AN INVESTIGATION OF REAL TIME ULTRASOUND DOPPLER TECHNIQUES FOR TISSUE MOTION AND DEFORMATION ANALYSIS

Aline Laure Criton

For the degree of Ph.D.

The University of Edinburgh

2005

ABSTRACT

Cardiovascular disease accounts for more than 50% of all deaths in the Western world. Atherosclerosis is responsible for the vast majority of these diseases. There are a range of risk factors for atherosclerosis that affect the endothelial lining vessel wall cells to cause endothelial dysfunction, which then predisposes to a localized build-up of 'plaque' tissue that narrows the lumen of the arteries. Plaque rupture promotes localized vasospasm, thrombosis and embolism causing downstream tissue death, resulting in severe disability or death from, for instance, heart attack (in the coronary circulation) or stroke (in the cerebral circulation). Narrowing of the lumen and plaque rupture are associated with high tissue stresses and tissue under perfusion, which will alter local arterial and myocardial wall dynamics and elastic properties. Hence visualization of tissue dynamic and deformation property changes is crucial to detect atherosclerosis in the earliest stages to prevent acute events.

The objective of this dissertation research is to develop new techniques based on Doppler ultrasound to investigate and visualize changes in tissue dynamic and deformation properties due to atherosclerosis in cardiac and vascular applications. A new technique, to correct for the Doppler angle dependence for tissue motion analysis has been developed. It is based on multiple ultrasound beams, and has been validated *in vitro* to study tissue dynamic properties. It can measure tissue velocity magnitude with low bias (5%) and standard deviation (10%), and tissue velocity orientation with a bias less than 5 degrees and a standard deviation below 5 degrees. A new Doppler based method, called strain rate, has also been developed and validated *in vitro* for the quantification of regional vessel or myocardial wall deformation. Strain rate is derived from the velocity information and can assess tissue deformation with an accuracy of 5% and a standard deviation less than 10%. Some examples of cardiac strain rate imaging have been gathered and are described in this thesis. Strain rate, as all Doppler based techniques, suffers from angle dependence limitation. A method to estimate one-component strain rate in any direction in the two-dimensional image not necessarily along the ultrasound beam has been developed. The method allows correcting for the strain rate bias along any user-defined direction. It is also shown that the full strain rate tensor can theoretically be extracted from the velocity vector field acquired by multiple beam tissue vector velocity technique. *In vitro* experiments have shown that qualitative two-component strain rate tensor can be derived. Two-component vector velocity from the moving tissue was acquired and two two-component strain rate images were derived. The images showed agreement with the expected deformation pattern.

Acknowledgements

This research was conducted in the Department of Medical Physics at the University of Edinburgh, in the Research and Development department of Philips Ultrasound in Bothell, WA (USA), and in Philips Research France in Paris (France).

I am grateful for the patient and knowledgeable supervision of Dr Jeff Powers, Dr Helen Routh, Professor Norman McDicken and Dr Pete Hoskins. Thanks also to my Philips colleagues, Thanasis Loupas, Cliff Cooley, Damien Dolimier, and Matthew Bruce for their incredible technical and moral support and for their useful (and occasionally, and more enjoyably, useless) discussions. My gratitude goes to other members of the Department of Medical Physics for providing enjoyable entertainments during my visits in Edinburgh.

My special thanks to Patrick Pesque for allowing me to undergo this PhD in Philips Ultrasound.

Finally I would like to express my deepest gratitude to my mother and father, and my husband Guy for without their continued encouragement, support and love this PhD and many other things in my life would not have been achieved.

To Sara, our daughter.

Table of Content

List of Abbreviations

WSS	Wall Shear Stress
MRI	Magnetic Resonance Imaging
B-mode	Intensity echo Imaging
RF	Radio Frequency
RGB	Red Green Blue
QBP	Quadrature Band Pass
QBF	Quadrature Band pass Filter
I	in phase
Q	in Quadrature
CW	Continuous Wave
PW	Pulsed Wave
2D	Two Dimensional
PRF	Pulse Repetition Frequency
LPF	Low Pass Filter
FFT	Fast Fourier Transform
CFI	Colour Flow Imaging
A-line	Amplitude echo line
PRI	Pulse Repetition Interval
CPA	Colour Power Angiography
TDI	Tissue Doppler Imaging
PET	Positron Emission Tomography
CT	Computed Tomography
SQ	Spatial Quadrature
1-C	one component
2-C	two component
3-C	three component
1-D	one dimension
2-D	Two Dimensional
3-D	Three Dimensional
AF	Atrial Filling
S	Systole
EF	Early Filling
BMF	Blood Mimicking Fluid
AWM	Arterial Wall Motion
QLab	Quantification Software Package
HDILab	Quantification Software Package
PSF	Point Spread Function
CCA	common carotid arteries
EPROM	non volatile memory
MO	Magneto Optical
CPU	Central Processing Unit
Mbytes	Mega Bytes
KHz	Kilo Hertz
WSS	Wall Shear Stress

MRI	Magnetic Resonance Imaging
B-mode	Intensity echo Imaging
RF	Radio Frequency
RGB	Red Green Blue
QBP	Quadrature Band Pass
QBF	Quadrature Band pass Filter
I	in phase
Q	in Quadrature
CW	Continuous Wave
PW	Pulsed Wave
2D	Two Dimensional
PRF	Pulse Repetition Frequency
LPF	Low Pass Filter
FFT	Fast Fourier Transform
AR	AutoRegressive
SCSI	Small Computer System Interface

List of Symbols

f_d	Doppler Frequency Shift in Hz
f_t	Transmit frequency in Hz
f_r	Receive Frequency in Hz
v	Velocity in m/s
θ	Angle in radian
c	Speed of sound in the tissue in m/s
t_{delay}	Time delay in seconds
d	Depth in m
$v_{\max}$	Maximum Velocity scale for a given PRF in m/s
$x(n,t)$	X position
$e(t)$	Echo intensity as a function of time
T	Period between pulse in seconds
$R(0,t)$	Lag zero autocorrelation function
$R(1,t)$	Lag one autocorrelation function
λ	Wavelength
B_d	Spectral Bandwidth
W	Aperture size
F	Aperture focal depth
$E(x)$	Effective aperture
$a_T(x)$	Transmit Aperture
$a_R(x)$	Receive Aperture
δ	Dirac function
$G_T(\mu)$	Transmit aperture signal frequency spectrum
$G_R(\mu)$	Receive aperture signal frequency spectrum
ω_d	Doppler frequency
v_x	Lateral Velocity component
v_z	Axial velocity component
σ^2	Variance
atan	Arc tangent function
rect	Rectangular function
cos	Cosine function
sin	Sine function
Sgn (x)	Function returning the sign of x
π	Pi number
exp(x)	Exponential function
tan(x)	Tangent function
$\overline{f_{Mean}}$	Mean Doppler Frequency Shift

$\vec{K}$	Unit vector in the direction of an ultrasound beam
$\vec{V}$	Vector velocity
SR	Strain rate and strain rate tensor
∂	Partial derivate
s_{xx}	Strain component along the x axis
S	Strain and strain tensor

1. Introduction and Thesis Aims

1.1. Introduction

The goal of this thesis is to develop new techniques, based on Doppler ultrasound, to detect, analyze, and visualize dynamic and elastic properties of tissues. Dynamic behavior of biological tissues relates to the motion of tissues in the body. Elastic properties define the relationship between the tissue deformation (dilation and compression) of biological tissues in relation to the force acting upon these tissues. Elastic and dynamic properties of moving tissues are changed during the process of certain diseases. One of the most common of these diseases is cardiovascular disease, which accounts for more than 50% of all deaths in the Western world. Some imaging techniques already exist to diagnose this disease but they have some limitations. Therefore development of new techniques to prevent, screen, and diagnose this disease is highly desirable. This chapter presents an overview of cardiovascular disease and the biomechanical basis of disease, a review of current ultrasound imaging techniques to assess this disease, and their limitations. This chapter also defines the aims of the thesis and gives an overview of its content.

1.2. Cardiovascular disease

In a healthy person, blood flows freely from the heart to all parts of the body through miles of arteries, but disease sometimes damages the arteries, slowing the flow of blood or even stopping it. The most common artery-damaging disease is atherosclerosis ('athero' means fatty; 'sclerosis' means scarring or hardening) and it is responsible for the vast majority of vascular and cardiac diseases. Atherosclerosis clogs the blood's pathways with an outgrowth called fibrous plaque (c.f. **figure 1-1**), which narrows the arteries, developing gradually over years and even decades.

Atherosclerotic plaque is responsible for clinical events, not only because it can narrow the arteries, but also because it can be a source of thrombosis (blood clots). Different types of plaque exist, stable plaque and vulnerable plaque. A small lipid pool and a large fibrous cap characterize stable plaque. Whereas vulnerable plaque is covered by a thin, fibrous cap and have a large lipid pool that upon rupture may lead to the formation of a blood clot and, ultimately, occlusion of the artery. Plaque rupture most often occurs in smaller arteries, such as the coronary arteries, which supply blood to the heart muscle. The occlusion of a coronary artery can lead to a heart attack. When a clot cuts off blood to the brain, the result is a stroke (Lakatta and Levy 2003).

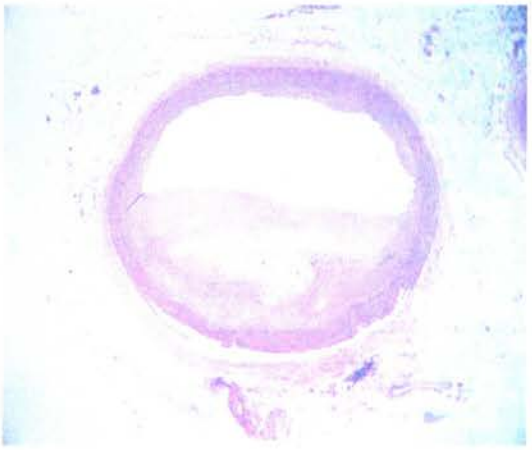

Figure 1-1: Microscopic image of an advanced lesion from a coronary artery. This image is reproduced from the Atherosclerosis Research web page of the School of Arts & Sciences, University of Pennsylvania (http://www.sas.upenn.edu/CGS/summer/highschool/pssa/pssa2004/atherosc.html)

Stroke and myocardial infarction risks are highly dependent on the plaque type. Until now no non-invasive technique can discriminate plaque types with sufficient reliability to enable identification and treatment of at-risk patients before rupture of

plaque occurs. Hence, a diagnostic tool with predictive capability would have a major impact on mortality and healthcare costs.

1.3. Cardiovascular Biomechanics

Biomechanics events are defined as internal and external forces exercised on and within the arterial wall. Blood vessels develop under the influence of mechanical stresses and strains and remodel in response to alterations of these factors. It has long been hypothesized that mechanical stresses and strains contribute to the development of vascular diseases such as atherosclerosis. Two main forces are responsible for atherosclerosis: wall shear stress and blood pressure.

1.3.1. Wall Shear Stress

Wall shear stress (WSS) is the viscous drag of the blood on the artery wall. Normal arterial flow is laminar, with secondary flows generated at curves and branches. A large number of studies have demonstrated that oscillatory low fluid shear stress and/or altered shear gradients (Kohler and Jawien 1992; Glagov 1994), due to eddy blood flow (turbulent flow) promote intimal hyperplasia (Liu 1999) (hyperplasia is defined as an enlargement of tissue due to increased number of cells). According to Glagov (Glagov 1994), intimal hyperplasia is not a pathologic process but an adaptive response of the arterial wall, which remodels itself to maintain optimal wall shear stress levels. Velocity profile skewing can create pockets in which the WSS is low (0.2 N.m-2). Atherosclerosis tends to localize to these sites (Caro, Fitz-Gerald et al. 1971; Ku, Giddens et al. 1985). High WSS is capable of damaging endothelial cells. Though high WSS is not present in healthy arteries or those with mild disease,

high WSS promotes thrombosis, and has been recorded in severely narrowed arteries (Strony, Beaudoin et al. 1993; Richardson 2002).

1.3.2. Blood Pressure

Blood pressure produces large forces, which are contained in normal arteries, but in diseased arteries the high internal stresses within the wall lead to plaque rupture (Loree 1992, Cheng 1993). This suggests that early disease is mediated by low WSS, whereas the latest and most dangerous phase of the disease, the rupture, is caused by blood pressure, the cyclic forces in the lumen of the artery giving rise to high tissue stresses. Plaque rupture is therefore associated with high tissue stresses, for which it is likely to have abnormal local arterial wall dynamics, and will generate abnormal myocardial wall dynamics.

1.3.3. Discussion

The material presented in this section reveals that cardiovascular disease is associated with alterations in the dynamic and biomechanical properties of tissues. Hence new diagnostic techniques should be based on assessing the dynamics (motion) and biomechanics (force) generated in the arterial and myocardial walls

1.4. Existing Ultrasound Investigative Methods

In vivo imaging techniques are used to measure quantities that can assess the degree of atherosclerotic disease. Depending on the location of the atherosclerotic vessel different imaging techniques and different criteria are used. Several imaging modalities, like MRI, angiography, nuclear medicine, and ultrasound, are used to diagnose atherosclerosis. However in this chapter only ultrasound techniques will be described, since the work of this thesis is based on developing novel ultrasound

Doppler technologies to assess the dynamics and biomechanics of the arterial walls and the myocardium.

In the first part of this section the Doppler Effect, basic principles of ultrasound and Doppler ultrasound imaging will be covered. Then more specific measurements and imaging assessment used to characterize atherosclerotic disease will be described. These are separated in the two most common clinical applications, carotid stenosis and cardiac infarction.

1.4.1. Basic Principles of Ultrasound and Doppler Ultrasound Imaging

In this section the basics of the Doppler Effect and ultrasound physics are briefly reviewed. An overview of conventional ultrasound B-mode, Spectral Doppler, Colour Flow Imaging and Tissue Doppler Imaging techniques is given to provide a foundation for the discussion of multi-component velocity and deformation estimations for tissue dynamic and biomechanics analysis in the following chapters. In this thesis 'dimension' refers to space (spatial dimension) and 'component' refers to components of the velocity vector.

1.4.1.1. The Doppler Effect

Whenever relative motion exists between a source of sound and a listener, the frequency of the sound as heard by the listener is different compared to the frequency when there is no relative motion. If the source and the listener are moving towards each other, the observed frequency is higher than the emitted frequency; if they are moving apart the heard frequency is lower. This phenomenon is known as Doppler Effect and was discovered by the Austrian physicist Christian Doppler (1803-1853). The Doppler Effect is used in many domains including in medicine and more

particularly in diagnostic ultrasound to detect motion within the body (this will be developed in sections 1.4.1.4 and 1.4.1.5). The use of the Doppler principle in medical ultrasound varies slightly from the classical Doppler method in that the moving targets (within the body) do not spontaneously emit a radiation, and it is therefore necessary to transmit a signal into the body to observe the changes in frequency, which occurs when it is reflected or scattered from the target.

It can be shown that under these conditions there is a shift in the ultrasound frequency given by (Evans and McDicken 2000):

$$f_d = f_t - f_r = 2 f_t v \cos\theta / c \qquad (1\text{-}1)$$

where f_t and f_r are the transmitted and received ultrasound frequencies respectively, v is the velocity of sound in the medium, θ is the angle between the ultrasound beam and the direction of motion of the target. If the angle between the direction of the moving targets and the ultrasound beam is not known the velocity estimation $v = v\cos(\theta)$ is biased by a $\cos(\theta)$ factor. This bias is also called angle dependence. Commercialized Doppler ultrasound systems measure only one-component of the three-component velocity vector of moving targets. As described later this lack of knowledge of target direction can lead to errors in velocity estimation (section 1.4.1.4).

1.4.1.2. Basic Principles of Ultrasonic Imaging

Ultrasonic imaging utilizes the same principles of pulse/echo ranging as radar and sonar. It transmits a beam of ultrasound radiation (which ranges between 1MHz and 20 MHz) into the body, collects and analyzes the returning echoes. Imaging devices are able to calculate the coordinates from which echoes originated, and these together

with knowledge of echo amplitudes allow cross-sectional images of the body to be acquired.

The imaging process begins with the application of a voltage pulse to a transducer array. The actual timing of the application of the pulse on different transducer array elements can be varied to steer and focus the transmit beam as illustrated in **figure 1-2a**. The transducer converts these electrical pulses into high frequency acoustic pulses, which propagate into tissue. The transmitted pulse is composed of high frequency sinusoids in the bandwidth of the transducer modulated by a slower varying envelope (called window). Whenever the outgoing pulse encounters an interface between tissues with different acoustic impedance, a fraction of the sound energy is scattered back towards the transducer (**figure 1-2b**), where it is reconverted back into an electrical signal, called Radio-Frequency (RF) data (**figure 1-2c**). The scattered envelope will differ from the transmitted pulse due to attenuation, scattering, and diffraction. The echoes returning will arrive back at the transducer following a round trip time, t_{delay}, of

$$t_{delay} = \frac{2 \cdot d}{c} \qquad (1\text{-}2)$$

where c is the speed of sound in the tissue and d the depth (Angelsen 2000). The envelope of the received signal is then calculated and mapped to a brightness value (**figure 1-2d**). This pulse/echo process is then repeated for an entire sector to make an image as in **figure 1-2a**.

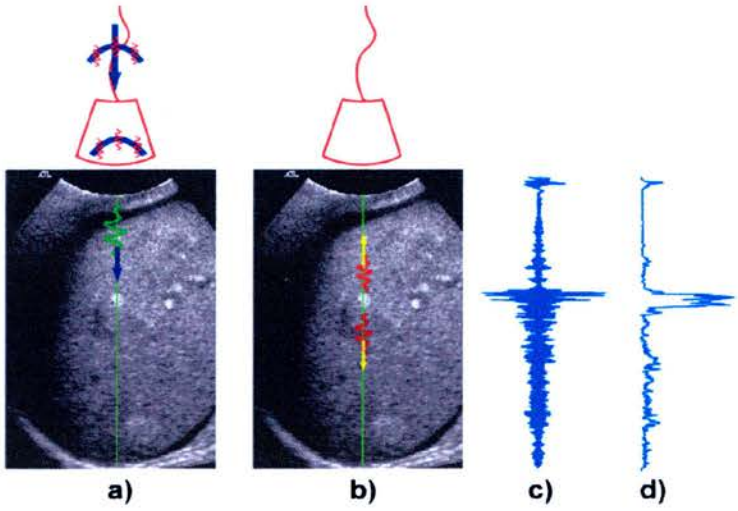

Figure 1-2: Pulse Echo illustration. a) Focused transmitted pulse. b) Sound energy reflected from the transmitted pulse by acoustic interfaces. c) RF data received from the transmitted pulse as a function of depth or time. d) Envelope of the received RF data.

1.4.1.3. Conventional B-Mode Ultrasound Imaging

A conventional B-mode image is formed by transmitting a pulse from a transducer array down a particular direction. Following transmit, the transducer array turns into a receiving array listening for backscattered echoes from tissue. **Figure 1-3** illustrates the path a signal follows once echo returns are received from the transducer array for a B-Mode image. A signal from each element of the scanhead array feeds into a beamformer, which spatially filters across the array such that scattering from a particular depth coherently adds. The resulting RF signal then enters a bandpass filter producing quadrature components.

These quadrature components enable the calculation of the instantaneous amplitude of the filtered-RF signal in the detection block. This signal is then log-compressed to fit within the dynamic range of the eye when displayed on a monitor. The low level signals are brought up closer to brighter signals in the compressed signal, enabling

the simultaneous visualization of weak and strong signals. Echo returns from each transmit line covering an image sector are then stored in a buffer, before scan conversion interpolates the data in a grid of square pixels. Then the scanconverted data is displayed on the monitor using RGB grey map.

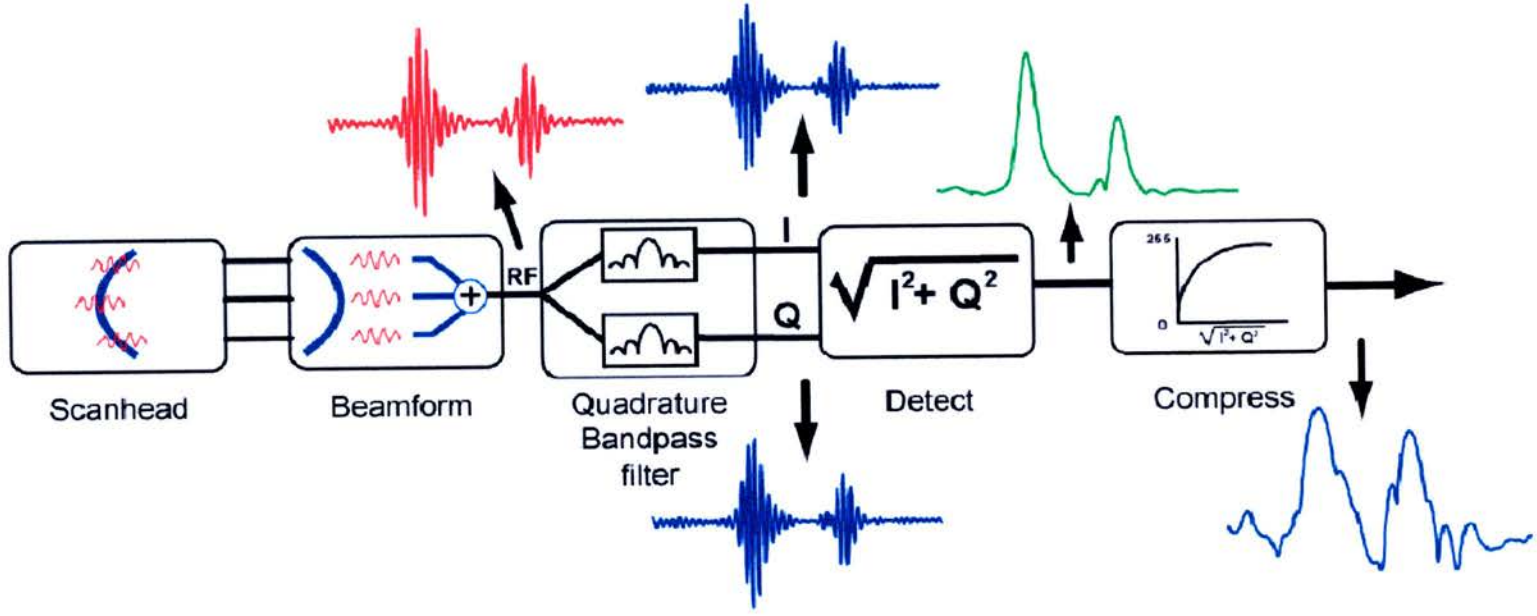

Figure 1-3: B-mode receive signal processing

1.4.1.4. Spectral Doppler

Doppler systems may be classified according to their transmit regime. Continuous wave (CW) devices transmit and receive ultrasound continuously whereas pulsed wave (PW) devices transmit and receive pulses. Most modern Doppler systems use PW techniques as this allows depth discrimination. Pulsed wave Doppler systems can be used to produce time-velocity waveforms in the form of a spectral Doppler trace (**figure 1-4**), considered in this section, or a 2D image of blood flow in the form of colour flow imaging, and considered in the next section.

Modern commercial spectral Doppler systems display a one-component velocity of the targets in a single sample volume as a function of time. Spectral Doppler combines the use of the Doppler Effect and ultrasonic imaging to detect the velocities of the moving targets. A conventional pulsed wave spectrum is formed by transmitting a pulse from a transducer array down one particular direction at a certain Pulse Repetition Frequency (PRF). The transmission and reception of the pulses follow the same principles as for conventional B-mode, except that the aperture used (delays of each element in transmit and in receive) and the pulse definition (frequency, length, and windowing) have different characteristics. **Figure 1-5** illustrates the path a signal follows once returned echo are received from the transducer array to form a spectrum.

Multiple acquisitions down the Doppler scanline at a constant PRF are used to detect the velocity projection of moving blood along the acoustic beam. Echoes from scatterers moving towards or away from the transducer will arrive at the transducer with frequencies slightly shifted from the transmit frequency f_t (c.f. equation 1-1).

The frequency shift, called Doppler shift f_d, is proportional to the projection of the moving target velocity along the ultrasound beam (c.f. equation 1-1).

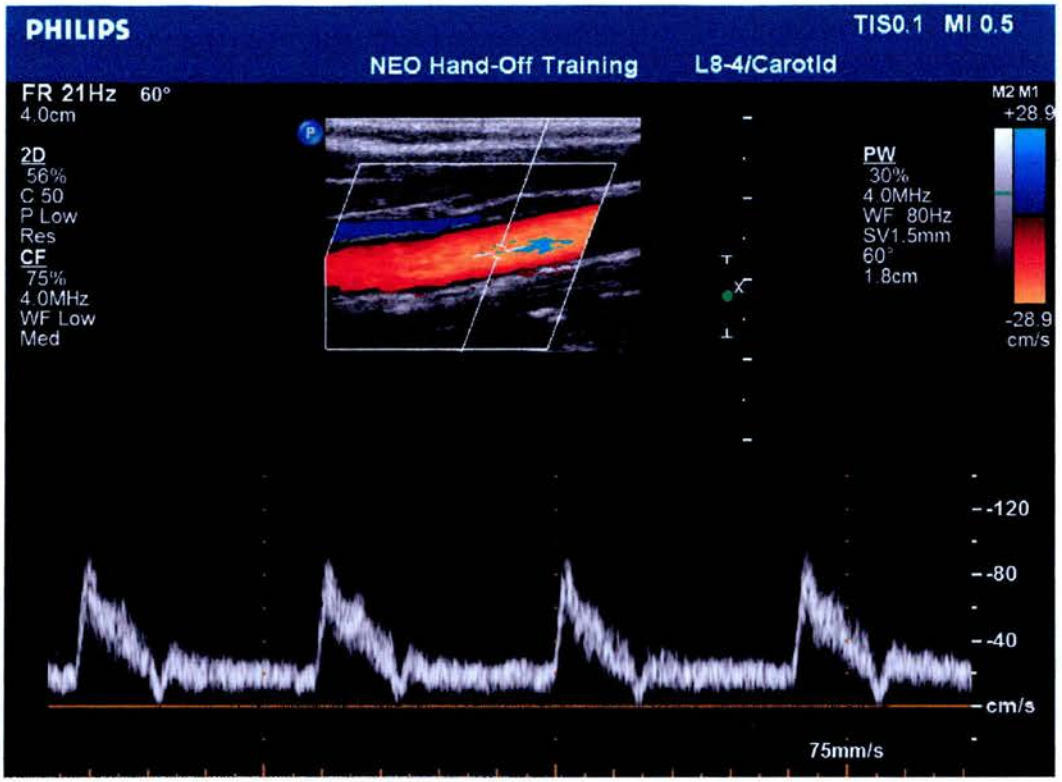

Figure 1-4: Spectral Doppler from a sample volume located in the carotid vessel.

After reception of each pulse, pulse 1 to pulse N, enters the processing chain illustrated in **figure 1-5.** The first step in the processing chain is quadrature bandpass filtering (QBF) to remove out of band noise. The In-phase and Quadrature signals (IQ) are created by multiplying by $\cos(2\pi f_t t)$ and $\sin(2\pi f_t t)$ and then low pass filtering (quadrature generation and Low Pass Filtering (LPF) is equivalent to bandpass filtering) resulting in the instantaneous phase in both depth and Doppler dimensions. All IQ pairs for one particular depth (sample volume or gate depth) for each pulse are stored in a buffer. The IQ pairs are high pass filtered, to remove high amplitude low velocity tissue motion (clutter), leaving higher velocity lower

amplitude blood flow signals. This step is also called high pass filter. Then the resulting IQ pairs are converted to a spectrum by processing them through a fast Fourier transform (FFT). This spectrum displays the Doppler frequency shift generated by the moving target within the sample volume as a function of time.

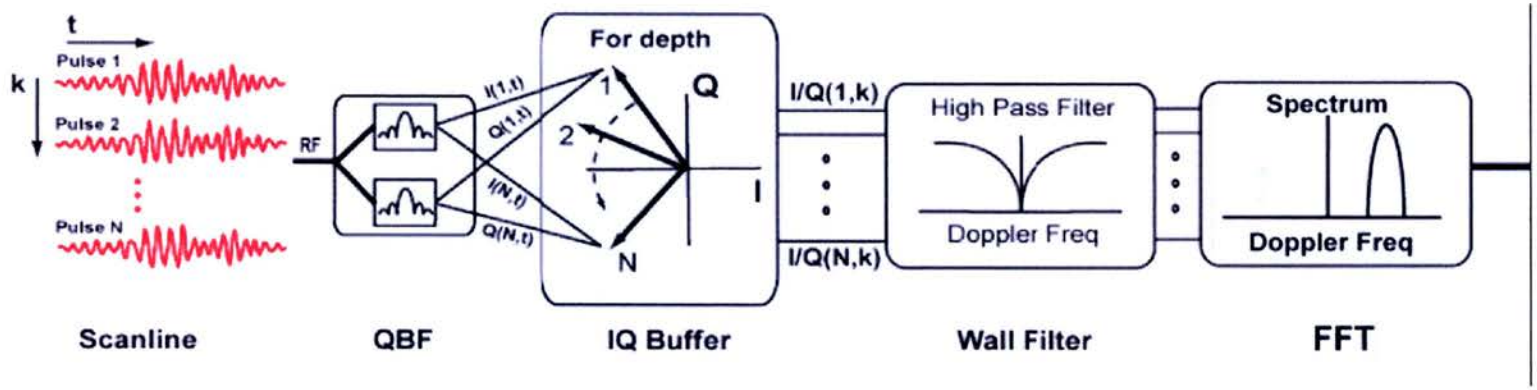

Figure 1-5: Spectral Doppler receive signal path

There are two main limitations to the single beam PW Doppler approach. First the maximum detectable velocity v_{max} is related to the PRF by the following equation(Evans and McDicken 2000):

$$v_{max} = \frac{c \times PRF}{4 f_t \cos(\theta)} \tag{1-3}$$

Aliasing artifacts can be produced if a target moving above the v_{max} velocity is present within the sample volume. The velocity of the fast moving target is then underestimated. This is also called "Nyquist" limit and equivalent to saying that the maximum Doppler frequency shift that can be detected is half of the PRF. Secondly the velocity measured is limited to the projection of the three-component velocity vector along the ultrasound beam axis. Hoskins et al. (Hoskins 1996) used moving string phantoms to investigate the dependence on the Doppler angle. In **figure 1-6** extremely large errors in velocity for beam-string angle above 70 degrees can be observed for conventional Doppler ultrasound.

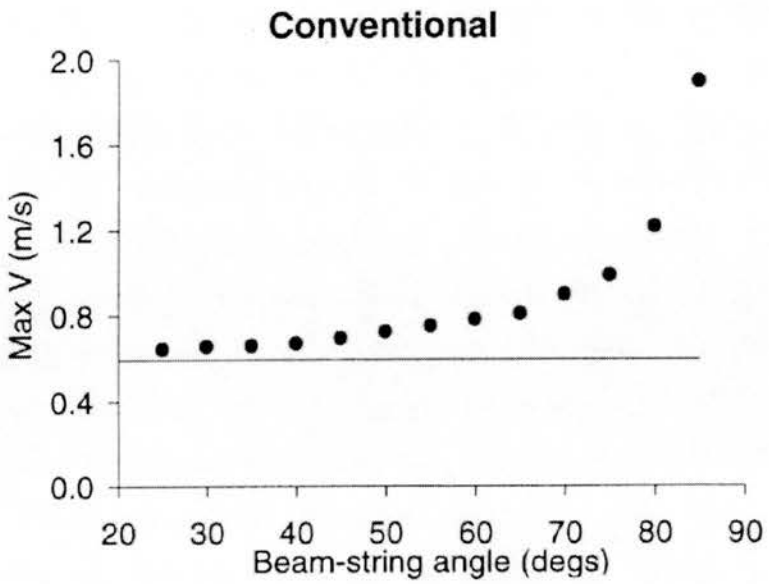

Figure 1-6: Measured maximum velocity in the string phantom as a function of ultrasound beam string angle (from Hoskins 1996, with permission).

1.4.1.5. Conventional Colour Flow Imaging

In this section the two-dimensional detection and visualization of one-component flow velocity measurements called Colour Flow Imaging (CFI) is described. Colour Flow Imaging uses multiple samples gates to map in two dimensions, one component velocity of moving blood cells (c.f. **figure 1-7**). CFI combines conventional real time pulse echo B-mode with real time two-dimensional pulsed Doppler imaging.

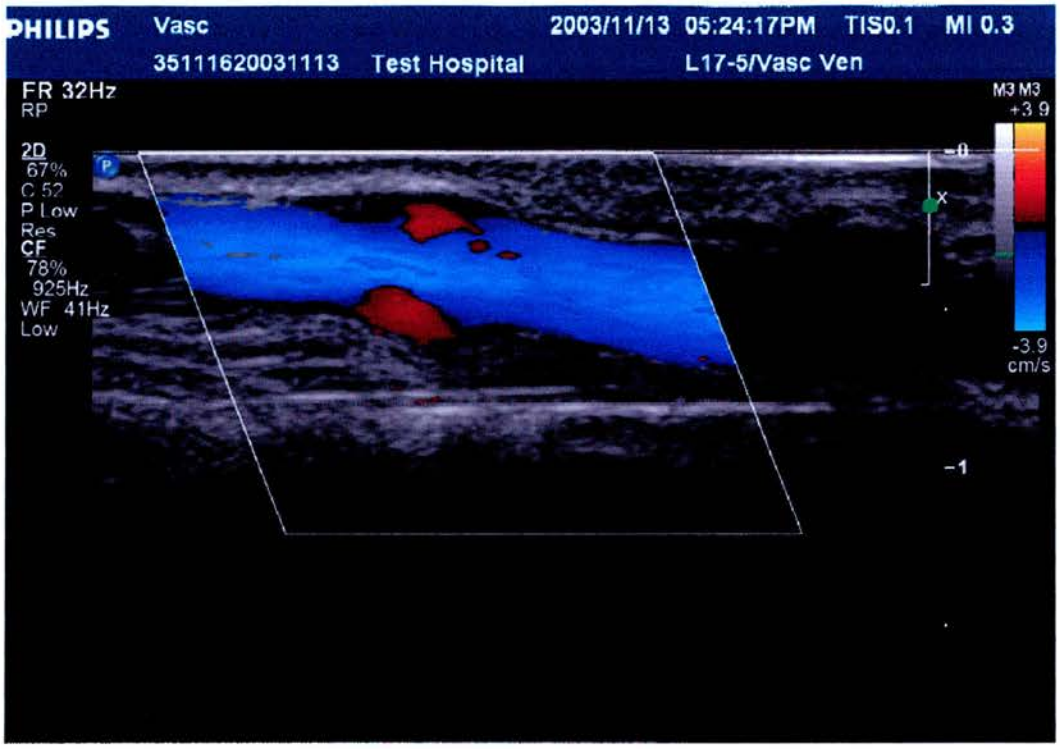

Figure 1-7: Colour Flow Imaging of blood flowing through a superficial vein.

Two different techniques can be used to derive the two-dimensional mapping of one-component velocity information from the pulsed Doppler signals. The first one uses the time domain approach and was developed by Bonnefous et al. (Bonnefous and Pesque 1986). The other one uses a phase domain approach and was developed by Kasai et al (Kasai, Namekawa et al. 1985). The latter is used in most of the commercially available ultrasound systems. The following describes the phase domain approach to estimate the one-component blood flow velocities based on the temporal samples of the complex demodulated signal from fixed positions in space. The transmit sequence for a colour Doppler image entails two different acquisitions **(Figure 1-8)**, a broadband pulse for B-mode and a narrower band pulse for colour flow. **Figure 1-8b** shows A-lines acquired for both the echo and colour pulses in the sector of **figure 1-8a**. The A-lines are displayed sequentially in time as fired across

the sector. B-mode pulses are fired across the sector within the region defined by the edges of the colour box, where upon the colour pulses begin to be acquired. **Figure 1-8b** illustrates an ensemble of 8 pulses, used for flow estimation, being sent down each colour scanline with a Pulse Repetition Interval (PRI) equal to 1/PRF (Pulse Repetition Frequency). The number of pulses used to collect a single colour flow line is called the ensemble length.

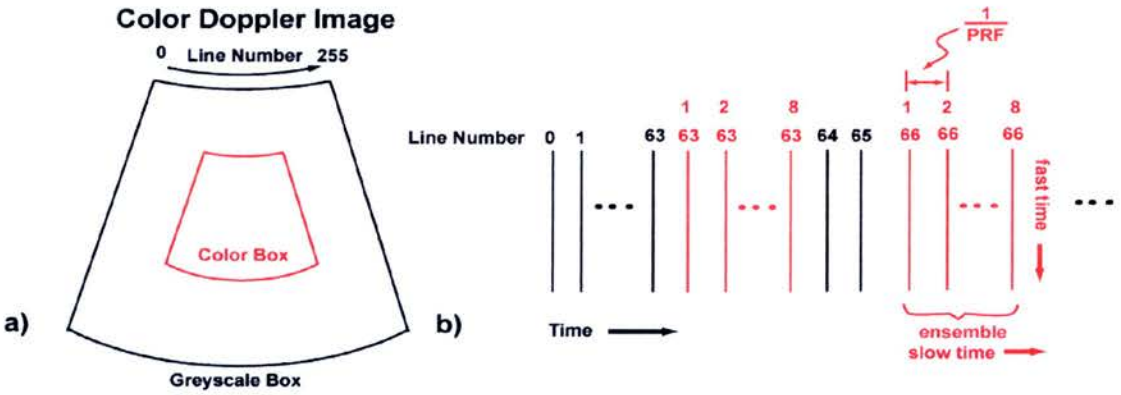

Figure 1-8: Colour Flow Imaging. a) B-mode and CFI 2D sectors. b) B-mode and CFI pulse sequencing.

The multiple acquisitions down the colour scanlines are used to detect the presence of the projection of moving blood along the acoustic beam. Echoes from scatterers moving towards or away from the transducer will arrive at the transducer with delays that change from echo to echo. These delays are proportional to the projection of the moving target velocity along the ultrasound beam. For a scatterer moving towards the transducer with a velocity, v, the received signal, $x(n,t)$, due to the n^{th} transmitted pulse in the ensemble will be

$$x(n,t) = e\left(t - t_{delay} - \frac{2nvT}{c}\right)\cos\left(2\pi f_t\left(t - t_{delay} - \frac{2nvT}{c}\right)\right) \qquad (1\text{-}4)$$

where t_{delay} refers to the pulse echo delay, T is the pulse repetition interval, n is the pulse number, v is the velocity, f_t is the transmit frequency, c is the speed of sound in the tissue, and e is the amplitude of the returned echo signal (Angelsen 2000). A slight frequency shift due to the Doppler Effect is neglected here under the assumption that $c>>v$.

After reception of each pulse, pulse 1 to pulse N, enters the processing chain illustrated in **figure 1-9.** The first step in the processing chain is quadrature bandpass filtering (QBF) to remove out of band noise. The IQ signals are generated by multiplying in (1-5) by $\cos(2\pi f_t t)$ and $\sin(2\pi f_t t)$ and then low pass filtered resulting in

$$
\begin{aligned}
I(n,t) &= e_{filtered}\left(t - t_{delay} - \frac{2nvT}{c}\right)\cos\left(\phi(n)\right) \\
Q(n,t) &= e_{filtered}\left(t - t_{delay} - \frac{2nvT}{c}\right)\sin\left(\phi(n)\right) \\
\phi(n) &= 2\pi f_t t_{delay} - 2\pi n f_d T
\end{aligned}
\tag{1-5}
$$

the instantaneous phase in both the depth and Doppler dimensions, where f_d (c.f. equation 1-1) is the Doppler frequency, t_{delay} refers to the pulse echo delay, T is the pulse repetition interval, n is the pulse number, v is the velocity, f_t is the transmit frequency, c is the speed of sound in the tissue, and $e_{filtered}$ is the filtered amplitude of the returned echo signal. Equations (1-5) are illustrated in the IQ buffer block of **figure 1-9** in complex form, $I(n,t)+jQ(n,t)$, at a particular depth t_{delay}. All the IQ pairs in depth for each pulse in the ensemble of a particular scanline J are stored in a buffer.

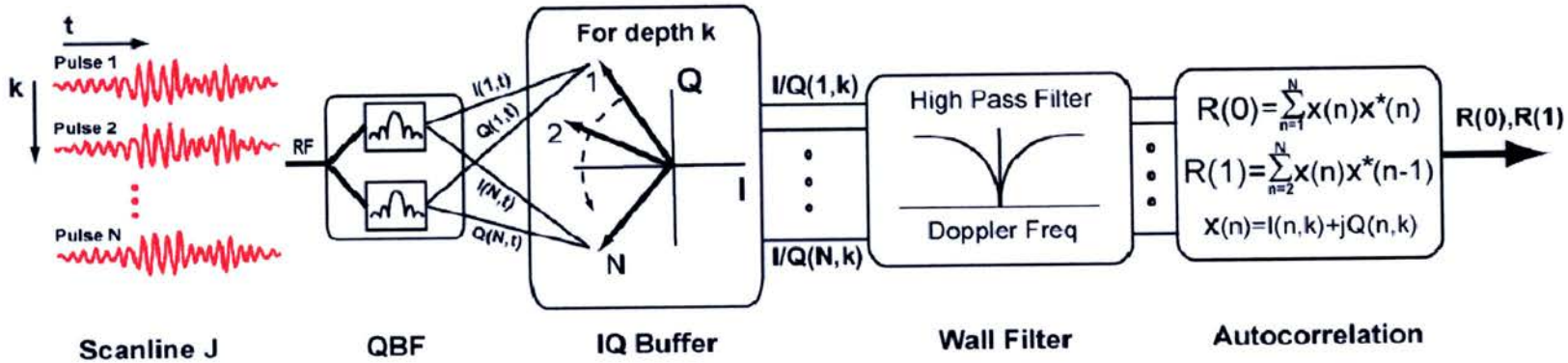

Figure 1-9: Colour Flow Imaging receive signal path

This IQ signal pair is then high pass filtered, to remove low velocity tissue motion, leaving higher velocity lower amplitude blood flow signals. The first two lags of the autocorrelation, $R(t,0)$ and $R(t,1)$, are then estimated using the following equations:

$$R(0,t)=\sum_{n=1}^{N} x(n,t)x^{*}(n,t)$$
$$R(1,t)=\sum_{n=1}^{N-1} x(n,t)x^{*}(n-1,t) \qquad (1\text{-}6)$$

where $x(n)=I(n,t)+jQ(n,t)$ and * represents the complex conjugate.

At this point the processing chain splits depending upon which colour flow mode is active. For clinical applications where the presence or absence of low velocity flow is important, the directionality of the flow is sacrificed and simply the power of the Doppler signal is displayed the lag zero of the autocorrelation (*R(0,t)*), **figure 1-10**. This display is illustrated on **figure 1-11**. This mode allows extremely low PRFs because aliasing of the Doppler signal from higher velocity flow is not a problem for visualization.

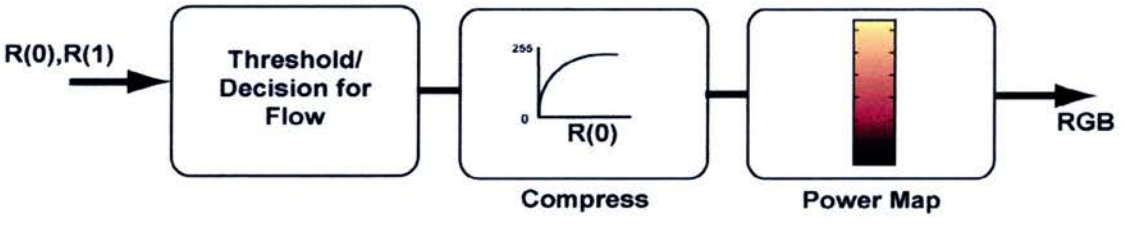

Figure 1-10: Colour Power display processing

R(0,t) is thresholded to remove noise and remaining tissue signal, compressed and mapped to an RGB value ready for display.

Figure 1-11: Display of lag zero of the autocorrelation estimator (carotid bifurcation flow).

In most clinical applications, the direction of the blood flow is important such as in the identification of vascular anatomy or flow dynamics in a vessel. In this mode *R(0,t)* is still used for thresholding noise and tissue clutter, but now the phase of the first lag of the autocorrelation, *R(1,t)*, is used for velocity estimation (c.f. **figure 1-12**).

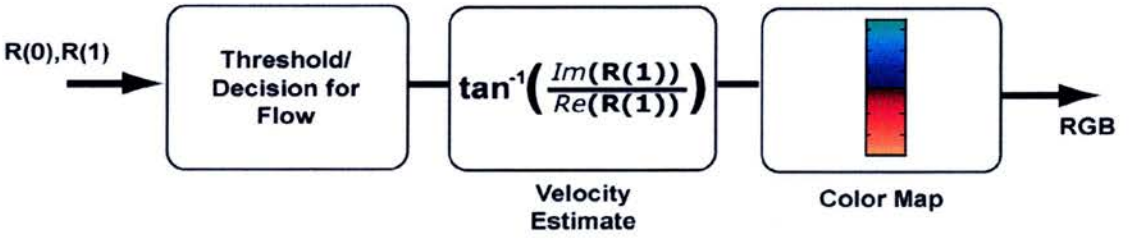

Figure 1-12: Colour Flow display processing

Figure 1-13 shows that the phase of *R(1,t)* boils down to a weighted average of phase differences between adjacent PRIs. If the magnitude of a PRI is small, then it contributes little to the overall magnitude and direction of *R(1,t)*. This phase difference is proportional to the Doppler shift experienced between PRIs.

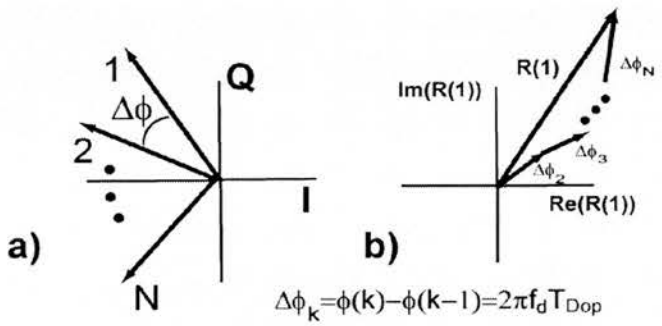

$$\Delta\phi_k=\phi(k)-\phi(k-1)=2\pi f_d T_{Dop}$$

$$R(1)=\frac{(|x(2)||x(1)|e^{j(\Delta\phi 2)}+|x(3)||x(2)|e^{j(\Delta\phi 3)}+\ldots+|x(N)||x(N-1)|e^{j(\Delta\phi N)})}{N}$$

Figure 1-13: a) IQ with Doppler shift b) Graphical representation of R(1)

The phase of R(1,t) is proportional to the mean Doppler frequency. This phase is then mapped to a colour scale, usually red for motion towards the transducer and blue for motion away from the transducer.

1.4.1.6. Conventional Tissue Doppler Imaging

Tissue Doppler Imaging is also a Doppler technique derived from the CFI technology to display tissue motion. It estimates the component of the tissue velocity vector projected on the acoustic beam. The concept of tissue Doppler imaging was introduced by McDicken et al. (McDicken, Sutherland et al. 1992) and was further developed by Sutherland et al. (Sutherland, Stewart et al. 1994). TDI is essentially used to assess cardiac muscle function and arterial wall motion. The velocities in the cardiac tissue are much lower than blood flow velocities (0-15 cm/s) and in the

arterial wall motion they are even lower (<1 cm/s). The signal processing performed in TDI is similar to that used by CFI systems to image blood flow. Modifications of the ultrasound system acquisition and signal processing parameters are required. These modifications are illustrated in **figure 1-14**. The high pass filter for the TDI signal path is bypassed or greatly weakened and the IQ pairs flow directly from the IQ buffer to the autocorrelation processing. The rest of the signal processing remains the same (c.f. **figure 1-14**). The velocity map is usually not thresholded, but just superimposed on the grayscale with a blending function so the grayscale structures can still be seen behind the colour velocities (c.f. **figure 1-15)**. The velocity of tissue motion is low compared to the blood velocity and the tissue signal amplitude is high compared to the blood signal amplitude. The acquisition sequence is therefore modified by having shorter ensemble length and lower Pulse Repetition Frequencies (PRFs).

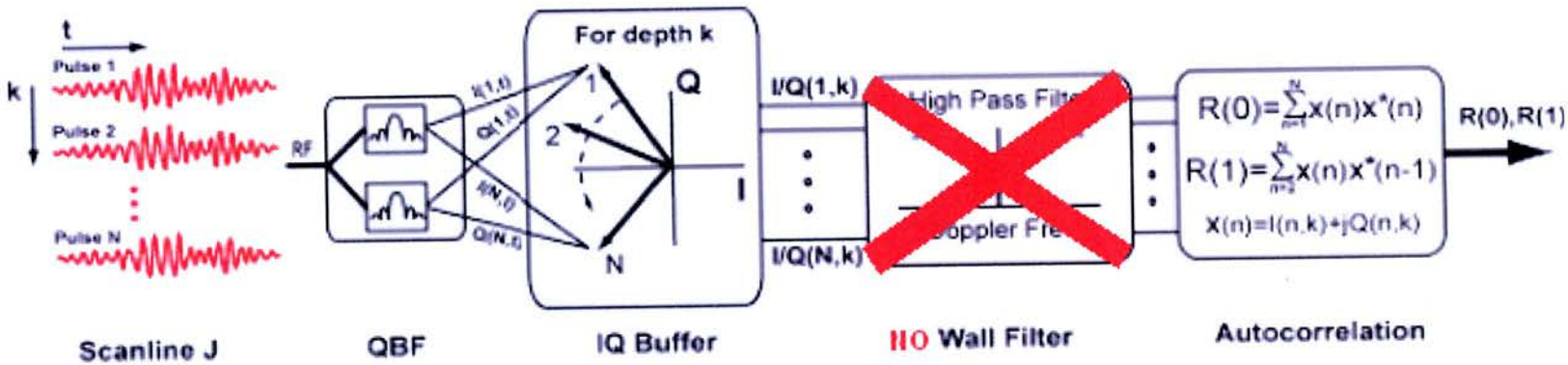

Figure 1-14: Colour Doppler receive signal path modified for Tissue Doppler Imaging

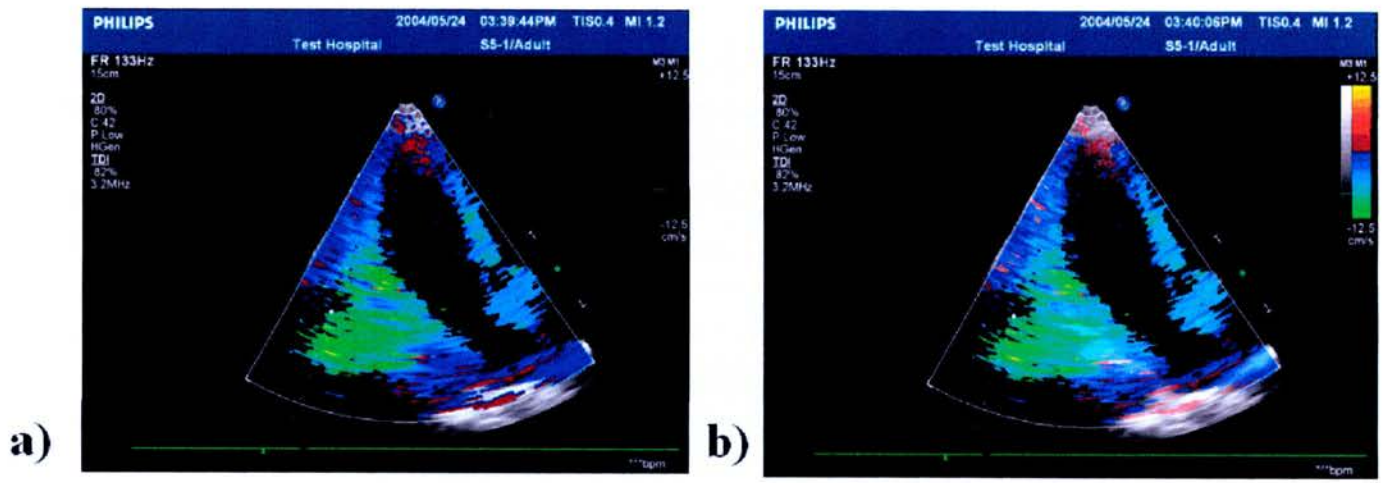

Figure 1-15: Tissue Doppler Imaging of the left ventricle. a) TDI without blend. b) TDI with blending.

1.4.2. Clinical Assessment of Atherosclerosis

1.4.2.1. Carotid Stenosis

In the case of carotid stenosis, the traditional approach of assessing the severity of a lesion and the resultant risk of stroke is based on its dimensions (e.g., percent of area stenosis) and the lesion composition (visual assessment of plaque morphology). The selection criteria are based on the estimation of the arterial lumen reduction, using anatomical visualization (Jmor, El-Atrozy et al. 1999) and blood velocity measurements (Chen, Salvian et al. 1998; Jogestrand, Lindqvist et al. 2002). Spectral Doppler can display the flow pattern within the stenosis. The estimation of the peak velocity within the jet is used to evaluate the degree of stenosis in diseased arteries by using standard tables (Bluth, Stavros et al. 1988; Robinson, Sacks et al. 1988). This measurement is often inaccurate. Random errors (±3 degrees of angle correction) lead to a variation of the degree of stenosis of ±12% (Kalman, Johnston et al. 1985). More important are the systematic errors resulting from a lack of knowledge of the true flow direction. This is often assumed to be parallel to the vessel wall. It has been shown that the angle error may be as high as 25° (Hoskins 1996). It is accepted that maximum velocities above 1.2 and 2.4 m/s correspond to stenoses with lumen restriction over 75% and 90%, respectively. However Arbeille et al. (Arbeille, Bouin-Pineau et al. 1999) showed that 41% of stenoses presenting a restriction ranging from 70% to 80 % have a maximum velocity lower than 1.2 m/s and that for higher degree of stenosis, the dispersion of the maximum velocity is high. Therefore an under- or overestimation of the Doppler angle of ±10 degrees could bias the degree of stenosis of more than 30 % and mislead the final diagnostic result.

Another measurement used to quantify arterial occlusive disease is the spectral broadening index (Kassam, Cobbold et al. 1982; Morin, Johnston et al. 1988). Spectral broadening is not only linked to the geometry of the transducer but also to the flow turbulence degree (and also the acceleration and velocity gradient within the sample volume). This index is obtained by measuring the maximum velocity spectrum at peak systole. The nonstationarity of the Doppler signal during the acquisition period is a problem for this measurement as Cloutier et al. raised (Cloutier, Shung et al. 1993). Using a pulsatile laminar flow model (phantom) they showed that the relative Doppler bandwidth invariance did not hold during acceleration and deceleration of blood flow. They concluded that even when using a small window (2.5 ms) to minimize nonstationarity effects, broadening due to spectral leakage dominated over geometric broadening. Therefore spectral broadening cannot be used in the clinical context without a new estimator other than the Fast Fourier Transform.

None of the previous techniques can provide information related to the dynamic behavior or the deformation of diseased arterial wall tissue, and hence are unable to distinguish between stable and unstable plaque.

Techniques for investigation of arterial wall motion have been described in the literature. Most of these measure motion of a single diameter, providing time-displacement waveforms, from which can be derived measures of elastic modulus (Wilson, Whyman et al. 1999; Wilson, Hoskins et al. 2000). A technique, which was developed by Bonnefous (Bonnefous, Montaudon et al. 1996), extends this approach, providing information on the relative movement in the longitudinal direction, and hence allowing relative strains to be investigated. This information is currently

unavailable using any other imaging modality, and does seem to offer great potential in assessment of the dynamic behavior of arterial plaque. By examination of such features as local motion along an arterial segment it is possible to both quantify and image the dynamic function of the arterial walls. This approach provides fundamental new knowledge of the physical mechanisms for rupture of carotid plaque. However this technique is derived from Tissue Doppler Imaging and therefore is angle dependent. The observed vessel wall motion is very complex even in normal subjects, due to bends and bifurcations in arteries, the non-regular layering and in homogeneities in the arterial walls (Liu, Lai et al. 2001; Weydahl and Moore 2001). Therefore a one-component velocity technique cannot fully assess these complex motions (Hoskins 2002). This technique is also only related to global motion of arterial walls and does not assess deformation, stress and strain within the arterial walls, which are modified during the disease process (Perktold and Rappitsch 1995; Hofer, Rappitsch et al. 1996).

1.4.2.2. Cardiac Infarction

In cardiology, the prevention, causes, and progression of myocardial ischemia continues to be a research priority. In clinical medicine, much research has focused on the early diagnosis and treatment of acute cardiac ischemia.

In echocardiography the study of the heart motion, especially the left ventricle, is of central interest. Indeed several investigations (Buda, Delp et al. 1983; O'Boyle, Parisi et al. 1983), have indicated that the analysis of endocardial motion provide a valid means of identifying some degree of ischemia. Tissue Doppler Imaging (TDI) acquires at very high frame rate one-component velocity fields (projection of the velocities along the ultrasound beams). Some studies have shown the potential

diagnostic role of this technique in determining regional myocardial function from velocity data sets for a number of heart diseases (Garcia, Rodriguez et al. 1996; Katz, Gulati et al. 1997; Severino, Caso et al. 1998; Derumeaux, Douillet et al. 1999; Galderisi, Caso et al. 1999; Mankad, Murali et al. 1999; Pasquet, Armstrong et al. 2000; Severino, Caso et al. 2000). Although encouraging data were obtained, it was clear that the interrogation of one-component velocity is not sufficient to fully assess regional myocardial function because of two major limitations. Like other Doppler modalities, Tissue Doppler measurements are dependent on the angle between the ultrasound beam direction and the motion direction of myocardium. The second problem of the technique is due to overall heart motion, rotation and deformation, which influence regional wall velocities (Hosono, Nakano et al. 1995; Taratorin and Sideman 1995; O'Dell and McCulloch 2000; O'Dell, McCulloch et al. 2000). Velocity information allows only a description of dynamic events and does not assess biomechanics of the myocardium, such as contraction and relaxation (Young, Kramer et al. 1994; Papademetris, Sinusas et al. 2001; Kuijer, Marcus et al. 2002; Hu, Metaxas et al. 2003).

1.4.3. Conclusion

Today, techniques exist to measure one-component velocity of moving blood and tissue with ultrasound Doppler imaging technology. However, a major drawback of these measurements is that the motion estimation is limited to the velocity component along the ultrasound beam axis. Cardiac and vessel wall motion studies have shown that complex three-component motions can be observed (Hosono, Nakano et al. 1995; Perktold and Rappitsch 1995; Taratorin and Sideman 1995; O'Dell and McCulloch 2000; O'Dell, McCulloch et al. 2000; Ding, Zhu et al. 2002;

Zhu and Friedman 2003). Hence there is a clinical need to fully assess the three components of the vector motion. The Doppler techniques, described in this chapter (spectral Doppler, Colour Flow and TDI), enable the assessment of the dynamic properties of flow and tissue. However they do not allow the assessment of the tissue deformation, which is of central interest in cardiovascular disease. Therefore a new technique to detect the tissue deformation tensor is needed to assess tissue biomechanics.

1.5. Thesis Aims

The aims of this thesis are to assess and visualize the tissue dynamic and deformation in the carotid arterial wall and in the myocardium in real time, using Doppler ultrasound based techniques. To achieve these goals two techniques have been developed:

1. A technique to correct for the angle dependence of the existing Tissue Doppler Imaging technique.
2. A new technique to assess deformation abilities of the tissue derived from one-component and multi-component tissue velocity estimation.

The thesis is organized in the following manner in order to address these aims:

- Chapter 1 gives an introduction to the clinical problem, "atherosclerosis", an overview of existing ultrasound imaging technologies and defines the aims of this thesis
- Chapter 2 will review the existing multi-component velocity estimation techniques for flow and tissue applications, and describe their performance and how they can be implemented in real time. From this review we will deduce the best methods to measure vector velocity in tissue motion.

- Chapter 3 will describe a real time, two-component velocity pulsed wave Doppler system developed to understand the basics of vector Doppler. An in vitro validation of this technique is also presented.
- The purpose of chapter 4 is to develop a technique to measure multi-component vector velocity for tissue motion imaging to overcome the angle dependence of the TDI technique. This technique is validated *in vitro* using motion phantom.
- Chapter 5 will investigate theoretically and experimentally a new technique to assess myocardial deformation, one-component strain rate imaging approach, derived from one-component tissue velocity estimation to overcome limitations of the Tissue Doppler Imaging which can measure only dynamic properties of tissue but cannot assess mechanical properties (stress, strain). This technique is validated *in vitro* using tissue mimicking phantom and *in vitro* in cardiac applications.
- Chapter 6 will describe theoretically a new technique, which allows the full measurement of the strain and strain rate tensors from multi-component vector velocity data.
- Finally in chapter 7 we will give a brief summary of the results and discuss how this work can be continued.

2. Review of Current Multi-Component Velocity Estimation Techniques

2.1. Introduction

As described in the previous chapter, one of the main limitations of Doppler ultrasound techniques is its angle dependence. The aim of this chapter is to review the current methods to estimate two and three vector velocity components, in order to choose the best technique for the estimation of the two and possible three components of tissue vector motion within the scan plane. Most of the existing multi-component velocity detection techniques have been developed to measure vector velocities of moving blood. Indeed Doppler ultrasound has long been used to quantify and image blood flow in the body compared to TDI, which is a relatively new technique. One of the goals of this thesis is to develop a multi component vector motion estimation technique for tissue application. This chapter describes existing multi component velocity vector estimators for flow in order to understand if these techniques can be applicable to tissue application and how they need to be modified for multi component velocity vector estimators for tissue.

The vector velocity techniques can be divided into 4 different domains, optical flow, edge detector, region matching, and Doppler-based techniques. This division has been made because these techniques are relying on different criteria to perform motion detection. The term "optical flow" refers to the temporal changes of brightness patterns in an image sequence, which can be used to infer the between-frames velocities of moving objects. Edge detection techniques can be used for cardiac wall motion assessment and consist of finding discontinuities in grayscale intensities and tracking these discontinuities throughout the cardiac cycle. Region matching (also called speckle tracking) techniques consist of measuring frame to

frame displacements by comparing the speckle pattern between successive images, the best match indicating the most likely distance that the speckle pattern has moved. Once the displacements have been accurately found the velocities can be calculated by integrating displacement with respect to time.

Edge tracking only allows tracking of the main edges in a grayscale image and does not give a complete mapping of the motion of every point in a two-dimensional image. This method will not be pursued because of this limitation. Other grayscale based methods (speckle tracking and optical flow) are highly dependent on frame rate, image quality and require retrospective analysis and a lot of computation power which makes these techniques non real time (Lubinski, Emelianov et al. 1999; Lubinski, Emelianov et al. 1999). For these techniques, low frame rate will result into great changes from frame to frame, resulting in poor tracking. This may also limit the use in high heart rates, as the motion and thus frame to frame change increases relative to the frame rate. Speckle tracking and optical flow also require that patterns are visible in the grayscale image. Poor image quality will therefore degrade the resulting motion estimation. Doppler based techniques are less dependent on frame rate and image quality and are real time techniques. This thesis work will therefore be aimed at developing new ultrasound technique using the Doppler Effect to assess tissue properties. This chapter will only describe techniques, which are Doppler based. The Doppler techniques also present the advantage that they are available in most commercial ultrasound systems as real time imaging mode techniques. The description of the other non-Doppler based techniques can be found in the appendix section. The Doppler based techniques can be separated into 3

categories: spectral analysis, multiple beam techniques, and most recently spatial quadrature. The literature for each of these techniques is given below:

- Spectral broadening: (Newhouse, Varner et al. 1977; Newhouse, Furgason et al. 1980; Newhouse, LeCong et al. 1980; Censor and Newhouse 1986; Newhouse, Censor et al. 1987; Censor, Newhouse et al. 1988; Newhouse and Reid 1991; Cathignol, Dickerson et al. 1994; Lee, Chiang et al. 1999; Li, Cheng et al. 2001; Yeh and Li 2002; Yeh and Li 2002),
- Multiple beam techniques: (Uematsu 1981; Wei-qi and Lin-xin 1982; Ashrafzadeh, Dormer et al. 1989; Schrank, Phillips et al. 1990; Overbeck, Beach et al. 1992; Fei, Fu et al. 1994; Maniatis, Cobbold et al. 1994; Fei, Fu et al. 1995; Phillips, Kadi et al. 1995; Giarre, Dousse et al. 1996; Fei, Liu et al. 1997; Fei and Fu 1999; Hoskins 1999; Hoskins, Fish et al. 1999; Dunmire, Beach et al. 2000; Scabia, Calzolai et al. 2000; Steel and Fish 2002; Behar, Adam et al. 2003; Steel, Fish et al. 2003; Steel, Ramnarine et al. 2003; Steel, Ramnarine et al. 2004)
- Spatial modulation: (Anderson 1997; Anderson 1998; Anderson 1998; Jensen and Munk 1998; Jensen and Munk 1998; Anderson, Bohs et al. 1999; Jensen and Munk 1999; Anderson 2000; Munk and Jensen 2000; Anderson and Kerr 2001; Jensen 2001; Jensen 2001; Jensen 2003)

In the first three sections each of these approaches is described.

One of the main strengths of ultrasound imaging, is its real time capability (compared to other medical imaging modalities such as MRI, PETs, CT). Therefore it is crucial that a technique, which measures multi-component velocities, is not only

accurate but also real time. The sections 2.5 and 2.6 describe the real time capabilities and the performance of the different vector velocity techniques described in the previous sections. The choice of a technique to measure two- or three-component vector velocity for tissue motion will be highly driven by its capability to be implemented in real time and its accuracy.

2.2. Spectral Broadening

A theorem introduced by Newhouse, Censor, and Reid (Newhouse, Furgason et al. 1980; Censor, Newhouse et al. 1988; Newhouse and Reid 1990; Newhouse and Reid 1991) predicts that the Doppler spectrum bandwidth B_d originating from line flow crossing a sound field at the focal depth depends only on the flow to beam axis angle (c.f. **figure 2-1**). The conventional Doppler equation (2-1)

$$f_d = \frac{2}{\lambda} v \cos\theta \qquad (2\text{-}1)$$

can then be thus used in combination with the transverse Doppler equation (2-2)

$$B_d = \frac{k}{\lambda} v \sin\theta \qquad (2\text{-}2)$$

where k is constant, given by the ratio between the ultrasound transducer width, W, and its focal length F and λ is the wavelength. The constant, k, is proportional to the W/F ratio and therefore the broadening B_d of the spectrum is directly proportional to the transmit/receive aperture configuration. This phenomenon will be explained in the following paragraphs in more details. Equations (2-1) and (2-2) provide means for computing both components of the velocity vector v.

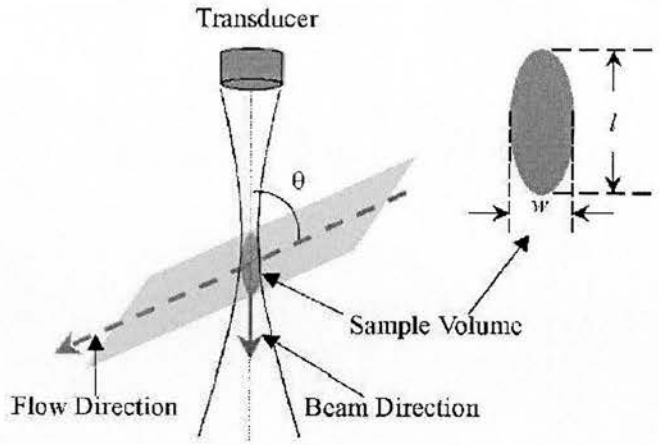

Figure 2-1: Schematic representation of Doppler angle and sample volume geometry

This phenomenon can be explained by two different approaches, the geometrical approach (Newhouse, Furgason et al. 1980) or the Fourier optics approach (Newhouse, Censor et al. 1987). However Guidi et al. (Guidi, Licciardello et al. 2000) have proven that these two explanations are no longer different. In this section the second approach is described.

It can be shown that in the far field or at the focal depth, the effective aperture is the convolution of the transmit and receive aperture functions (Censor, Newhouse et al. 1988) (c.f. appendix B). **Figure 2-2** and equation (2-3) illustrate the relationships between the aperture receive and transmit functions (respectively $a_T(x)$ and $a_R(x)$), the effective aperture ($E(x)$), and the radiation pattern for a linear array.

$$E(x) = a_T(x) \otimes a_R(x) \qquad (2\text{-}3)$$

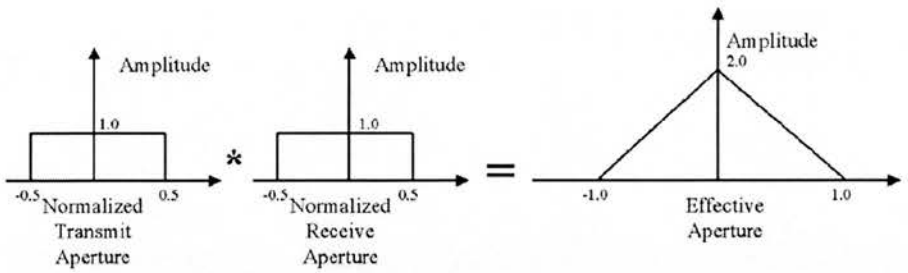

Figure 2-2: Relation between the receive and transmit aperture functions and the effective aperture.

This convolution theorem can be extended to the calculation of the Doppler spectrum (Newhouse, LeCong et al. 1980). In this case the spectrum $S(\mu)$ measured at the receiver is obtained by convolving the excitation spectrum received by a moving particle $G_T(\mu)$ by the excitation spectrum reemitted by the moving particle $G_R(\mu)$, then shifting the zero reference to the transmitter frequency ω:

$$S(\mu) = \delta(\mu - \omega_d) \otimes G_T(\mu) \otimes G_R(\mu) \qquad (2\text{-}4)$$

where ω_d represents the Doppler frequency and is equal to $\frac{2v_z}{c}$ ($v_z = v\cos\theta$), and μ is the transmit frequency. If there is no apodization in transmit and in receive, $G_T(\mu)$ and $G_R(\mu)$ can be considered as perfect rectangular functions in the frequency domain, centered at half the Doppler frequency with a width equal to $\frac{v_x}{c} * \frac{W}{F}$ ($v_x = v\sin\theta$). $G_T(\mu)$, and $G_R(\mu)$, are represented in **figure 2-3** and $S(\mu)$ in **figure 2-4**.

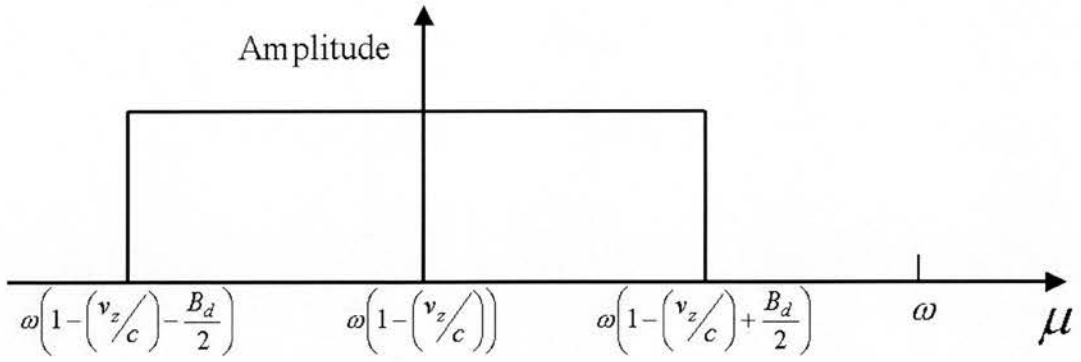

$$G_T(\mu) = G_R(\mu)$$

Figure 2-3: Transmit or receive amplitude spectrum for a constant velocity and oblique incidence.

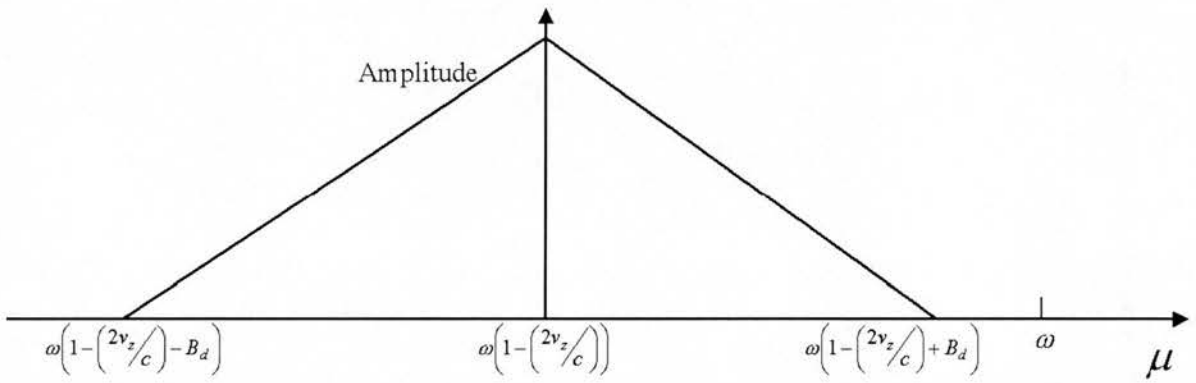

$$S(\mu) = \delta(\mu - \omega_d) \otimes G_{T(\mu)} \otimes G_R(\mu)$$

Figure 2-4: Effective amplitude spectrum for a constant velocity and oblique incidence.

Therefore from the two following equations (2-5) and (2-6) the direction (2-7) and the magnitude (2-8) of the velocity can be determined.

$$B_d = \frac{v_x}{c} \times \frac{W}{F} = \frac{v \sin\theta}{c} \times \frac{W}{F} \qquad (2\text{-}5)$$

$$f_d = \frac{2}{\lambda} v_z = \frac{2}{\lambda} v \cos\theta \qquad (2\text{-}6)$$

$$\theta = a\tan\left(\frac{B_d}{f_d}\times\frac{2cF}{\lambda W}\right) \qquad (2\text{-}7)$$

$$v = \frac{f_d \times \lambda}{2\cos(\theta)} \qquad (2\text{-}8)$$

Newhouse et al. (Newhouse, Dickerson et al. 1994) have extended this technique to a three-component vector Doppler. This is achieved by combining two frequency shifts measured from two separate transducers. When all three-velocity components are present, a triple peaked spectrum is obtained if both transmitters are simultaneously fired. Each side peak is due to transmission and reception by the same aperture, while the middle peak represents the combined cross-reception of the two apertures. The three components of the velocity vector are shown to be proportional to the separation of the side peaks, to their bandwidth and to the central peak shift, respectively.

Most of the publications presenting this technique (Newhouse, Furgason et al. 1980; Censor, Newhouse et al. 1988; Newhouse and Reid 1990; Cathignol, Dickerson et al. 1994; Newhouse, Dickerson et al. 1994; McArdle, Newhouse et al. 1995) are restricted to a single sample volume at a time. However this approach can be extended to a two-dimensional display by using an autoregressive spectrum model (Lee, Chiang et al. 1999; Li, Cheng et al. 2001; Yeh and Li 2002; Yeh and Li 2002). In this approach the FFT estimator is not used as the spectral bandwidth is assumed to be linearly proportional to the bandwidth of a Gaussian power spectrum and is estimated by using the autocorrelation function. The variance σ^2 can be approximated by:

$$\sigma^2 \approx \frac{2}{T^2}\left[1-\frac{|R(1)|}{R(0)}\right] \qquad (2\text{-}9)$$

where T denotes the emission interval of ultrasound pulses (i.e., PRF = 1/T), R(0) is the lag zero autocorrelation and R(1) is the lag one autocorrelation. Yeh and Li (Yeh and Li 2002) showed that the AR (AutoRegressive) method not only accurately estimated the Doppler bandwidth, it also outperformed the conventional FFT method at small Doppler angles. Since only a limited number of flow samples were used, real-time two-dimensional Doppler angle estimation is possible.

2.3. Multiple Beam Techniques

A large number of crossbeam vector Doppler ultrasound techniques for angle-independent velocity measurements have been proposed for the last 30 years (Dunmire, Beach et al. 2000). These techniques rely on the fact that a three-component velocity vector can be obtained by measuring the Doppler velocity at a given point from three linearly independent directions (Gehlbach and Alvarez 1981; Uematsu 1981). This may originate either from multiple transducers arranged in a variety of positions (Wei-qi and Lin-xin 1982; Ashrafzadeh, Dormer et al. 1989; Schrank, Phillips et al. 1990; Overbeck, Beach et al. 1992; Maniatis, Cobbold et al. 1994), through a single transducer divided in different sub-apertures, (Phillips, Kadi et al. 1995; Scabia, Calzolai et al. 2000), or through a variety of steering angles, (Fei, Fu et al. 1995; Fei, Liu et al. 1997; Hoskins 1997; Fei and Fu 1999). The first two approaches allow simultaneous acquisition of different angles, in contrast to the last technique where separate images have to be acquired for each angle. Regardless of acquisition, these estimates are then combined, taking the geometric relationships among the multiple beams into account, to estimate the two or three components of the vector velocity. In this section only one of these multiple beam approaches that uses two ultrasound transducers, is described. **Figure 2-5** illustrates such a device.

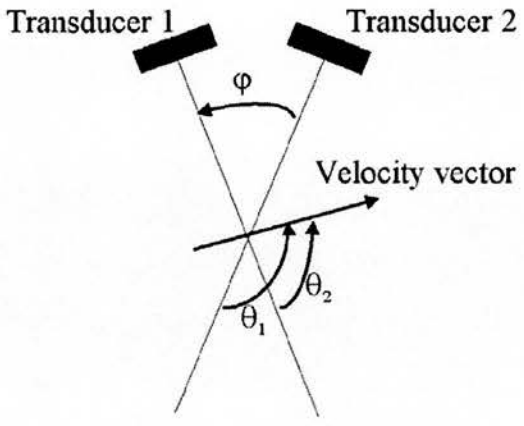

Figure 2-5: Cross-beam arrangement of transducers.

The two Doppler frequency shifts received at the center of each transducer are the following:

$$f_1 = \frac{2|v|}{c} f_0 \cos(\theta_1)$$
$$f_2 = \frac{2|v|}{c} f_0 \cos(\theta_2) \qquad (2\text{-}10)$$

where

$$\theta_1 = \theta_2 + \varphi \qquad (2\text{-}11)$$

The velocity component along the beam direction is:

$$v_z = |v| \cos\theta_1 = \frac{f_2 - f_1 \cos\varphi}{\sin\varphi} \qquad (2\text{-}12)$$

The velocity component perpendicular to the first beam:

$$v_x = |v| \sin\theta_1 = \frac{c}{2} \frac{f_1}{f_0} \qquad (2\text{-}13)$$

The magnitude and angle of the velocity can be found from v_z and v_X.

$$v = \sqrt{\left(v_z^2 + v_x^2\right)} \qquad (2\text{-}14)$$

$$\theta = \operatorname{atan}\left(\frac{v_x}{v_z}\right) \qquad (2\text{-}15)$$

This technique can be easily extended to a three-component Doppler technique by adding a third transducer, which will determine the y-component. Also to avoid using multiple transducers this technique can be applied to single transducer by dividing its aperture in two sub-apertures Phillips et al. (Phillips, Kadi et al. 1995) and Scabia (Scabia, Calzolai et al. 2000). Dumnire et al. (Dunmire, Beach et al. 2000) have published a review of cross beam vector Doppler techniques, which relates the evolution of the multi beam techniques for the last 30 years, from single-element multiple transmitter designs to systems having multiple subapertures and simultaneous acquisition. They concluded that the best designs for measuring vector velocity with cross beam devices is a single array transducer separated in several sub-apertures (at least two) allowing multiple beams to operate simultaneously.

Other slightly different approaches to multi-beam velocity estimation have been suggested that are correlation-based instead of Doppler-based. Routh (Routh, Pusateri et al. 1990), Bonnefous (Bonnefous 1988) and Hein (Hein 1994; Hein 1995) have described a system with multiple parallel beams. The velocity is found by cross-correlating responses from the different beams to find the movements of the targets. This method removes the depth-dependent angle problem but raises a new problem, which is creating equal and parallel beams throughout the region of investigation. Giarre (Giarre, Dousse et al. 1996) also developed a reconstruction method based on a geometrical approach to calculate the two-component, in-plane velocity vector using the information of two independent two-dimensional one-

component flow velocity measurements obtained from two closely spaced transducers.

2.4. Spatial Modulation

Spatial modulation is the most recently invented multi-component vector velocity technique. However this technique is closely related to multi-beam techniques and suffers from some of the same limitations.

In conventional ultrasound the Doppler Effect only allows measurement of the component of the velocity along the ultrasound beam since there is modulation of the ultrasound field only in the direction parallel to the beam (this is explained in more details in section 2.4.1). The Doppler Effect shifts the frequency of the modulation along the beam by a frequency proportional to the projection of moving target velocity along the beam. The modulation of the ultrasound field is either compressed (positive frequency shift, corresponding to movement towards the transducer) or expanded (negative frequency shift corresponding to the movement away from the transducer).

In the spatial modulation approach, this effect is extended to the lateral dimension by generating a modulation of the ultrasound energy perpendicular to the ultrasound wave propagation in the far field (or focal plane). So a moving target, crossing this field, introduces compression or dilation and therefore generates a Doppler frequency shift not only of the modulation in the axial direction but also in the direction perpendicular to it. Thus, the movement of a target is determined from a field with spatial oscillation in both the axial direction of the transducer and in one or two directions, transverse to the axial direction.

Two different methods, which employ the same phenomenon, have been developed: Spatial Quadrature (SQ) introduced by Anderson (Anderson 1997; Anderson 1998; Anderson 1998; Anderson, Bohs et al. 1999; Anderson 2000; Anderson and Kerr 2001) and the Vector Velocity estimator introduced by Jensen and Munk (Jensen 1993; Jensen and Munk 1998; Jensen and Munk 1998; Jensen and Munk 1999; Munk and Jensen 2000; Jensen 2001; Jensen 2001).

2.4.1. Spatial Quadrature

In Spatial Quadrature (SQ), the ultrasound point spread functions, which interrogate the sample volumes, are laterally weighted with odd and even functions (c.f. **figure 2-6**) to produce a modulation in the echo signals passing through each resolution volume. This modulation can be decoded to estimate the lateral component of the velocity. The even Point Spread Function (PSF) is produced by applying an, even, real receive apodization while the odd PSF is given by the multiplication of the real even PSF by the $j \cdot \mathrm{sgn}(x)$, where x represents the position within the aperture relative to its center, j the square root of -1 (c.f. **figure 2-6**).

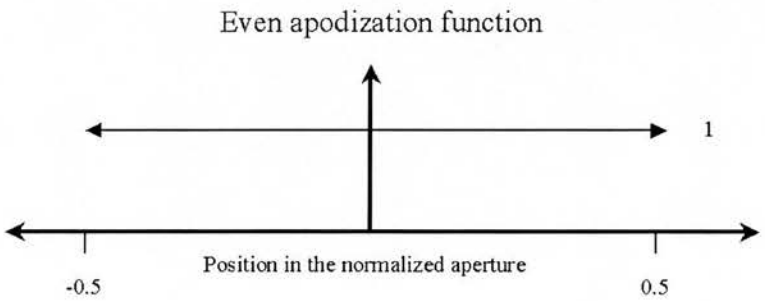

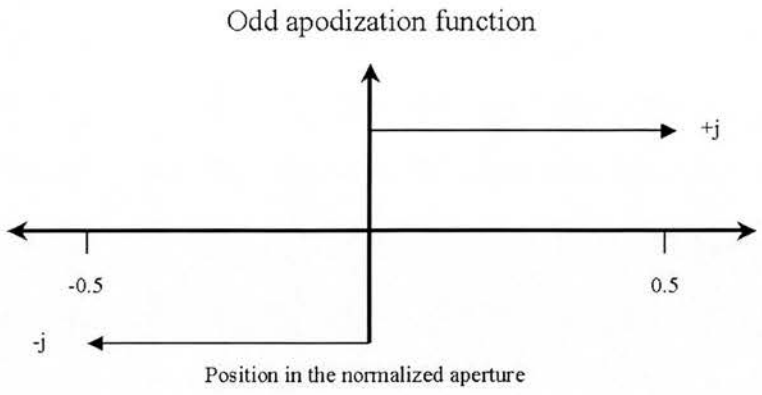

Figure 2-6: Spatial Quadrature even and odd apodization functions

The spatial quadrature phenomenon can be illustrated by a very simple example that consists of a two-element array (c.f. Appendix C). When applying an even and odd apodization to this array it can be demonstrated that the two signals created have real lateral modulations in quadrature (phase shift of 90 degrees) (c.f. Appendix C). This theory can be extended to a full array if we consider that in the aperture plane the even and odd apodizations are the convolution results of respectively $\delta(x \pm d_x) \otimes w(x)$ and $j \cdot \mathrm{sgn}(x)\delta(x \pm d_x) \otimes w(x)$, where x is the position in the array and $2d_x$ is the distance between the two Dirac functions. Then in the focal plane the resulting point spread function weightings in the lateral direction (x_F) are the Fourier transforms of the receive apodizations (c.f. **Figure 2.7**):

$$\delta(x \pm d_x) \otimes w(x) \xleftrightarrow{FourierTransform} 2\cos(2\pi k_{lat} x_L) \times W(x_L) \tag{2-16}$$

$$j \cdot \mathrm{sgn}(x) \cdot \delta(x \pm d_x) \otimes w(x) \xleftrightarrow{FourierTransform} 2\sin(2\pi k_{lat} x_L) \times W(x_L) \tag{2-17}$$

where $W(x_L)$ is the Fourier transform of w(x) and $k_{lat} = \omega d / 2\pi zc$.

Figure 2-7, reproduced from Anderson's paper (Anderson 1998), represents a conventional rectangular aperture with its PSF (top), the even (middle) and odd

(bottom) apodizations with their corresponding PSFs generated from the same per-channel RF data.

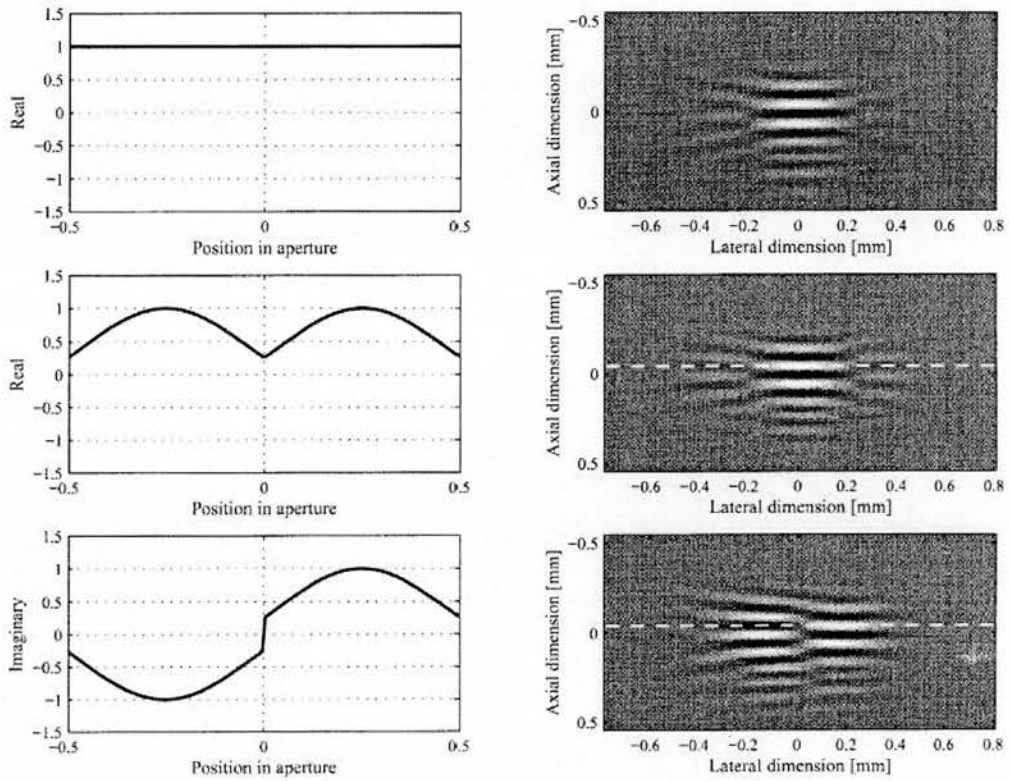

Figure 2-7: Three apodization functions paired with the Point Spread Functions (PSF) generated by their application to the same RF data set. The conventional PSF (top), created with uniform apodization, is compared with the even (middle) and odd (bottom) spatial quadrature PSFs created with the associated even and odd apodization functions. All three PSFs were synthesized using echo data from a 100 micrometer wire target in a water tank. The even PSF (middle, right) and the odd PSF (bottom, right) were processed as real and imaginary parts of a PSF with complex lateral modulation. The transmit pulse was a 3-cycle 7.5 MHz transmit pulse was recorded at a 36 MHz sampling rate on each of 128 elements of a 7.5 MHz linear array using a 28.2 mm aperture. The focus and region of interest was at 30 mm range. This figure is reproduced from Anderson (Anderson 1998).

In **Figure 2-7** all three PSFs were synthesized using echo data from a 100 micrometer wire target in a water tank. The transmit pulse was a 3-cycle 7.5 MHz transmit pulse was recorded at a 36 MHz sampling rate on each of 128 elements of a 7.5 MHz linear array using a 28.2 mm aperture. The focus and region of interest was at 30 mm range.

In spatial quadrature when the scatterer moves through the interrogated sample volume with both axial and lateral velocity components, the axial and lateral modulations are mixed together. Anderson (Anderson 2000) applied the heterodyning demodulation technique to separate the two velocity components. Overbeck et al. (Overbeck, Beach et al. 1992) first introduced this demodulation technique for the multiple beam vector Doppler approach. By combining linearly the two even and odd receive signals, it can be shown (appendix D) that the transverse velocity component v_x and the axial velocity component v_z can be expressed as:

$$\begin{aligned} v_x &= \frac{d\theta_{lateral} d_x}{2\pi 2T_{prf}} \\ v_z &= \frac{d\theta_{axial} c}{2\pi 4T_{prf} f_0} \end{aligned} \qquad (2\text{-}18)$$

where c is the sound velocity, v_z is the projection of the blood velocity on the beam axis, f_0 is the transmit frequency, T_{prf} the time between two pulses emissions, and where $d\theta_{lateral}$ and $d\theta_{axial}$ are expressed as:

$$\begin{aligned} d\theta_{lateral} &= 2\pi T_{prf} f_x \\ d\theta_{axial} &= 2\pi T_{prf} f_p \end{aligned} \qquad (2\text{-}19)$$

where $f_x = v_x/d_x$ and $f_p = 2v_z/c*f_0$.

By using the autocorrelation estimator R (c.f. Appendix D) it follows:

$$v_x = \frac{d_x}{2\pi 2T_{prf}} \arctan\left(\frac{\mathrm{Im}(R_1(1))\mathrm{Re}(R_2(1)) + \mathrm{Im}(R_2(1))\mathrm{Re}(R_1(1))}{\mathrm{Re}(R_1(1))\mathrm{Re}(R_2(1)) - \mathrm{Im}(R_1(1))\mathrm{Im}(R_2(1))}\right)$$
$$v_z = \frac{c}{2\pi 4T_{prf} f_0} \arctan\left(\frac{\mathrm{Im}(R_1(1))\mathrm{Re}(R_2(1)) - \mathrm{Im}(R_2(1))\mathrm{Re}(R_1(1))}{\mathrm{Re}(R_1(1))\mathrm{Re}(R_2(1)) + \mathrm{Im}(R_1(1))\mathrm{Im}(R_2(1))}\right) \quad (2\text{-}20)$$

The magnitude and angle of the velocity can be found from v_z and v_x.

$$v = \sqrt{\left(v_z^2 + v_x^2\right)} \quad (2\text{-}21)$$

$$\theta = a\tan\left(\frac{v_x}{v_z}\right) \quad (2\text{-}22)$$

2.4.2. Velocity Vector Estimator

This method differs from the previous method in that it uses a different scheme to generate the in phase and quadrature lateral modulations of the acoustic field.

As in the previous technique, the receive beamforming is designed to create the lateral spatial modulation. The technique starts from a very simple assumption that the far-field radiation pressure R(x) must contain a number of oscillations and must be bounded to have a finite ultrasound field. Thus the far-field pressure can be described as the product of a rectangular function modulated by a lateral oscillation:

$$R(x_L) = rect(L)\cos(2\pi f_x x_L) \quad (2\text{-}23)$$

From this, it is possible to deduce the receive aperture apodization that is equal to the Fourier transform of $R(x_L)$ if the Fraunhofer approximation is verified (far-field or in the focal plane). Let the receive aperture r(x) be the convolution of two functions $r_1(x)$ and $r_2(x)$:

$$r(x) = r_1(x) \otimes r_2(x) \quad (2\text{-}24)$$

then it follows:

$$R(x_L) = R_1(x_L) R_2(x_L) \qquad (2\text{-}25)$$

where $R_1(x_L)$ and $R_2(x_L)$ are respectively the Fourier transforms of $r_1(x)$ and $r_2(x)$.

The Fourier transform of the rectangular function of width L is:

$$r_1(x) = FourierTransform(rect(L)) = \frac{L}{z\lambda} \sin c\left(\pi x \frac{L}{z\lambda}\right) \qquad (2\text{-}26)$$

Here λ is the wavelength and z is the axial distance to the focal plane.

The Fourier transform of the cosine term is:

$$\begin{aligned} r_2(x) &= FourierTransform(\cos 2\pi f_x x_L) \\ &= \frac{1}{2z\lambda}\left[\delta\left(\frac{x}{z\lambda} + f_x\right) + \delta\left(\frac{x}{z\lambda} - f_x\right)\right] \end{aligned} \qquad (2\text{-}27)$$

Thus, the resulting receive apodization is the convolution of r_1 (x) and r_2 (x):

$$\begin{aligned} r(x) &= r_1(x) \otimes r_2(x) \\ &= \frac{L}{2z\lambda}\left[\sin c\left(\pi\left(\frac{x}{z\lambda} + f_x\right)L\right) + \sin c\left(\pi\left(\frac{x}{z\lambda} - f_x\right)L\right)\right] \end{aligned} \qquad (2\text{-}28)$$

The spatial frequency f_x of the lateral modulation is determined by the distance between the peaks of the two sinc functions and is:

$$f_x = \frac{x}{z\lambda} = \frac{1}{d_x} \qquad (2\text{-}29)$$

To be able to determine the signal of the velocity a one-sided spectrum should be employed to interrogate the region of interest. For the determination of axial velocities, the Hilbert transform of the signal is used. The same principle can be applied to determine transverse velocities by simultaneously having two receive transversally modulated fields 90-degree phase shifted, or more explicitly displaced at a distance of $d_x/4$ to yield spatial quadrature. Introducing positive and negative timing delays, which will tilt the two beams in opposite directions from the axial

direction, can produce the spatial quadrature. The time delays are calculated so the two beams at the focal point are symmetrically placed around the axial direction at a distance equal to $d_x/8$.

Jensen and Munk (Jensen and Munk 1999) also developed a new estimator for the Vector Velocity technique using a modified autocorrelation technique. This new estimator calculates independently the two components of the velocity. By combining linearly the two in phase and in quadrature receive signals, it can be shown (c.f. Appendix E) that the transverse velocity component v_x and the axial velocity component v_z can be expressed as:

$$\begin{aligned} v_x &= \frac{(d\theta_1 + d\theta_2)c}{2\pi 2T_{prf}} \\ v_z &= \frac{(d\theta_1 - d\theta_2)c}{2\pi 4T_{prf} f_0} \end{aligned} \tag{2-30}$$

where c is the sound velocity, v_z is the projection of the blood velocity on the beam axis, f_0 is the transmit frequency, T_{prf} the time between two pulses emissions, and where $d\theta_1$ and $d\theta_2$ are expressed as:

$$\begin{aligned} d\theta_1 &= 2\pi T_{prf}(f_x + f_p) \\ d\theta_2 &= 2\pi T_{prf}(f_x - f_p) \end{aligned} \tag{2-31}$$

where $f_x = v_x/d_x$ and $f_p = 2v_z/c*f_0$.

By using the autocorrelation estimator R (c.f. Appendix E) the same equations than (2-20)-(2-22) can be applied to obtain v_x, v_z, v, and θ.

The heterodyning demodulation and the new estimator proposed by Jensen and Munk (Jensen and Munk 1999) result in the same autocorrelation estimator.

The spatial quadrature or velocity vector technique is derived from the multiple crossbeam techniques. It can be compared to the single array transducer, two sub-aperture multi-beam design. Indeed, by apodizing and combining the signals received by the two sub-apertures with specific functions (odd and even functions), it can be shown that these two methods are equivalent. Jensen and Anderson have adopted a Fourier description of the spatial quadrature method while multi-beam techniques are described with a geometrical approach. However the main improvement of the spatial quadrature technique is that the transversal modulation created in the far field can be controlled by the receive apodizations (in the limit of the aperture size).

2.5. Real Time Implementation

Real time visualization of velocity field is a very important factor for these techniques to be adopted in a clinical environment. It is driven essentially by the computational demand and the hardware capabilities of ultrasound systems.

2.5.1. Spectral Broadening

As noted Tortoli et al. (Tortoli, Guidi et al. 1992), the spectral broadening technique does not require any specialized pulsed Doppler electronics. The only requirements are that the spectrum presents a good signal to noise ratio and the high pass filters can work with a properly low cutoff frequency. The computation of the mean frequency and bandwidth is almost negligible compared to other techniques and is widely available in commercial ultrasound system as real time tool (mean and peak frequency).

2.5.2. Multiple Beam Techniques

From a computational point of view multiple beam techniques are almost insignificant (small amount of trigonometric relations to calculate or use of the heterodyning demodulation with the autocorrelation estimator). The main problem is to gather the signals from the different beams to perform the vector Doppler calculation and to perform all the processing necessary to extract the spectra (high pass filtering, Fast Fourier Transform). The hardware of the ultrasound system has to support a parallel architecture and multiple signal paths in the case of simultaneous acquisitions of these signals. From an acquisition point of view, it can be difficult to apply large multi-beam transducers on the body, especially in cardiology, where the transducer is placed between ribs.

2.5.3. Spatial Modulation

This method uses two ultrasound beams for sampling the in-phase and quadrature component of the lateral field and a set of samples (in-phase and quadrature in both time and space) is taken for each pulse-echo line. Therefore some sort of parallel architecture is required to be able to implement this technique. The four samples (in-phase and quadrature in both time and space) are then used in an autocorrelation approach that yields both the axial and the lateral velocity, and thus the velocity vector. This method has the advantage that it requires only one standard transducer with modified beamformation and some parallel architecture to be able to process the multiple signals independently. The signal processing preceding the beamformation can be implemented using standard signal processors.

2.6. Performance

Performance of a technique can be expressed by its ability to make measurements with a minimal error (small standard deviation) and a small bias. However in the clinical context, reproducibility is crucial for the validation of a new technique. High reproducibility is linked to low measurement error. Therefore it is important to distinguish between systematic (bias) and random errors (standard deviation). The former may be of little importance if they affect all measurements to a similar degree, so that comparisons of the measured data between patients and also within the same patient present the same bias for which it may be possible to correct. Random errors, on the other hand, may invalidate such comparisons. Although random errors may be reduced by repeated measurements, it is not the preferred practice to perform multiple repeat measurements on the same patient in one sitting in the clinical environment.

2.6.1. Spectral Broadening

Measurements on thread phantoms have shown good agreement with theoretical prediction, since spectra evaluated at different depths and different velocities all exhibited a nearly triangular shape with identical bandwidth (Tortoli, Guidi et al. 1992). Tortoli et al. also reported that the thread measurements showed that the expected linear relationship between the bandwidth and the transverse velocities had less than 10% fluctuation (standard deviation). Hoskins (Hoskins 1999) showed that the maximum frequency of the Doppler spectrum and spectral broadening as a function of the beam-thread angle have a very good agreement between the measured and predicted values over the whole range of angles (standard deviation was less than 10 %) (c.f. **figure 2-8**).

Experiments using flow phantoms are more problematic because there is a velocity gradient within the sample volume that, in itself, will give rise to a range of Doppler frequency shifts. Cloutier (Cloutier, Shung et al. 1993) and Tortoli (Tortoli, Guidi et al. 1992) showed that the relative bandwidth does not vary with the mean blood velocity and with the beam sample volume size with a beam vessel angle above 84 degrees in steady laminar flow models. However at lower angles, the Doppler bandwidth noticeably increases as the sample size (pulse length) is increased.

For laminar flow and low Doppler angles Tortoli et al. (Tortoli, Guidi et al. 1993) concluded that the sample volume should be minimum (down to 1 mm) to avoid velocity gradient within the range cell. For small sample volume (1 mm) the bandwidth measurement works well in conditions where the noise ratio of the spectrum is below the threshold fixed at 1% of the peak power. This threshold corresponds to a minimum signal to noise ratio of 20 dB, which is in the order of blood to clutter ratio for superficial and deep flow clinical applications, to be able to determine correctly the spectrum bandwidth.

Cloutier et al. (Cloutier, Shung et al. 1993) also raised the problem of non-stationarity of the Doppler signal during the acquisition period. Using a pulsatile laminar flow model (phantom) they showed that the relative Doppler bandwidth invariance did not hold during acceleration and deceleration of blood flow. They concluded that even when using a small window (2.5 ms) to minimize non-stationarity effects, broadening due to spectral leakage dominated over geometric broadening. Their advice was therefore to use a spectral estimator other than Fourier transform to assess spectral broadening.

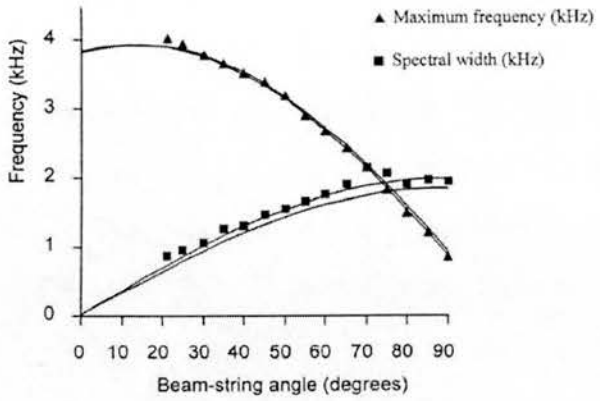

Figure 2-8: Measured and calculated spectral width and maximum frequency as a function of beam-string angle. This figure is reproduced from Hoskins (Hoskins 1999), Ultrasound in Medicine, 1999, 25, 583-592 (with permission).

2.6.2. Multiple Beam Techniques

A number of publications (Phillips, Kadi et al. 1995; Hoskins 1997; Scabia, Calzolai et al. 2000) present extensive performance testing with string phantom for multiple beam techniques. In these experiment setups, string phantoms are used to investigate the dependence on the angle between the beam and the moving string. In all these papers a good correlation between the beam-string angle and the vector Doppler estimated beam-string angle was found for the string phantom (c.f. **figure 2-9**). In **figure 2-9** extremely large errors in velocity for beam-string angle above 70 degrees can be observed (52 % of bias with a variation of 27%) for conventional Doppler ultrasound. However with a multi-beam technique the maximum velocity estimation showed a bias and a variation less than 2%. The angle estimation presented also a very good accuracy (0% of bias with a variation of 1.3%).

Flow phantoms have been used to evaluate the robustness of these techniques in the presence of velocity, acceleration, and direction gradients, all of which have

influence even more in the case of stenotic vessels. Even though the true direction of motion in a flow phantom is not known, it has been shown that the variation of the estimated velocities can give an appreciation of the error of the beam-direction of motion angle. In the case of stenotic flow phantom it has been shown (Hoskins 1997) that conventional Doppler presents a very large variation with beam-vessel angle for estimated maximum velocity. This variation can go up to 35% in stenosis model. However when using a multiple beam approach the variation of the estimation of the maximum velocity within the post-stenotic jet for beam-vessel angle ranging from 40 to 80 degree decreased to 2% therefore improving the reproducibility of the Doppler technique.

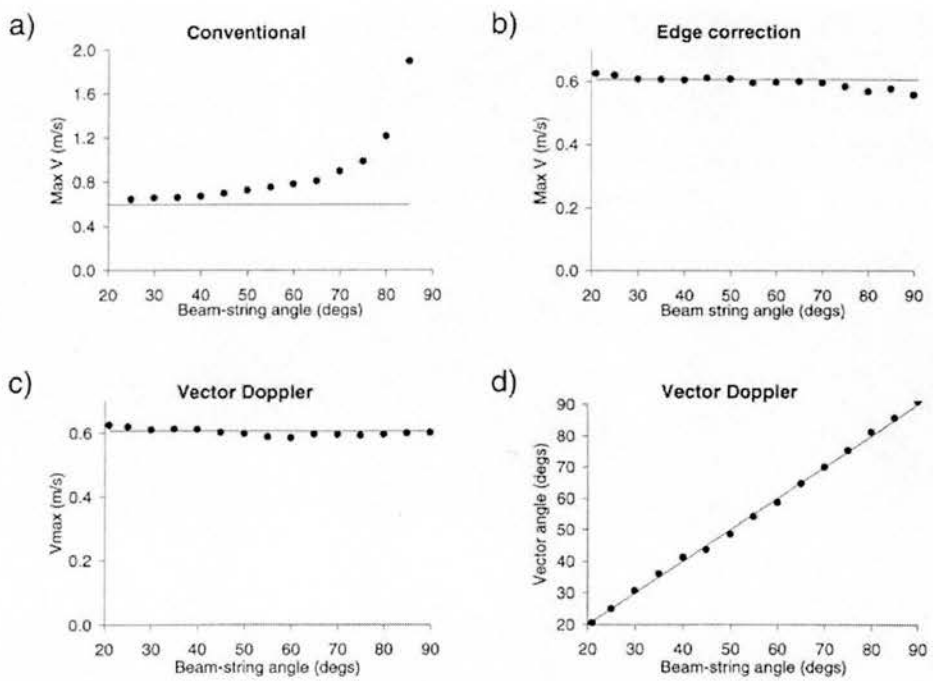

Figure 2-9: Results from the string phantom. Maximum velocity estimated using (a) conventional Doppler, (b) angle correction with respect to the edge of the Doppler aperture, and (c) vector Doppler. The estimated beam string angle is shown in (d). This figure is reproduced from Hoskins, (Hoskins 1997) Ultrasound in Medicine, 1997, 23, 889-897 (with permission).

The multi-beam technique, when using a single transducer divided in multiple receive sub-apertures, (Phillips, Kadi et al. 1995; Scabia, Calzolai et al. 2000), suffers from a lower lateral resolution than conventional single-beam Colour Flow Imaging, due to the fact that the receive apertures used in multiple beam are smaller than in single beam. The sensitivity is also decreased in the case of the multiple receive sub-apertures because less transducer elements are used to perform the beamformation and summation.

2.6.3. Spatial Modulation

This method has been tested by using simulation (Jensen and Munk 1998) and using a real time prototype on phantom data (Jensen and Munk 1999).

The simulation is performed using the impulse response method developed by Tupholme (Tupholme 1969) and Stepanishen (Stepanishen 1971) in the implementation developed by Jensen and Svendsen (Jensen and Svendsen 1992). A vessel of 10-mm diameter is placed at 70 mm from the center of the transducer array. All the scatterers within the vessel have a steady velocity of 1 m/s (plug flow) while the vessel angle varies from 0, to 90 degrees. An ensemble length of 50 has been used to create this data. The results are illustrated in **figure 2-10**.

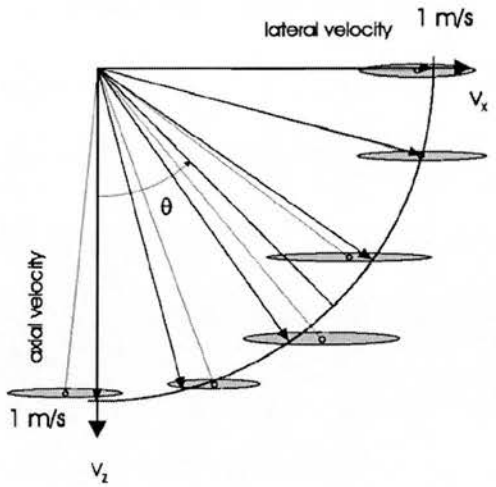

Figure 2-10: Results of the simulation for the Vector Velocity technique. Velocity of targets 1m/s. Angles: 0, 15, 35, 55, 75, 90 degrees. This figure is reproduced from Jensen, (Jensen and Munk 1998) IEEE Transactions UFFC, 1998, 45, 837-851.

The true velocity vectors are indicated by the small arrows. The gray ellipses for each velocity estimate indicate the standard deviations for both the axial (short axis) and the lateral estimation (long axis) with the mean value represented as in the center of the ellipse. The overall mean velocity is 0.99 m/s, axial standard deviation is 0.015 m/s and lateral standard deviation is 0.196 m/s.

In vitro, the method was tested using a very fine grain sponge to obtain a backscatter signal. This sponge was angulated and moving relative to the transducer. The transducer was angulated at 90, 75, 60 and 50 degrees. The ensemble length used was 20. With the autocorrelation-based estimator, the bias on the estimate of the lateral velocity is approximately –8%. The overall standard deviation, averaged over all angles, is 10%. The use of the new autocorrelation estimator decreased the bias by 10%. This autocorrelation technique allows the simultaneous estimation of the transverse and axial velocity components. This improvement in accuracy is certainly

due to the fact that not only the phase of the two components is taking into account but also their power.

The underestimation of the absolute velocity is due to the very broad lateral frequency. The transverse velocity accuracy depends on the frequency of the oscillations generated in the far field. The frequency of these oscillations is proportional to the distance between the two peaks of the receive apodization. Indeed the larger the transducer is, the greater the distance in between the two peaks can be and therefore the smaller the modulation will be (the greater the frequency will be). However the lateral modulation period is in general larger than that of the axial modulation and therefore for a given velocity the change in phase for the axial signal will be smaller than the change in phase for the transverse signal. The autocorrelation technique allows compensation for this problem (Jensen and Munk 1999). By using a lag k greater than one for the transversal component in the autocorrelation estimator the transverse phase sensitivity is increased.

The signal to noise can also be improved by averaging the autocorrelation estimates along the axial direction (Jensen and Munk 1999).

The spatial modulation, like the multiple beam technique, also suffers from a lower lateral resolution than conventional single-beam colour flow imaging, due to the fact that the receive apertures used are apodized. The sensitivity is also reduced in the case of spatial modulation for the same reason.

2.7. Discussion and Conclusion

The techniques described in this chapter have all been developed to detect multi-component velocity for blood flow applications. Can these techniques be applied to estimate two or three-component velocity for tissue motion?

The spectral broadening method relies on the estimation of the velocity variance to assess the transversal velocity component. The variance estimation precision is directly linked to the ensemble length (in the case of colour flow) or the number of samples used in the FFT (fast Fourier transform) to generate the Doppler spectrum (in the case of pulsed wave Doppler). The larger the ensemble or the number of samples the better the estimation. However in TDI (c.f. chapter 1) the ensemble length is very small (2 to 4 pulses per line) to allow very high acquisition frame rates (>100 Hz) and with this short ensemble length, the estimation of the variance is not reliable. To improve the estimation, the ensemble length has to be increased and therefore the frame rate will decrease limiting the real time aspect of TDI. Moreover with larger ensemble length, because the tissue velocity is highly non-stationary (high acceleration and deceleration in systole and early diastole >2cm/s^2), the variance of the Doppler spectrum will not be only due to transverse motion but also to acceleration and deceleration. The estimation of the transverse velocity will be biased by this factor. Therefore this technique just like multi-component flow velocity estimation is not appropriate to assess multi-component tissue velocities. The multi-beam and spatial modulation techniques are somewhat equivalent. They both used a partial receive aperture and therefore the lateral resolution of the tissue Doppler imaging will be reduced. The slight difference between the two techniques is that the receive apertures in spatial modulation are apodized (windowed) allowing a narrower lateral frequency modulation with lower side lobes in the focal plane. Therefore a more precise estimate of the lateral velocity component with the spatial modulation approach could be achieved (this remains to be proven), but a lower lateral resolution than in the multi-beam technique will be observed. By apodizing

the receive sub-apertures there will also be a loss of receive signal that might be crucial in colour flow where blood signals are very weak. In Tissue Doppler Imaging this loss of signal is less important because the tissue signal is much stronger (40 to 60 dB higher than the flow signal). Because of the potentially better lateral velocity estimation, spatial modulation is the preferred techniques to perform multi-component tissue velocity estimation. However to implement the spatial modulation method the apodizations of the receive apertures need to be changed as a function of receive depth to allow dynamic receive focusing. The system used for this study (Philips Ultrasound, HDI 5000) has only the capability to increase monotonically the gain on each element and therefore cannot provide a dynamic focalization as well as sub-aperture apodizations. The multi-beam technique is the most appropriate (and feasible) to measure multi-component tissue velocities as they can be acquired with a low ensemble length and in real time (by modifying the signal processing and the hardware of existing ultrasound device). Therefore the multi-beam technique will be used to estimate two-component tissue velocity in the following chapters.

2.8. Appendices

2.8.1. Appendix A: Non Doppler Vector Velocity Techniques

2.8.1.1. Edge Detection

Edge detection is a very active area especially in the field of echocardiography. This approach is essentially used to track cardiac wall and vessel wall structures throughout the cardiac cycle, as well as, to determine the geometry of the left ventricle or to measure the motion of vessel walls.

Wall tracking is a method, which measures tissue motion with ultrasound echoes by tracking the rising edge of the echo reflected from a tissue/blood interface, such as vessel wall or cardiac muscle. Powalowski (Powalowski 1988) has used this technique to measure the motion of vessel walls. He uses a simple threshold to extract the interior and exterior edges of the vessel walls. More complex techniques are used to extract edges in cardiac applications. Geiser (Geiser, Oliver et al. 1988; Geiser, Conetta et al. 1990) and Friedland (Friedland and Adam 1989) have developed an automatic algorithm to detect epicardial and endocardial borders of the ventricular cavities. These algorithms consist of three basic steps:

1. image preprocessing
2. application of an edge operator to determine pixels likely to represent an edge
3. "tidying" of the image.

The image preprocessing is intended to suppress the speckle component of the ultrasound image and to amplify the specular targets, which represent the structure of interest along the borders. This preprocessing consists of convolving spatially and temporally the ultrasound image with a low pass filter. The second step consists of extracting the endo- and epicardial continuous borders by using an edge detection algorithm. This step is probably the most important, since it will create a map of edges contained in the image. Several techniques to extract edges exist. One of the standard ways to find an edge is to look for a change in the amplitude of gray level (Canny 1986). These brightness changes can be characterized by gradients or first derivative operators. The last step is tidying the image by the deletion of extraneous edge pixels and filling in gaps to form a continuous boundary.

The center of the ventricle can then be estimated by calculating the centroid of endo- and epicardial continuous borders. Using this kind of representation circumferential function can be assessed by measuring the radial motion of the endocardium, the radial wall thickening, or the changes in cavity section areas (Buda, Delp et al. 1983; O'Boyle, Parisi et al. 1983). Wall motion can also be depicted as a three-component plot (Schiller 1985) where the x-axis represents the segment, and the z-axis represents the radial motion of the endocardium throughout the cardiac cycle.

2.8.1.2. Time-Domain Velocimetry

A number of speckle tracking methods have appeared in the literature in the last 15 years: Gardiner and Fox (Gardiner and Fox 1989), Wilson and Gill (Wilson and Gill 1993), Trahey et al. (Trahey, Allison et al. 1987), Dotti et al. (Dotti, Lombardi et al. 1992), Hein and O'Brien (Hein and O'Brien 1993), and Bonnefous and Pesque (Bonnefous and Pesque 1986). The time-domain approach estimates the velocity of a target on the displacement of the scatterers between pulses. This technique is strictly not a Doppler approach, but is closely related. The primary advantage of this technique over a pulsed Doppler system is the theoretical elimination of aliasing. The use of 2-D correlation to estimate motion from ultrasound B-mode images was first reported by Trahey (Trahey, Hubbard et al. 1988) for angle-independent blood flow detection.

2D-speckle tracking or region-matching technique is one application of time domain analysis. Two standard region-matching techniques will be presented in this section:

- Crosscorrelation
- Sum-of-absolute differences

2D-speckle tracking measure velocities by comparing the speckle pattern in small kernel (X wide and Y high) in a first image acquisition to each possible match in a larger surrounding search (2N x 2M) region in second image acquisition by maximizing *CRS* coefficient or minimizing *SAD* coefficient (c.f. **figure 2-11**). The displacement vector D can be used to calculate the velocity of the kernel region (both magnitude and direction), which can then be superimposed on the B-scan.

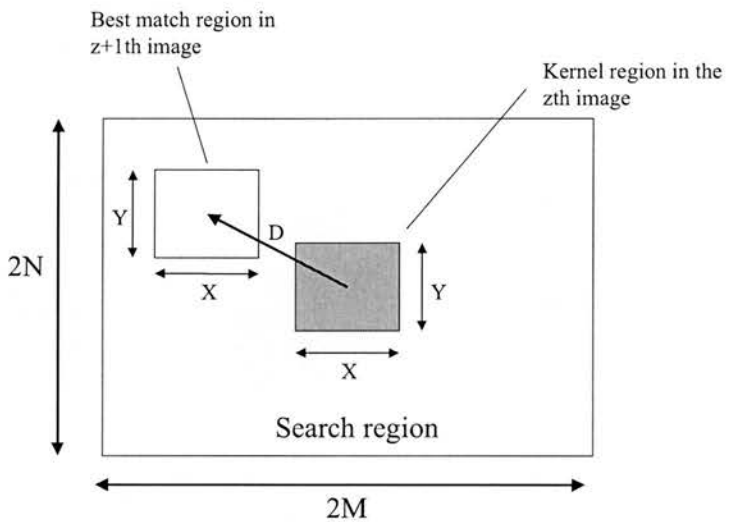

Figure 2-11: Geometry for 2-D speckle tracking. A kernel region (shaded) of (XxY) pixels is identified in the zth image and compared with all possible matching location in a (2Mx2N) search region.

1. Crosscorrelation

Crosscorrelation is a 2D technique based on comparison of grayscale intensities between consecutive frames. Given a target with X+1 columns and Y+1 rows ($x=x_0 \ldots x_0+X$ and $y=y_0 \ldots y_0+Y$) at frame t, its position at frame t+1 can be estimated

by finding the column-and row shifts m and n which maximize the normalized crosscorrelation coefficient *CRS(m,n)* (equation (2-32))

$$CRS(m,n) = \frac{\sum_{x=x_0}^{x_0+X}\sum_{y=y_0}^{y_0+Y}\left\{G(x,y,t)-\overline{G}_t\right\}\left\{G(x+m,y+n,t+1)-\overline{G}_{t+1}\right\}}{\sqrt{\sum_{x=x_0}^{x_0+X}\sum_{y=y_0}^{y_0+Y}\left\{G(x,y,t)-\overline{G}_t\right\}^2\sum_{x=x_0}^{x_0+X}\sum_{y=y_0}^{y_0+Y}\left\{G(x+m,y+n,t+1)-\overline{G}_{t+1}\right\}^2}} \quad (2\text{-}32)$$

where $\overline{G}_z$ and $\overline{G}_{z+1}$ denote the mean value of the target region at frame t and the candidate region at frame t+1, respectively (equations (2-32) and (2-33)):

$$\overline{G_t} = \sum_{x=x_0}^{x_0+X}\sum_{y=y_0}^{y_0+Y} G(x,y,t) \quad (2\text{-}33)$$

$$\overline{G_{t+1}} = \sum_{x=x_0}^{x_0+X}\sum_{y=y_0}^{y_0+Y} G(x+m,y+n,t+1) \quad (2\text{-}34)$$

2. Sum-Of-Absolute-Differences

An alternative displacement estimate can be obtained by finding the column and row-shifts m and n which minimizes the sum-of-absolute-differences *SAD(m,n)* (equation (2-35))

$$SAD(m,n) = \sum_{x=x_0}^{x_0+X}\sum_{y=y_0}^{y_0+Y}\left|G(x,y,t)-G(x+m,y+n,t+1)\right| \quad (2\text{-}35)$$

This technique has been extended to three-component detection by Bashford and Von Ramm (Bashford and von Ramm 1995)(Bashford and von Ramm 1995), and Morsy and Von Ramm (Morsy and Von Ramm 1998) by using a kernel volume. Performing conventional crosscorrelation or a SAD search in three-dimension has the disadvantage of being computationally expensive. To overcome this problem feature tracking is proposed (Bashford and von Ramm 1995; Morsy and Von Ramm 1998) to optimize the computation time. It is based on identifying and tracking a set

of discrete features used in successive ultrasound images. Features used include peaks of image amplitude and zero crossing of RF lines. In two-dimension feature patterns will appear as three-component representations of amplitude. The feature pattern locator is represented by the tip of the pattern, and the matcher is represented by the pattern shape.

2.8.1.3. Optical Flow Technique

Optical flow, or instantaneous velocity field calculation, has first been introduced by Horn and Schunck (Horn and Schunck 1981). This technique is used to determine motion in any types of images, from video sequences to successive ultrasound images recorded from an ultrasound system. A relatively simple iterative algorithm for velocity estimation is based on the spatio-temporal gray-level derivatives in successive frames. The vector velocity field, recovered by this technique, does not correspond to the real three-component velocity field of the objects being imaged, but to its projection on the image plane. However, in two-component ultrasound imaging, the optical flow quantitatively describes the motion seen by an observer on the video monitor.

In this approach, the assumption is that motion introduces displacement of points in the 2D imaging plane but does not affect their brightness so that

$$G(x+\delta x, y+\delta y, t+\delta t) = G(x, y, t) \quad (2\text{-}36)$$

where G(x,y,t) represents the brightness of the pixel located at abscissa x and ordinate y of the two component image at time t. It can be shown that the following relation exists between the brightness and the velocity:

$$u\frac{\delta G}{\delta x}+v\frac{\delta G}{\delta y}+\frac{\delta G}{\delta t}=0 \qquad (2\text{-}37)$$

where u and v denote the velocity projections along axis x and axis y respectively. It is important to appreciate that the optical flow algorithm is only fully valid when the brightness varies linearly along x, y directions and in time (t) (so that the second- and higher-order differentials are actually equal to zero). Equation (2-37) contains two unknowns (u and v) and, consequently, one more equation is required to obtain a solution. Horn and Schunck suggested that an additional equation could be formulated by imposing a smoothness constraint on the spatial derivatives of the x- and y-velocity components according to equation (2-38)

$$\left(\frac{\delta u}{\delta x}\right)^2+\left(\frac{\delta u}{\delta y}\right)^2+\left(\frac{\delta v}{\delta x}\right)^2+\left(\frac{\delta v}{\delta y}\right)^2\rightarrow \min \qquad (2\text{-}38)$$

The optical flow algorithm of Horn and Schunck is based on finding a solution, which minimizes a weighted combination of the errors in the optical flow and smoothness constraints. The weighted error E(λ) can be expressed as equation (2-39)

$$E(\lambda)=\iint\left[\begin{array}{l}\left[u\frac{\delta G}{\delta x}+v\frac{\delta G}{\delta y}+\frac{\delta G}{\delta t}\right]^2\\ +\lambda*\left[\left(\frac{\delta u}{\delta x}\right)^2+\left(\frac{\delta u}{\delta y}\right)^2+\left(\frac{\delta v}{\delta x}\right)^2+\left(\frac{\delta v}{\delta y}\right)^2\right]\end{array}\right]dxdy \qquad (2\text{-}39)$$

where the parameter λ should be assigned a small value if the image gray levels are accurate (i.e., the optical flow constraint is likely to be valid) and a large value if they are noisy (so that the smoothness constraint is given more weight). The value of λ can be determined by looking at statistical properties of the ultrasonic images such as variance. The condition of minimum error results in the following iterative solution:

$$u^{i+1} = \bar{u}^{i} - \frac{\delta G}{\delta x}\left[\bar{u}^{i}\frac{\delta G}{\delta x} + \bar{v}^{i}\frac{\delta G}{\delta y} + \frac{\delta G}{\delta t}\right] \Big/ \left[\lambda + \left(\frac{\delta G}{\delta x}\right)^2 + \left(\frac{\delta G}{\delta y}\right)^2\right] \qquad (2\text{-}40)$$

$$v^{i+1} = \bar{v}^{i} - \frac{\delta G}{\delta y}\left[\bar{v}^{i}\frac{\delta G}{\delta x} + \bar{v}^{i}\frac{\delta G}{\delta y} + \frac{\delta G}{\delta t}\right] \Big/ \left[\lambda + \left(\frac{\delta G}{\delta x}\right)^2 + \left(\frac{\delta G}{\delta y}\right)^2\right] \qquad (2\text{-}41)$$

where the superscript "i" denotes the iteration index, u and v are the local means of the x- and y-velocity components, and the various partial derivatives are calculated as finite differences from local sets of image data.

Equations (2-40) and (2-41) show that a new pair of values (u, v) is calculated as the averages of surrounding values minus an adjustment which in velocity space is in the direction of the gray-level gradient. Once the velocity vector (u,v) has been determined for each pixel location, the direction and magnitude of the flow can be plotted at each pixel location.

One of the applications of optical flow is in the field of echocardiography. Mailloux, Meunier, Bertrand (Mailloux, Bertrand et al. 1984; Mailloux, Bleau et al. 1987; Meunier, Bertrand et al. 1988) have applied optical flow to compute interframe velocity field of the heart, which shows the direction of motion of local areas of cardiac muscle during contraction.

The analysis of cardiac wall thickness can be used to diagnose conditions such as ischemia and infarction. The authors also extended the optical flow technique by taking into account different linear transformations such as, translation, rotation, deformation (contraction and expansion) that allowed a better description of the heart model. These linear components can be combined with the optical flow algorithm by adding a local linearity constraint. Indeed any vector field can be described by linear equations of the form:

$$\begin{bmatrix} u(x,y) \\ v(x,y) \end{bmatrix} = \begin{bmatrix} a \\ b \end{bmatrix} + \begin{bmatrix} A & B \\ C & D \end{bmatrix} \begin{bmatrix} x \\ y \end{bmatrix} \tag{2-42}$$

This linear field can be described as the sum of four vector fields, which represent physiologic mechanical properties. This can be easily seen if the linear equation is rewritten as:

$$\begin{aligned} \begin{bmatrix} U(x,y) \\ V(x,y) \end{bmatrix} &= \begin{bmatrix} a \\ b \end{bmatrix} + (C-B)/2 \begin{bmatrix} 0 & -1 \\ 1 & 0 \end{bmatrix} \begin{bmatrix} x \\ y \end{bmatrix} \\ &+ (A+D)/2 \begin{bmatrix} 1 & 0 \\ 0 & 1 \end{bmatrix} \begin{bmatrix} x \\ y \end{bmatrix} \\ &+ \begin{bmatrix} (A-D) & (B+C) \\ (B+C) & (D-A) \end{bmatrix} \Big/ 2 \begin{bmatrix} x \\ y \end{bmatrix} \end{aligned} \tag{2-43}$$

The first right-hand term of equation (2-43) describes a translation field, the second, third, and fourth describe respectively, rotational, divergent (strain), and shear field (shear strain). The components a, b, A, B, C, and D can be obtained after computing the optical flow and then minimizing the following equations:

$$\sum_{i=1}^{N} \left[\left(a + Ax^i + By^i - u^i \right)^2 + \left(b + Cx^i + Dy^i - v^i \right)^2 \right] \tag{2-44}$$

where the superscript "i" denotes the iteration index and N the total of iterations. To minimize (2-44) the method of least squares is used, where the summation is taken over all points in the image where the velocity is observed.

Optical flow algorithms can theoretically be used to estimate blood flow from the changing speckle pattern in a B-scan image. However this technique requires a very high signal to noise ratio and is therefore not very reliable for these applications.

2.8.2. Appendix B: Effective Aperture

This theory relies on the fact that in the far field or at focal depth, a continuous wave radiation pattern $P_T(s)$ of a linear array is given by the Fourier transform of the transmit aperture function $a_T(x)$:

$$P_T(s) = \int_{-\infty}^{+\infty} a_T(x) e^{i2\pi xs} dx \qquad (2\text{-}45)$$

where $s = \sin(\theta), \theta$ is the angle measured from the perpendicular to the array, and x the element location in wavelength. Similarly, the radiation pattern that is seen by the array $P_R(s)$ is given by the Fourier transform of the receive aperture function $a_R(x)$. The pulse echo radiation pattern $P_{TR}(s)$ is given by the product of the transmit radiation $P_T(s)$ and the receive radiation $P_R(s)$:

$$P_{TR}(s) = P_T(s)\ P_R(s) \qquad (2\text{-}46)$$

This is equivalent to convolving the transmit aperture function $a_T(x)$ with the receive aperture function $a_R(x)$ and taking the Fourier transform of the result

$$P_{TR}(s) = F\left(a_T(x) \otimes a_R(x)\right) \qquad (2\text{-}47)$$

The convolution of the transmit and receive aperture functions is often called the effective aperture of the array E(x):

$$E(x) = a_T(x) \otimes a_R(x) \qquad (2\text{-}48)$$

The effective aperture can be thought of as the receive aperture that would produce an identical radiation pattern if the transmit aperture were a point source.

2.8.3. Appendix C: Spatial Quadrature with a two Element Array

The two elements receiving signals are denoted A and B. A moving target located in the far field or at the focal point at position (x, z) is illuminated with monochromatic radiation of frequency ω. The receive aperture has the form $\delta(x \pm d_x)$.

The odd function introduces a 90-degree phase advance for the positive element $\delta(x + d_x)$ and a 90-degree phase delay for the negative element $\delta(x - d_x)$. The two signals received at A and B have respectively the following delays R_A/c and R_B/c, where c is the sound speed in the medium and R_A and R_B are:

$$R_A = \sqrt{z^2 + (d_x + x)^2}$$
$$R_B = \sqrt{z^2 + (d_x - x)^2} \qquad (2\text{-}49)$$

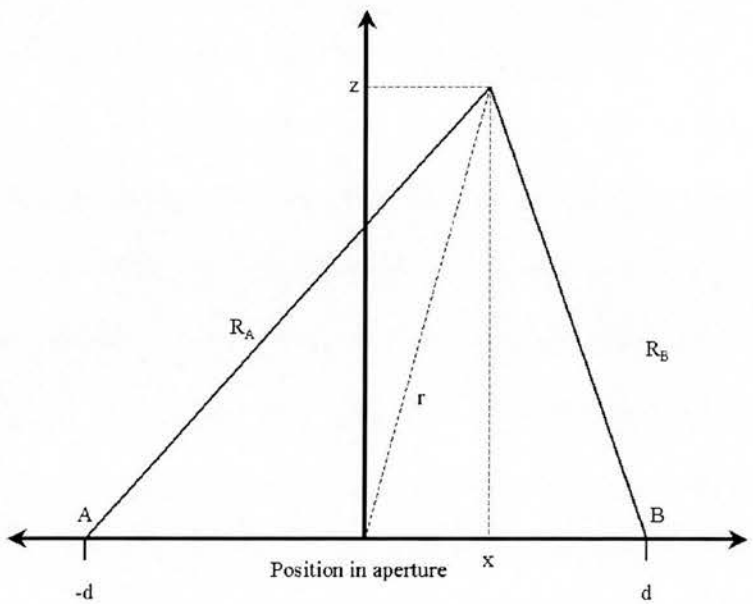

Figure 2-12: Two-element array geometry

The two signals received at A and B are the following:

$$s_A(t) = {}^{1}\!/_{R_A} \exp\left(-j\omega\left(t - \frac{R_A}{c}\right)\right) = {}^{1}\!/_{R_A} \exp(-j\omega t)\exp\left(j\omega\frac{R_A}{c}\right)$$
$$s_B(t) = {}^{1}\!/_{R_B} \exp\left(-j\omega\left(t - \frac{R_B}{c}\right)\right) = {}^{1}\!/_{R_B} \exp(-jwt)\exp\left(j\omega\frac{R_B}{c}\right) \quad (2\text{-}50)$$

Given the Fraunhofer approximation in the far field or focal plane, z>>x, ${}^{1}\!/_{R_A} \approx {}^{1}\!/_{R_B} \approx {}^{1}\!/_{r}$. Therefore we can drop this term in equations (2-50). After applying the even and odd apodizations we obtain the following signals:

$$\begin{aligned} Even(t) &= s_A(t) + s_B(t) \\ &= \exp(-j\omega t)\times\left[\exp\left(j\omega\frac{R_A}{c}\right) + \exp\left(j\omega\frac{R_B}{c}\right)\right] \\ Odd(t) &= -js_A(t) + js_B(t) \\ &= \exp(-j\omega t)\times\left[-j\exp\left(j\omega\frac{R_A}{c}\right) + j\exp\left(j\omega\frac{R_B}{c}\right)\right] \end{aligned} \quad (2\text{-}51)$$

If the Taylor development is applied as following:

$$\sqrt{1+b} = 1 + \frac{1}{2}b - \frac{1}{8}b^2 + \xi(b) \quad (2\text{-}52)$$

where $\xi(b) \xrightarrow{b\to 0} 0$.

Then it follows:

$$R_A = \sqrt{z^2 + (d_x + x)^2} \approx z\left(1 + \frac{1}{2}\left(\frac{d_x + x}{z}\right)^2\right)$$
$$R_B = \sqrt{z^2 + (d_x - x)^2} \approx z\left(1 + \frac{1}{2}\left(\frac{d_x - x}{z}\right)^2\right) \quad (2\text{-}53)$$

Equations (2-51) become:

$$Even(t) = \exp(-j\omega t) \times \left[\begin{array}{l} \exp\left(\frac{j\omega c}{z} \left(1 + \frac{1}{2} \left(\frac{d_x + x}{z} \right)^2 \right) \right) \\ + \exp\left(\frac{j\omega c}{z} \left(1 + \frac{1}{2} \left(\frac{d_x - x}{z} \right)^2 \right) \right) \end{array} \right]$$

$$Odd(t) = \exp(-j\omega t) \times \left[\begin{array}{l} -j \exp\left(\frac{j\omega c}{z} \left(1 + \frac{1}{2} \left(\frac{d_x + x}{z} \right)^2 \right) \right) \\ + j \exp\left(\frac{j\omega c}{z} \left(1 + \frac{1}{2} \left(\frac{d\ - x}{z} \right)^2 \right) \right) \end{array} \right] \qquad (2\text{-}54)$$

By expanding, factoring and using Euler's identities equations (9-5) can be written as follows:

$$Even(t) = \exp(-j\omega t) \times \exp\left(\frac{j\omega c}{z} \right) \times \exp\left(\frac{j\omega}{2zc} \left(x^2 + d_x^{\ 2} \right) \right) \times 2\cos\left(\frac{\omega d_x x}{zc} \right)$$

$$Odd(t) = \exp(-j\omega t) \times \exp\left(\frac{j\omega c}{z} \right) \times \exp\left(\frac{j\omega}{2zc} \left(x^2 + d_x^{\ 2} \right) \right) \times 2\sin\left(\frac{\omega d_x x}{zc} \right) \qquad (2\text{-}55)$$

The two equations in (2-55) are identical except for the real modulation factor, which are of the forms $\cos\left(2\pi k_{lat} x\right)$ and $\sin\left(2\pi k_{lat} x\right)$, where $k_{lat} = \omega d / 2\pi zc$. The term $\exp(-j\omega t)$ represents the carrier frequency. $\exp\left(\frac{j\omega z}{c} \right)$ represents the phase delay due to the propagation of the wave from the focal plane at distance z to the array. $\exp\left(\frac{j\omega}{2zc} \left(x^2 + d_x^{\ 2} \right) \right)$ is a frequency dependent quadratic phase term analogous to that in the Fraunhofer approximation.

2.8.4. Appendix D: Tranverse and Beam Velocity Components Calculation in the Spatial Quadrature case

For the regular Doppler technique (no transverse modulation), the complex received signal (after the Hilbert transform) sampled at the depth of interest for a narrow band pulse can be expressed as following:

$$r(i) = \exp\left(2\pi \frac{2v_z}{c} f_0 i T_{prf} + \phi \right) \tag{2-56}$$

where c is the sound velocity, v_z is the projection of the blood velocity on the beam axis, f_0 is the transmit frequency, i the pulse number, T_{prf} the time between two pulses emissions, and ϕ is an arbitrary phase factor.

In the case of odd and even modulated ultrasound fields, the even and odd receive signals can be written as:

$$r_{even}(i) = \exp\left(2\pi \frac{2v_z}{c} f_0 i T_{prf} \right) \cos\left(2\pi \frac{v_x}{d_x} i T_{prf} \right) \tag{2-57}$$

$$r_{odd}(i) = \exp\left(2\pi \frac{2v_z}{c} f_0 i T_{prf} \right) \sin\left(2\pi \frac{v_x}{d_x} i T_{prf} \right) \tag{2-58}$$

where v_x is the transverse velocity and d_x is the lateral modulation period.

Using Euler's equations and equations (2-57) and (2-58) we obtain:

$$\begin{aligned} r_1(i) &= r_{even}(i) + j r_{odd}(i) = \exp\left(j 2\pi i T_{prf} \left(f_x + f_p \right) \right) \\ r_2(i) &= r_{even}(i) - j r_{odd}(i) = \exp\left(j 2\pi i T_{prf} \left(f_x - f_p \right) \right) \end{aligned} \tag{2-59}$$

where $f_x = v_x/d_x$ and $f_p = 2v_z/cxf_0$.

By multiplying these two signals, two demodulated signals along the two spatial axes can deduced:

$$het_{lateral}(i) = r_1(i) \times r_2(i)^* = \exp\left(j2\pi i T_{prf} f_x\right)$$
$$het_{axial}(i) = r_1(i) \times r_2(i) = \exp\left(j2\pi i T_{prf} f_p\right) \quad (2\text{-}60)$$

The two phases of the signals are given by:

$$d\theta_{lateral} = 2\pi 2T_{prf} f_x = 4\pi T_{prf} \frac{v_x}{d_x}$$
$$d\theta_{axial} = 2\pi 2T_{prf} f_p = 4\pi T_{prf} \frac{2v_z}{c} f_0 \quad (2\text{-}61)$$

and therefore v_x and v_z can be calculated:

$$v_x = \frac{d\theta_{lateral} d_x}{2\pi 2T_{prf}}$$
$$v_z = \frac{d\theta_{axial} c}{2\pi 4T_{prf} f_0} \quad (2\text{-}62)$$

Using the lag one autocorrelation gives an estimate of the phase shift:

$$d\theta = \arctan\left(\frac{\mathrm{Im}\left(R(1)\right)}{\mathrm{Re}\left(R(1)\right)}\right) \quad (2\text{-}63)$$

where Im(R(1)) represents the imaginary part of the complex lag one autocorrelation and Re(R(1)) the real part.

If we consider the following geometrical equivalence:

$$\tan(A+B) = \frac{\tan(A)+\tan(B)}{1-\tan(A)\tan(B)} \quad (2\text{-}64)$$

It follows:

$$v_x = \frac{d_x}{2\pi 2T_{prf}} \arctan\left(\frac{\mathrm{Im}\left(R_1(1)\right)\mathrm{Re}\left(R_2(1)\right)+\mathrm{Im}\left(R_2(1)\right)\mathrm{Re}\left(R_1(1)\right)}{\mathrm{Re}\left(R_1(1)\right)\mathrm{Re}\left(R_2(1)\right)-\mathrm{Im}\left(R_1(1)\right)\mathrm{Im}\left(R_2(1)\right)}\right)$$
$$v_z = \frac{c}{2\pi 4T_{prf} f_0} \arctan\left(\frac{\mathrm{Im}\left(R_1(1)\right)\mathrm{Re}\left(R_2(1)\right)-\mathrm{Im}\left(R_2(1)\right)\mathrm{Re}\left(R_1(1)\right)}{\mathrm{Re}\left(R_1(1)\right)\mathrm{Re}\left(R_2(1)\right)+\mathrm{Im}\left(R_1(1)\right)\mathrm{Im}\left(R_2(1)\right)}\right) \quad (2\text{-}65)$$

where $R_k(s)$ represents the autocorrelation function of lag s (integer) of r_k and is expressed as:

$$R_k(s) = \sum_{i=0}^{i=N-s} r_k(i) \times r_k(i+s)^* \quad (2\text{-}66)$$

where N is the total number of pulses sent to form a line.

The magnitude and angle of the velocity can be found from v_z and v_x.

$$v = \sqrt{\left(v_z^2 + v_x^2\right)} \quad (2\text{-}67)$$

$$\theta = a\tan\left(\frac{v_x}{v_z}\right) \quad (2\text{-}68)$$

2.8.5. Appendix E: Tranverse and Beam Velocity Components Calculation for the Vector Velocity Technique

For the regular Doppler technique (no spatial quadrature), the received signal sampled at the depth of interest for a narrow band pulse can be expressed as following:

$$r(i) = \cos\left(2\pi \frac{2v_z}{c} f_0 i T_{prf} + \phi\right) \quad (2\text{-}69)$$

where c is the sound velocity, v_z is the projection of the blood velocity on the beam axis, f_0 is the transmit frequency, i the pulse number, T_{prf} the time between two pulses emissions, and ϕ is an arbitrary phase factor.

If we then generate the spatial quadrature fields, the receive signal can be written as:

$$r_{sq}(i) = \cos\left(2\pi \frac{2v_z}{c} f_0 i T_{prf}\right) \exp\left(2\pi \frac{v_x}{d_x} i T_{prf}\right) \quad (2\text{-}70)$$

where v_x is the transverse velocity and d_x is the lateral modulation period.

If we perform the Hilbert transform of r(i) we obtain:

$$r_{sqh}(i) = \sin\left(2\pi \frac{2v_z}{c} f_0 i T_{prf}\right) \exp\left(2\pi \frac{v_x}{d_x} i T_{prf}\right) \tag{2-71}$$

Using Euler's equations and equations (2-70) and (2-71) we obtain:

$$\begin{aligned} r_1(i) &= r_{sq}(i) + j r_{sqh}(i) = \exp\left(j2\pi i T_{prf}\left(f_x + f_p\right)\right) \\ r_2(i) &= r_{sq}(i) - j r_{sqh}(i) = \exp\left(j2\pi i T_{prf}\left(f_x - f_p\right)\right) \end{aligned} \tag{2-72}$$

where $f_x = v_x/d_x$ and $f_p = 2v_z/c*f_0$.

The two phases of the signals are given by:

$$\begin{aligned} d\theta_1 &= 2\pi T_{prf}\left(f_x + f_p\right) \\ d\theta_2 &= 2\pi T_{prf}\left(f_x - f_p\right) \end{aligned} \tag{2-73}$$

Adding and subtracting the two phase changes give:

$$\begin{aligned} d\theta_1 + d\theta_2 &= 2\pi 2 T_{prf} f_x = 4\pi T_{prf} \frac{v_x}{d_x} \\ d\theta_1 - d\theta_2 &= 2\pi 2 T_{prf} f_p = 4\pi T_{prf} \frac{2v_z}{c} f_0 \end{aligned} \tag{2-74}$$

and therefore we deduce v_x and v_z :

$$\begin{aligned} v_x &= \frac{\left(d\theta_1 + d\theta_2\right) d_x}{2\pi 2 T_{prf}} \\ v_z &= \frac{\left(d\theta_1 - d\theta_2\right) c}{2\pi 4 T_{prf} f_0} \end{aligned} \tag{2-74}$$

The velocity and the angle can then be calculated as in the appendix D using equations (2-66)-(2-68).

3. Real Time Pulsed Wave Vector Doppler

3.1. Introduction

To fully understand the multi-beam technique a real time two- component velocity pulse wave Doppler system has first been developed. This system is used to validate the multi-beam technique in one dimension (using only one spatial gate rather than having multiple gates in two-dimension imaging). This chapter describes the implementation of such a system and the experimental validation and results.

3.2. Multi-component Doppler Technique

Multi-component Doppler techniques make use of multiple transducers to perform Doppler measurements along different line of sight, over the same investigated volume (called sample volume). In this chapter the design of a new system to perform two-component Doppler measurements is presented.

Different single array aperture configurations can be used to perform simultaneous two-component Doppler:

- Phillips et al. (Phillips, Kadi et al. 1995) used a configuration where a conventional ultrasound pulse is transmitted from one of the sub-apertures and then both sub-apertures are simultaneously used for reception. The receive only sub-aperture must track echoes along the direction of the acoustic burst transmitted from transmit-receive sub-aperture at the same time that echoes are received by the transmit receive sub-aperture. To span the two dimensional space, the transmit-receive sub-aperture has to scan in a conventional phased-array format, while the receive only sub-aperture receives angular-scattered echoes by tracking the transmitted beamformed by transmit receive sub-aperture.

- Scabia et al.(Scabia, Calzolai et al. 2000) used another configuration where a linear array is divided into two sub-apertures and the transmit aperture is localized at the centre of both receive sub-apertures (c.f. **figure 3-3**). In this configuration conventional dynamic receive beamformation is used in reception.

In Phillips et al (Phillips, Kadi et al. 1995) configuration, the tracking makes the beamformation for the receive only sub-aperture more complex than Scabia et al. (Scabia, Calzolai et al. 2000) configuration, where no tracking is required and conventional geometrical beamformation can be used for both receive sub-apertures is used. The two-way or "round trip" (transmit and receive) beam separation in Phillips configuration is also equivalent to Scabia et al. (Scabia, Calzolai et al. 2000) configuration (if the same receive aperture sizes and locations are used). We chose to implement Scabia et al. (Scabia, Calzolai et al. 2000) configuration because of the simpler receive beamformation and equivalent beam separation.

This prototype is based on a commercially available ultrasound, the HDI 5000 (Philips Ultrasound, WA, USA). A 128-element linear array transducer (L7-4, Philips Ultrasound) with electronic focusing and beam steering is used. This conventional linear array transducer is electronically subdivided into two receive sub-apertures (software modified by the author), which are spatially separated (c.f. **figure 3-1**). A beamformer is used to steer and focus the ultrasound beams simultaneously for each aperture. A conventional pulse is transmitted from the transmit aperture and then both receive sub-apertures are used for reception. Two scanning methods, non-steered and steered are possible and shown in **figures 3-1** and **3-2** respectively.

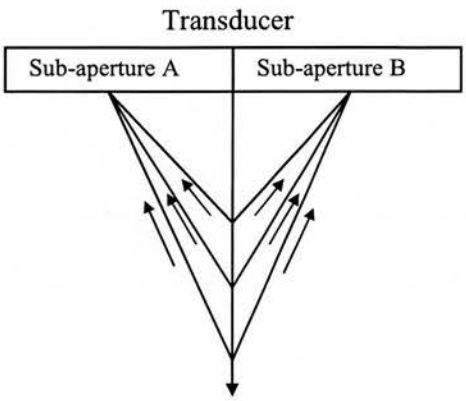

Figure 3-1: Scanning configuration with no steering angle

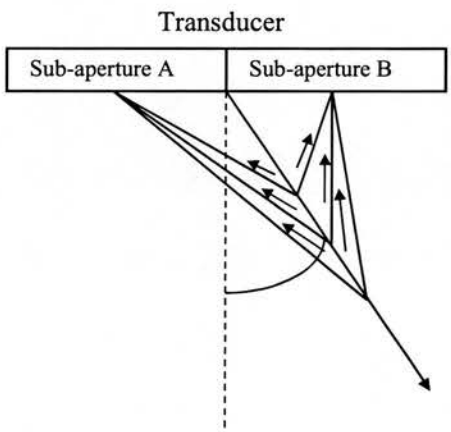

Figure 3-2: Scanning configuration with steering angle

The centers of two receive aperture are located at a distance D from the transmit aperture, corresponding to 12-degree steering angle (in non steered configuration, $\theta_{MeanFRA} = \theta_{MeanFRB} = 12\,\mathrm{deg}$, c.f. **figure 3-3**).

The independent sub-apertures receive the reflected pulses and the returned signals are processed for Doppler information in the conventional way.

Two mean frequency Doppler shifts are measured from the receive apertures. Using the Doppler equation and the known geometry (**figure 3-3**) of the transmit and receive beams, it is then possible to calculate the magnitude of the two component vector velocity $|\bar{v}|$ and its direction θ_v relative to the coordinate system indicated. As shown in **figure 3-3**, all angles are defined as counterclockwise and positive from the reference indicated.

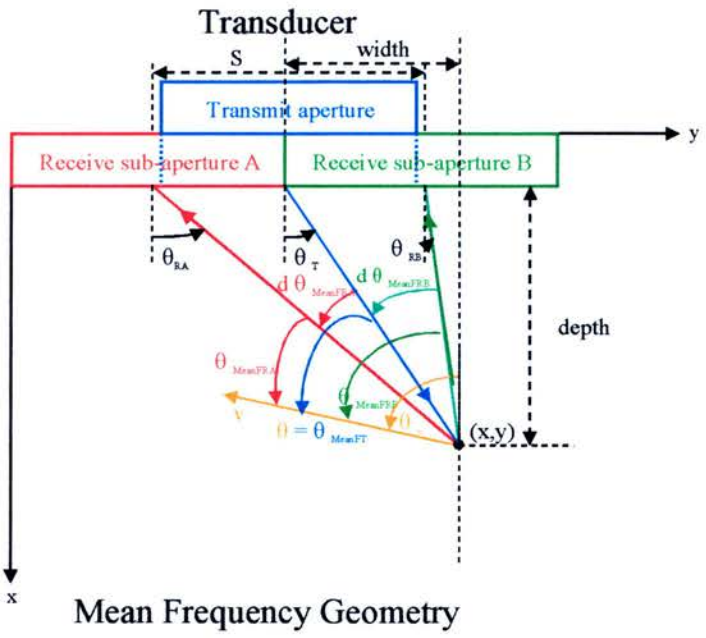

Figure 3-3: Array geometry adopted for multiple beam reception using mean frequencies. Angles are defined counterclockwise and positive from the reference shown

For the angular-scatter the mean frequency $\overline{f_{MeanA}}$ and $\overline{f_{MeanB}}$ can be measured using the following equations (3-1 to 3-7):

$$\begin{aligned}\overline{f_{MeanA}} &= \frac{|\bar{v}|*\left[\cos(\theta_{MeanFRA})+\cos(\theta)\right]*f_0}{c} \\ \overline{f_{MeanB}} &= \frac{|\bar{v}|*\left[\cos(\theta_{MeanFRB})+\cos(\theta)\right]*f_0}{c}\end{aligned} \quad (3\text{-}1)$$

where $\theta_{MeanFRA}$ and $\theta_{MeanFRB}$ are derived from the following equations:

$$\begin{aligned}\theta_{MeanFRA} &= \theta_v - \theta_{RA} \\ \theta_{MeanFRB} &= \theta_v - \theta_{RB}\end{aligned} \quad (3\text{-}2)$$

$$\begin{aligned}\theta &= \theta_v - \theta_T \\ \theta_T &= steeringangle\end{aligned} \quad (3\text{-}3)$$

$$v = \frac{f_{MeanB} \times c}{f_0 \times (\cos(\theta_v - \theta_{RB}) + \cos(\theta_v - \theta_T)}$$

$$\frac{S}{2} = R \times \tan(accep\tan ceangle) \tag{3-4}$$

$$width = R \times \sin(\theta_T)$$

$$depth = R \times \cos(\theta_T)$$

$$\begin{aligned} d\theta_{MeanFRA} &= \theta_{RA} - \theta_T \\ d\theta_{MeanFRB} &= \theta_T - \theta_{RB} \end{aligned} \tag{3-5}$$

$$\begin{aligned} \theta_{RA} &= \tan^{-1}\left[\frac{|width| + |S|/2}{|depth|}\right] \\ \theta_{RB} &= \theta_T - \tan^{-1}\left[\frac{|width| - |S|/2}{|depth|}\right] \end{aligned} \tag{3-6}$$

$$\theta_v = \tan^{-1}\left[\frac{f_{MeanA} * \left(\cos\left(d\theta_{MeanFRB}\right) + 1\right) - f_{MeanB} * \left(\cos\left(d\theta_{MeanFRA}\right) + 1\right)}{f_{MeanA} * \sin\left(d\theta_{MeanFRB}\right) + f_{MeanB} * \sin\left(d\theta_{MeanFRA}\right)}\right] + \theta_T \tag{3-7}$$

In our case $\theta_{MeanFRA} = \theta_{MeanFRB} = \theta_{Mean}$.

The two-component vector Doppler system calculates the mean frequency Doppler shifts, $\overline{f_{MeanB}}$ and $\overline{f_{MeanA}}$, as centroids of the fast Fourier transforms (FFT) of the demodulated Doppler signals from the two receive sub-apertures. Centroids are calculated by applying a mean weighted function on the Doppler spectra. The weight is calculated as the normalized distance from the peak power frequency bin to the actual frequency bin.

As in single beam PW Doppler systems, a maximum depth of investigation X_{Max} can be defined as a function of pulse repetition frequency (PRF); in the two-component Doppler case with the above assumptions for the scanning geometry, the round trip distance is $X_{Max}\left(1 + \cos\left(\theta_{Mean}\right)\right)$ and therefore, X_{Max} depends on θ_{Mean} according to the following relationship:

$$X_{Max} = (c/PRF)\left(\cos(\theta_{Mean})(1+\cos(\theta_{Mean}))\right) \qquad (3\text{-}8)$$

Equation 3-8, when $\theta_{Mean} = 0$, reduces to the well-known results for the single beam Doppler, which is $X_{Max} = c/(2 \times PRF)$.

Another important issue, in Doppler systems, is the aliasing problem. In the case of the two-component Doppler system, the maximum detectable velocity depends on the PRF and the angle between the probe axis and the velocity vector, but with a different law than the mono-component Doppler case. The maximum Doppler velocity is different for the two receivers, because they receive the scattered signal from the same sample volume with different angles. The relationships reported in the following equations determine the maximum velocity magnitude detectable by receivers A and B as a function of PRF and the angle θ_{Mean} :

$$V_{MaxA} = \frac{c}{f_0} \times \left| \frac{PRF}{2(\alpha - 1)} \right| \times \sqrt{\frac{1}{\sin^2 \theta_{Mean}} + \frac{\alpha^2}{(1+\cos(\theta_{Mean}))^2}} \qquad (3\text{-}9)$$

$$V_{MaxB} = \frac{c}{f_0} \times \left| \frac{PRF}{2(\alpha + 1)} \right| \times \sqrt{\frac{1}{\sin^2 \theta_{Mean}} + \frac{\alpha^2}{(1+\cos(\theta_{Mean}))^2}} \qquad (3\text{-}10)$$

where $\alpha = \tan(\theta) \times (1+\cos(\theta_{Mean}))/\sin(\theta_{Mean})$.

These relationships are derived considering that the maximum detectable Doppler frequency by each transducer is $PRF/2$, and taking into account the geometry of the probe. Finally, the overall maximum velocity V_{Max} detectable is chosen as the minimum of the two maximum velocities expressed in equations (3-9) and (3-10):

$$V_{Max} = \min(V_{Max1}, V_{Max2}) \qquad (3\text{-}11)$$

The two-component Doppler system is capable of scanning two-dimensional areas (the sample volume can be moved laterally and axially). The technique used for

lateral movement of the sample volume is done by moving the group of transmit/receive (RXA/TX/RXB) sub-apertures along the array (c.f. **figure 3-4**), keeping constant the distance between the transmit (TX) and receive sub-apertures (RXA and RXB).

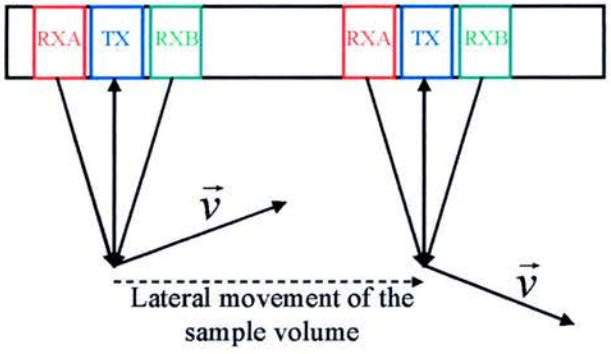

Figure 3-4: Example of lateral movement of the sample volume. The lateral movement of the sample volume is achieved by moving the RXA/TX/RXB sub-aperture group. The distances between the centers of the sub-apertures remain constant for a fixed scan depth.

For the axial movement of the sample volume the transmit sub-aperture (TX) is kept on the same position on the array, and the centers of the two receive sub-apertures (RXA and RXB) are moved symmetrically in opposite directions, with constant steering angle (or acceptance angle). As the sample volume moves deeper the centers of two receive sub-apertures move away from each other and the apertures increase their sizes to maintain a constant F-number (depth over the width of the sub-aperture is constant F=depth/width of the sub-aperture). The inverse is true when the sample volume is moved close to the skin line. The F-number is maintained constant to have

the same separation between the receive beams. Therefore the spectral broadening is constant and the precision of two components of the velocity does not vary with depth (until the limits of the array are reached).

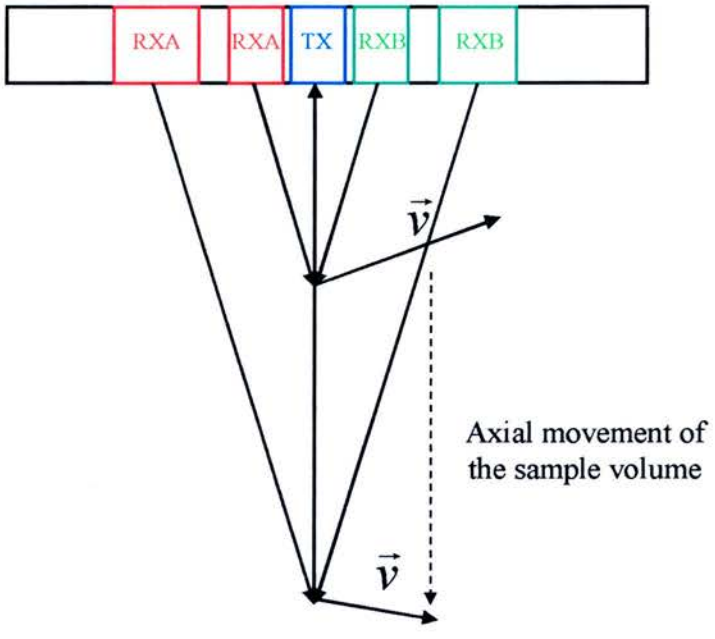

Figure 3-5: Example of axial movement of the sample volume. The axial movement of the sample volume is achieved by moving in opposite direction the receive sub-apertures RXA/RXB.

The same technique will be applied for two-dimensional vector Doppler in the following chapter.

3.3. System Design and Data Acquisition and Processing

The implementation of vector Doppler has been performed by modifying the hardware and software of a commercial ultrasound diagnostic imaging system, the HDI 5000 (Philips Ultrasound, Bothell, WA, USA). The modifications, done by the author, consist of enabling the beamformer to simultaneously acquire two beams from the two receive sub-apertures. The per element Radio Frequency (RF) signals are digitized with a 10-bit A/D converter and the RF data are then focused, steered

along the two directions θ_{Mean} and $-\theta_{Mean}$, respectively for sub-apertures RXA and RXB, and summed to form two 18-bit summed RF signals. The signal path has been modified by the author to process simultaneously these two signals. The two summed RF signals are first quadrature band-pass filtered to extract an in phase and a quadrature (IQ) samples at the sample volume depth. The FFT of the two IQ pairs is then calculated at 1 KHz to create two spectrograms. The spectrograms are compressed to 8-bit data and then displayed simultaneously on the screen of the ultrasound system. An example of the display is shown in **figure 3-6**. Two types of data can be acquired along the signal path of the two-component Doppler system:

- Two seconds of 18-bit summed RF data can be acquired at 24 MHz sampling (c.f. appendix 3.8) or

- 8-bit spectrograms can be acquired with almost unlimited time (c.f. appendix 3.8).

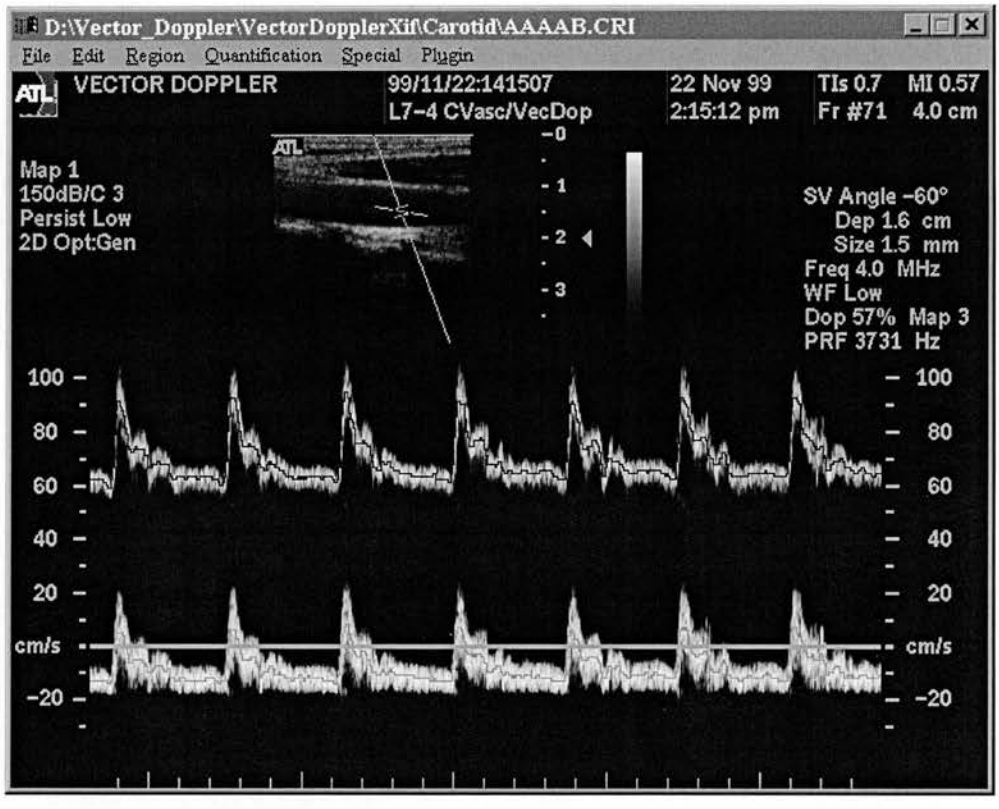

Figure 3-6: Example of the display of the two spectrograms coming from the two separate receive apertures. The sample volume is in a carotid artery.

The signal path is illustrated in **figure 3-7**. The 8-bit spectrograms are sent from the image memory of the HDI 5000 directly to a PC workstation where they are processed using HDI Lab, an offline quantification package developed by Philips Ultrasound to support research. The spectrograms as well as some acquisition and display information data are sent to HDI Lab. A C++ HDI Lab plugin was developed by the author to extract the mean frequencies of the two spectrograms and to calculate and display the true velocity and angle of the target. The maximum frequency can also be used to estimate the true velocity and angle but in the

following chapters where this technique is extended to two dimensions, the autocorrelation approach is used and can only generate the mean velocity.

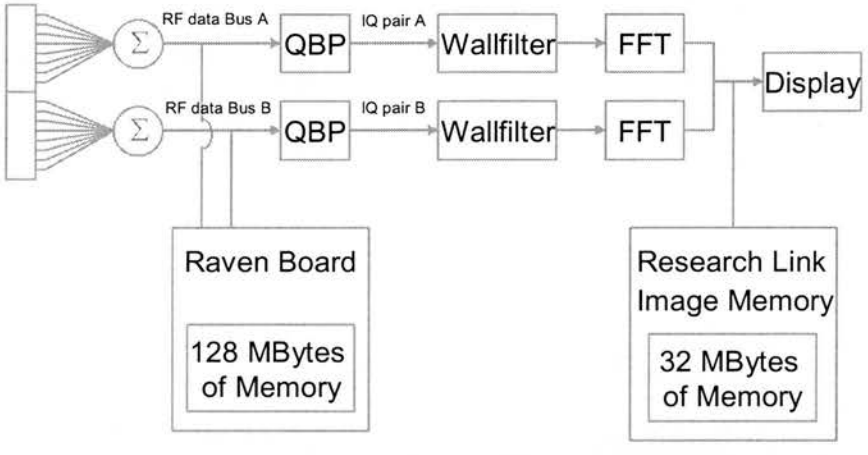

Figure 3-7: Data Acquisition and processing for the real time two component PW Doppler.

Transmit characteristics:

A conventional ultrasound pulse is transmitted from the whole transmit aperture using no apodization and focusing as close as possible to the sample volume. The number of cycles in the transmit pulse matches the sample volume and is sinusoidally apodized.

Receive characteristics:

There is no receive apodization and the focusing is as close as possible to the sample volume. The acceptance angle is fixed for each application (transducer selection).

The receive aperture is calculated from the acceptance angle in non-steering and applied to steered and non-steered apertures.

There is no apodization in receive and in transmit to maximize the Doppler signal sent and received and therefore to maximize sensitivity.

3.4. Experimental Validation

Different experiments are performed on a laboratory test object to produce spectrograms in real time to validate the technique. The test object is used to verify the system capability to measure velocity of moving targets. A BBS string phantom (BBS Medical Electronic, Sweden), using a 1.6 mm diameter "O"-ring rubber loop, is used for this validation. The free ends of the "O"-ring were joined flush in order to prevent the generation of a transient spike on the spectral display as the join pass through the sample volume. The filament was immersed in a 9.5 % glycerol solution whose speed of sound was 1540 m/s. The containing tank was lined across its base with acoustic absorber (Ceram AB, Lund, Sweden) to reduce reflections. In all experiments the indicated string velocity is 1 m/s and the true string velocity (mean, standard deviation) was 106 ± 0.4 cm/s. The real filament speed is different from the indicated speed due to the fact that the "O"-ring has a diameter of 1.6 mm, hence sits further out the radius where the speed is higher. For more details on the string phantom, a full description of the preparation and calibration of the string phantom is given in by Hoskins (Hoskins 1996).

Spectrograms are collected for calibrated angles ranging from 27 to 83 degrees (every two degrees), and depth ranging from (15 mm to 81 mm). An example of spectrograms obtained from the ultrasound system is illustrated **figure 3-8**.

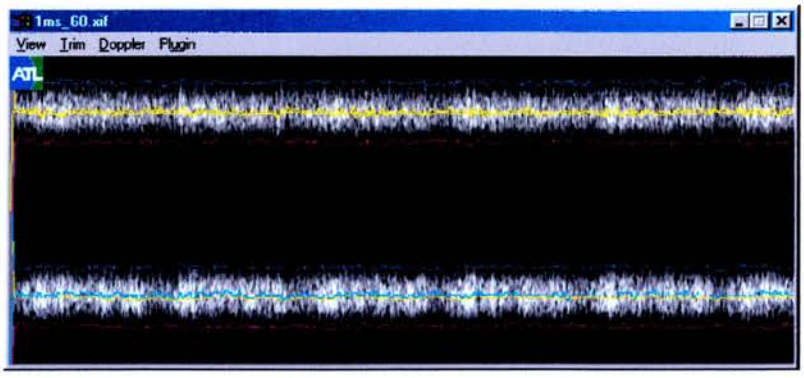

Figure 3-8: String phantom spectrograms displayed with HDI Lab. Mean Frequencies are represented in yellow.

3.5. Results

3.5.1. Angle Calibration

Figure 3-9 illustrates the angle calibration results. From 27 to 83 degrees (beam to string angle) spectrograms are collected and analyzed. The beam-string angle and the true velocity are calculated for each of these beam/string angles. The mean angle error for all angles is 0.07 degree with a standard deviation over all measured angle of 1.5 degree and the mean standard deviation is 0.24 degree.

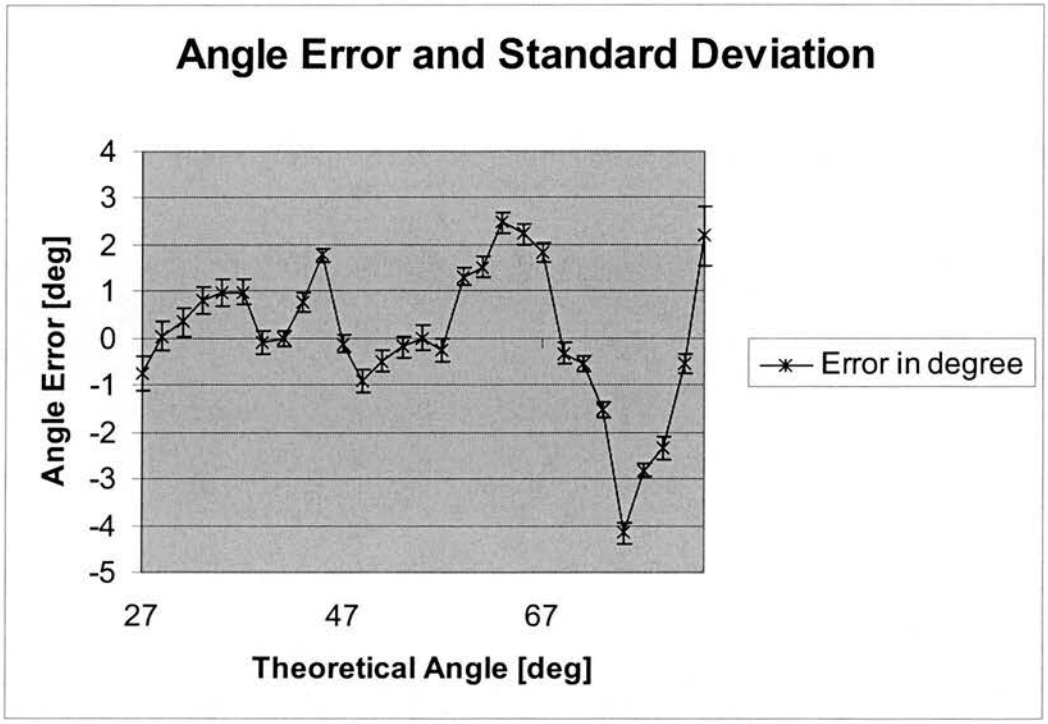

Figure 3-9: Angle Error and standard deviation for the string phantom calibration in percent.

Figure 3-10 represents the results for the velocity measurements. The mean velocity error in percent is displayed as a function of transmit beam/string angle. The mean error is 2.02 % with a standard deviation of 11.41 % and a mean standard deviation of 0.49 %.

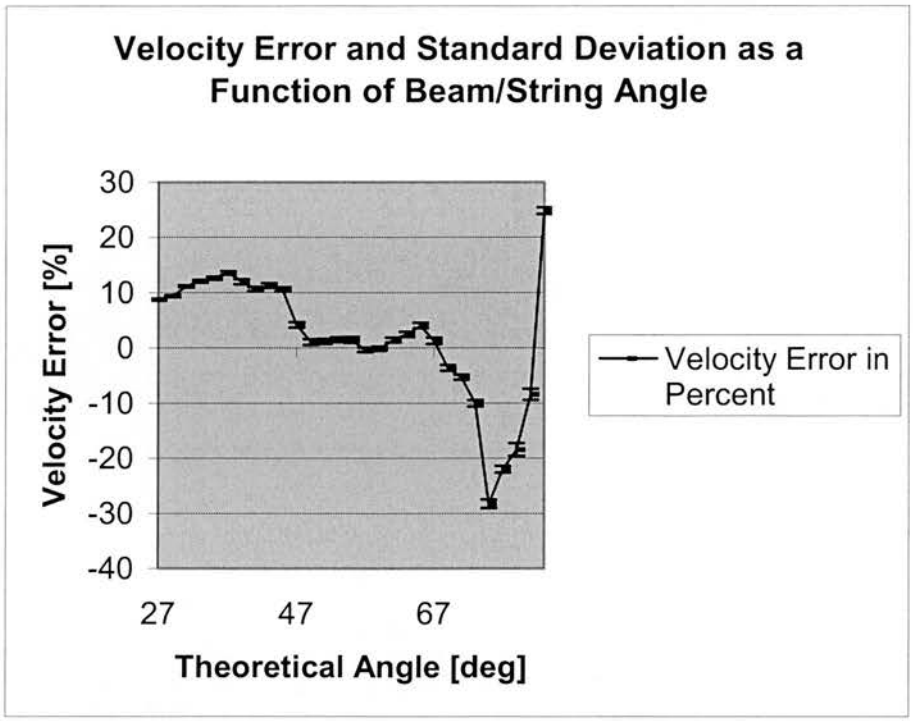

Figure 3-10: Mean velocity error and standard deviation as a function of transmit beam/string in percent.

The velocity error graphs shows that the true velocity can be measured with an error below 5 % with the two-component Doppler device for transmit beam/string angle between 47 and 69 degree. Above 67 degrees the velocity error can be significant (around 20 %) and below 47 degree the error is around 10 %. For all angles the calculated velocity standard deviation is very small (below 1%). The velocity bias above 67 degrees is due to the fact that the mean velocity of one of the receive sub-apertures is biased by the high pass filter. This effect is illustrated in **figure 3-11**. In that setting the transmit beam/string angle is 72 degrees which means that the receive beam of one of the sub-apertures is 84 degrees and almost perpendicular to the string. The bottom spectrum corresponds to this sub-aperture and is partially filtered out by the high pass filter. The bottom mean velocity is therefore overestimated, which biases the absolute velocity estimation. The negative swing after 67 degrees is due to

the fact that the beam/string angle of one of the sub-apertures crosses through the 90 degree angle. The highest negative angle is when the beam/string angle of this sub-aperture is equal to 90 degrees.

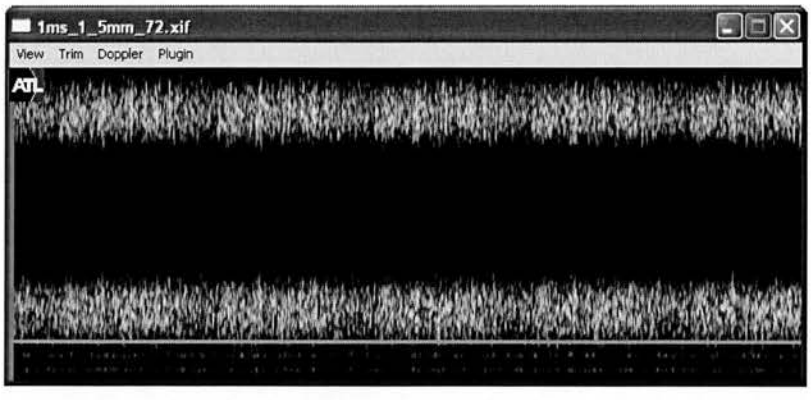

Figure 3-11: String phantom spectrograms displayed with HDI Lab for a transmit beam/string angle of 72 degrees. The bottom spectrum is obtained from the received sub-aperture, which receive beam makes an angle close to 90 degrees with the string phantom.

For angles below 47 degrees the signal received from the sub-aperture, which has the receive beam/string angle the closest to zero degree, is weaker than the signal received from the other sub-aperture. This effect is related to the directivity effect of the transducer elements. As the angle of incidence to the transducer elements becomes smaller (gets closer to zero degree), the amplitude of received signal decreases. This effect is illustrated **figure 3-12** where the top and the bottom Doppler spectra have different amplitudes. This decrease of signal will increase the bias of the velocity. It is also more difficult as the string becomes more parallel to the transmit beam to make sure that the sample volume is centered on the string. In the dual beam case where there are two receive sample volumes, if one overlaps more with the string that the other the velocity measurements will be biased (Steel, Ramnarine et al.

2003). The angle error is fairly small for all angles (below 4 degrees) and the standard deviation is around 1 degree.

Figure 3-12: String phantom spectrograms displayed with HDI Lab for a transmit beam/string angle of 32 degrees. The top spectrum has lower amplitude than the bottom spectrum due to the receive beam/string angle difference.

3.5.2. Depth Dependence

Figure 3-13 illustrates the transmit beam/string angle calculation dependence against depth. The angle does not vary as a function of depth (standard deviation of the error is 0.75 degrees with a mean error of 0.02 degree).

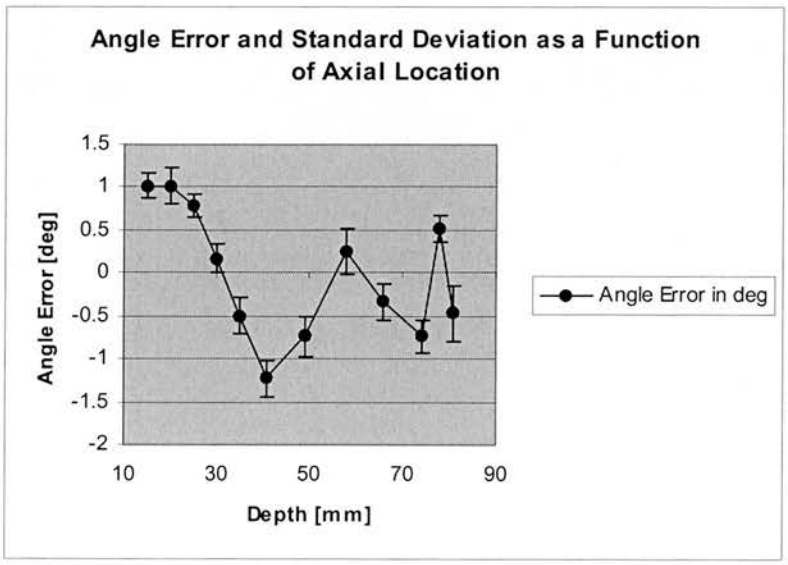

Figure 3-13: Mean angle error and standard deviation as a function of depth in degree.

Figure 3-14 illustrates the true velocity dependence against depth. The graph shows that the velocity does not vary as a function of depth (standard deviation of the error is 2.70 % with a mean error of 1.9 % degree).

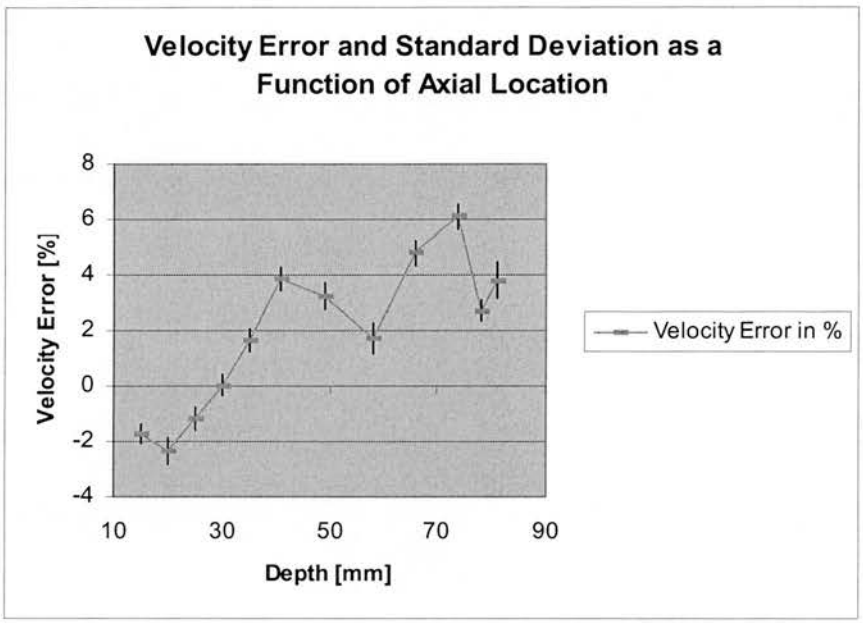

Figure 3-14: Mean velocity error and standard deviation as a function of depth in percent.

3.6. Clinical Validation

This technique was validated clinically by Steel et al. (Steel, Ramnarine et al. 2003; Steel, Ramnarine et al. 2004) for flow peak velocity measurements in the common carotid artery in 9-healthy volunteers. The goal of the study was to show that the dual beam vector Doppler ultrasound is angle independent and more reproducible than single beam Doppler system. The authors assessed the angle-dependence over Doppler angles of 40 degrees -70 degrees and the reproducibility of the dual-beam blood maximum velocity estimate measured in the common carotid arteries (CCA) 1 to 2 cm prior to the bifurcation of 9 presumed-healthy volunteers. The velocity magnitude estimate was reduced by approximately 7.9% as the angle between the

transmit beam and the vessel axis was increased from 40 degrees to 70 degrees. With repeat measurements made, on average, approximately 6 weeks apart, the 95% velocity magnitude limits of agreement were as follows: Intra-observer -41.3 to +45.2 cm/s; inter-observer -29.6 to +46.8 cm/s. There was an 8.6 cm/s inter-observer bias in velocity magnitude. The authors concluded that the dual-beam vector Doppler system can measure blood velocity within its scan plane with low dependence on angle and with similar reproducibility to that of single-beam systems.

Figure 3-15 shows the two spectrograms collected from a normal volunteer carotid and **figure 3-16** shows the calculated transmit beam/flow angle (mean 65 degree).

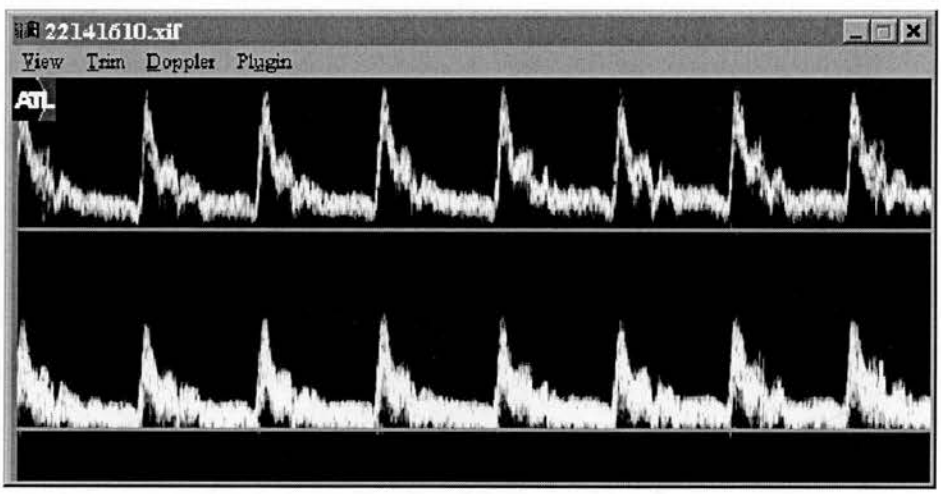

Figure 3-15: Spectrograms from a normal volunteer carotid flow.

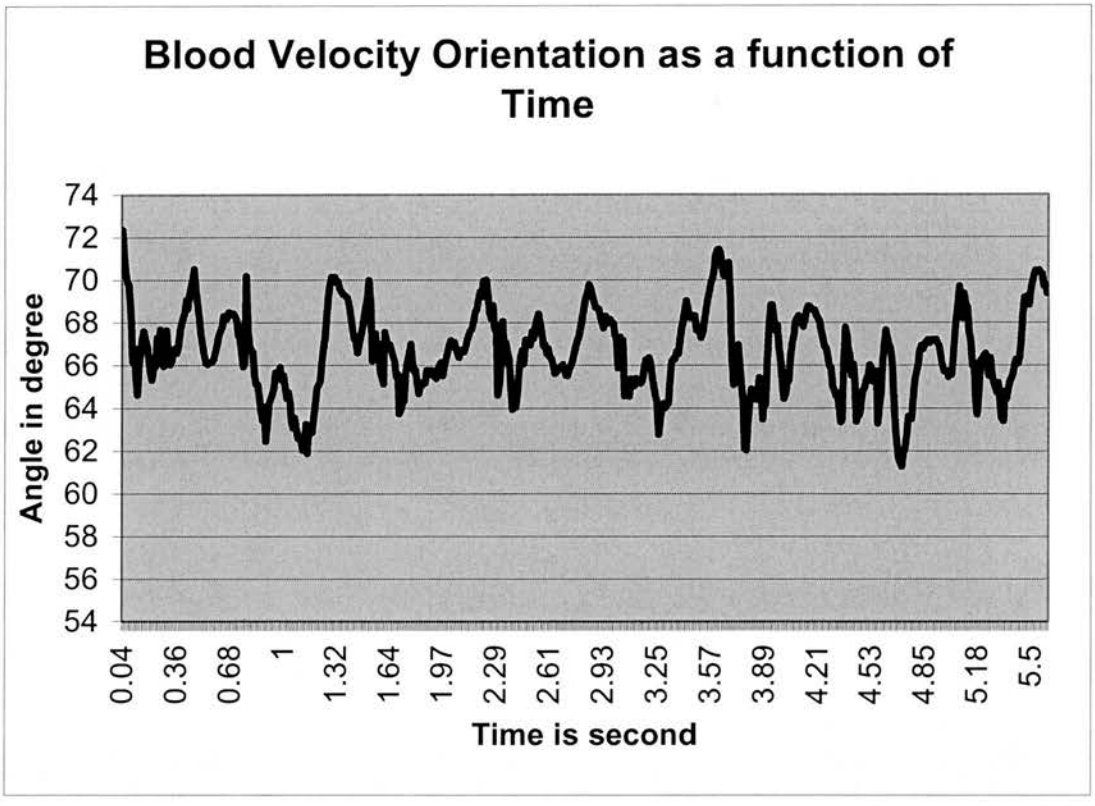

Figure 3-16: Calculated beam/flow angle in the carotid of a volunteer as a function of time.

3.7. Conclusion

A two-component velocity Doppler real time system has been implemented. The system is based on a commercial ultrasound system provided a 5-MHz 128-element linear-array transducer. The developed system is capable of displaying in real time the spectrograms from the two receive aperture and can calculate in real time the mean frequencies, the true beam/target velocity angle and magnitude for angle between 45 and 67 % with a velocity error below 5% and an angle error below 4 degree and with no depth dependence. This method has been validated for carotid flow application. In the next chapter this technique is extended to two dimensions and to tissue motion application.

3.8. Appendices

3.8.1. Raven RF acquisition system

Raven is an acquisition system that has been developed by Phillips Ultrasound to acquire and store beamformed and summed 18-bit RF data from a HDI 5000 ultrasound system (Philips Ultrasound, Inc., Bothell, WA, USA). Frames of RF data can be acquired and saved to removable media (e.g. Magneto Optical Disks) for later analysis. The system settings are simultaneously saved so that the RF data can be effectively analyzed. The Raven system comprises an embedded hardware module, a user control, a hard disk for buffering the acquired data and where the software driving the board resides and a Magneto Optical disk for exporting data.

The RF acquisition system comprises:

- An embedded raven board with 64 or 128 Mbytes of memory (RAM).
- A separate hard drive where the raven software resides and where the RF data are stored after acquisition.
- A MO drive where the data stored in the hard drive is spooled to.

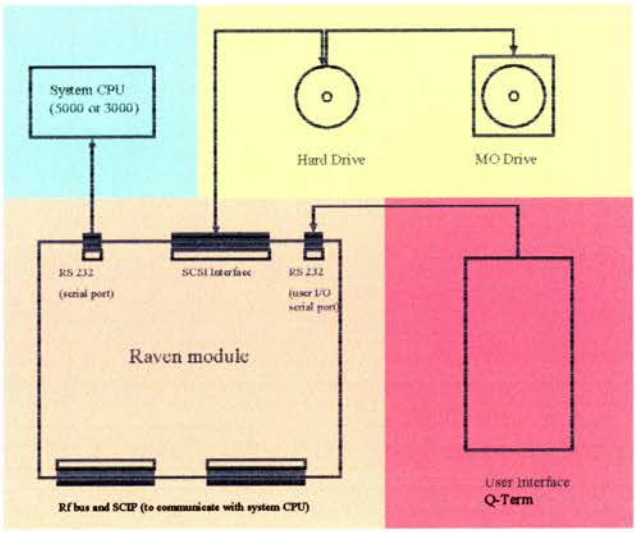

Figure 3-17: Raven Acquisition System.

Functions of each modules:

- The raven board (orange) acquires the RF data in real time. It has a cycling buffer so that as long as the system scans it is acquiring data cyclically. It can store up to 128 Mbytes. The Raven board boots from the external hard drive via a SCSI (Small Computer System Interface) link. The system has to be on freeze when collecting RF data.
- The user interface (pink) consists of an alphanumeric display incorporated into the handheld module. This supports interrogative dialogs and feedback to the user. Input commands to the raven board are generated from the handheld module, with each key having a pre-assigned character string saved in non-volatile memory (EPROM).

- The external hard drive (yellow) is a 2 gigabytes hard drive and contains the software to run the raven board. The external MO drive can write onto MO disks of up to 640 Mbytes. The MO drive is linked to the hard drive via a SCSI link.
- The Raven board is linked to the CPU (Central Processing Unit in green) of the ultrasound system via a serial link. This allows the Raven to send message to the ultrasound system CPU (e.g. command to print the parameter file).

3.8.2. Research Link

Research Link is a software package developed for the HDI 5000 (Philips Ultrasound, Inc., Bothell, WA, USA) to collect CFI, TDI, echo loops and Doppler spectrograms directly from the image memory of the ultrasound system (8-bit per sample data up to 64 Mbytes of data). Once collected, this data can be shipped directly to an offline PC (if the ultrasound system is linked to the offline PC via an Ethernet link). Then the data collected from the ultrasound system can be displayed and processed by HDI Lab, an offline quantification package developed by Philips Ultrasound, Inc. for researcher. Researchers can also develop their own HDILab plug-in to perform quantification or measurement. A plug-in is an algorithm or a simple routine that the researcher can add and run from HDI Lab. It extends the features of the software and allows the user to modify it in function of his needs.

4. Real Time Vector Doppler for Two-Dimensional Tissue Motion Imaging

4.1. Introduction

Tissue Doppler Imaging (TDI) (McDicken, Sutherland et al. 1992) can assess tissue motion in vascular and cardiac imaging. However, a major drawback of these measurements is that the motion estimation is limited to the component along the ultrasound beam axis. Cardiac and vessel wall motion studies have shown that complex three-component motions can be observed, and that there is a clinical need to fully assess the three components of the vector motion (Taratorin and Sideman 1995; Henson, Song et al. 2000; O'Dell, McCulloch et al. 2000).

In cardiology, the assessment of the left ventricle pumping patterns is of particular interest. The outer cardiac silhouette changes very little during the cardiac cycle (Hamilton and Rompf 1932; Hoffman and Ritman 1985), and the major changes occur intracardially as a result of the movement of the atrioventricular plane (plane between the ventricles and the atria) (Alam 1991; Alam, Rosenhamer et al. 1992). The observation that the epicardial site of the apex remains virtually immobile during the cardiac cycle has probably contributed to this notion (Slager, Hooghoudt et al. 1986; Assmann, Slager et al. 1988). This way of pumping the blood without much displacement of the intrathoracic structures surrounding the heart minimize the heart's energy expenditure during the cardiac cycle (Hamilton and Rompf 1932). This piston-like motion of the heart is correlated with the myocardial fiber directions. The myocardium is composed of longitudinally, circumferentially (or radially), and obliquely oriented fibers (Armour and Randall 1970). Radial and longitudinal fiber contractions result in radial and longitudinal shortening during systole (Henson, Song et al. 2000). Contraction of the helical fibers results in a twisting of the left ventricle along its long axis (Streeter, Spotnitz et al. 1969). However this rotation is minimal

and is below 15 degrees during the cardiac cycle (Henson, Song et al. 2000). Therefore the motion of the myocardium is decomposed in two main movements of the myocardial fibers during the cardiac cycle: longitudinal along the major axis of the heart and circumferential. The motion directions are fairly constant throughout the cardiac cycle and only the direction will change between systole and diastole.

For vascular applications, techniques for investigation of arterial wall motion are becoming more and more important for the assessment of atherosclerosis. Most of these measure motion of a single diameter, providing time-displacement waveforms, from which can be derived measures of elastic modulus (Wilson, Whyman et al. 1999; Wilson, Hoskins et al. 2000). A technique, which was developed by Bonnefous (Bonnefous, Montaudon et al. 1996), extends this approach, providing information on the relative movement in the longitudinal direction. This information is currently unavailable using any other imaging modality, and does seem to offer great potential in assessment of the dynamic behavior of arterial plaque. By examination of such features as local motion along an arterial segment it is possible to both quantify and image the dynamic function of the arterial walls. This approach provides fundamental new knowledge of the physical mechanisms for rupture of carotid plaque. However this technique is derived from Tissue Doppler Imaging and therefore is angle dependent. To study superficial vessel wall motion a linear array ultrasound transducer is applied on the skin over the region of interest, and the arterial tissue is dilated by the normal cardiac pulsation. In the plane perpendicular to the vessel long axis, tissue motion mainly occurs radially within the vessel wall (Ryan and Foster 1997; Maurice, Ohayon et al. 2004) while the ultrasound waves propagates axially, or in depth. Therefore a one-component velocity technique

cannot fully assess the radial motion from every part of the vessel wall.

This section describes how TDI can be extended by acquiring a real time two-component velocity vector via a dual beam vector Doppler technique. A vector Doppler velocity estimator using a small interbeam angle can suffer from both bias and large variance. This estimator is also strongly dependent on the settings of the echographic system. To reduce the large bias and variance, most vector velocity techniques use a very large ensemble length (EL) (>20), which does not allow real time implementation. A new processing technique is proposed. This technique reduces the bias and the standard deviation of the vector velocity estimate. In cardiology and vascular applications it has been shown that the motion axis for one moving tissue target varies slowly throughout the cardiac cycle (longitudinal and circumferential for myocardial wall motion and radial for vessel wall motion). The new method uses this observation and translates it into the fact that the vector velocity angle will vary slowly over the cardiac cycle than the velocity magnitude. This method has also been suggested and used for flow applications by (Lee, Chiang et al. 1999; Steel, Fish et al. 2003). The angle can then be estimated using a large time window, and the velocity magnitude will be estimated using this filtered orientation and spontaneous (non-temporally filtered) Doppler frequency shift (c.f. equation 1-1). The performance of this new technique is tested experimentally using a tissue mimicking rotating phantom and different temporal filter length.

The chapter is organized as follows: in section 4-2, the dual beam vector Doppler technique and the novel processing technique to reduce the bias and variance of the velocity estimate are described; in section 4-3, a phantom validation to optimize the TDI settings is presented.

4.2. Dual Beam Vector Doppler for Tissue Motion Imaging

A similar approach to the previous chapter is used. It utilizes a single transducer array, transmitting ultrasound from a single aperture and receiving backscattered echoes from two sub-arrays defined by contiguous sets of elements, on either side of the transmit aperture. **Figure 4-1** illustrates the transmit/receive aperture configuration. The receive aperture/subapertures are placed symmetrically across the centre the transmit aperture (the transmit/receive aperture can slide to acquire the full two-dimensional image) and the size of sub-apertures are equal. The transmit aperture emits an acoustic beam steered in the direction ϕ (ϕ is measured from a normal to the array). In reception the echoes backscattered from moving targets are received by the receive sub-apertures simultaneously.

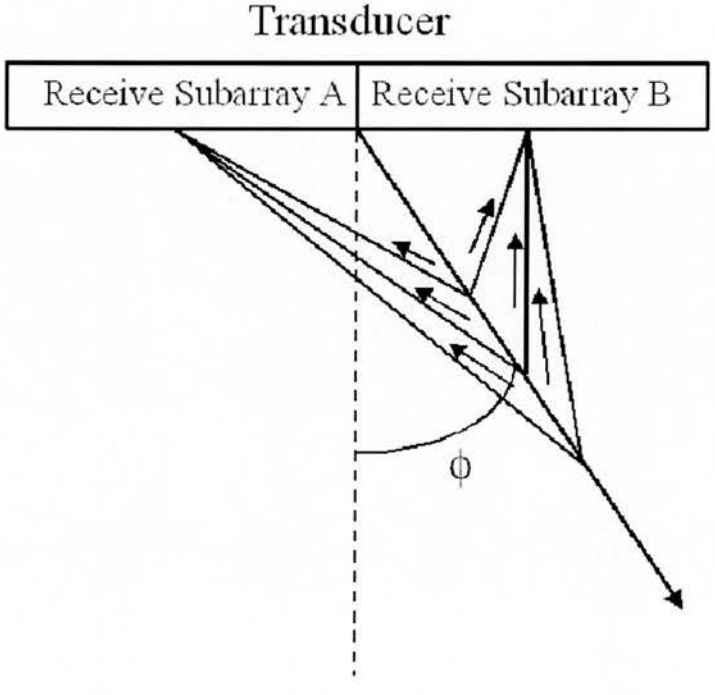

Figure 4-1: Aperture Receive Configuration

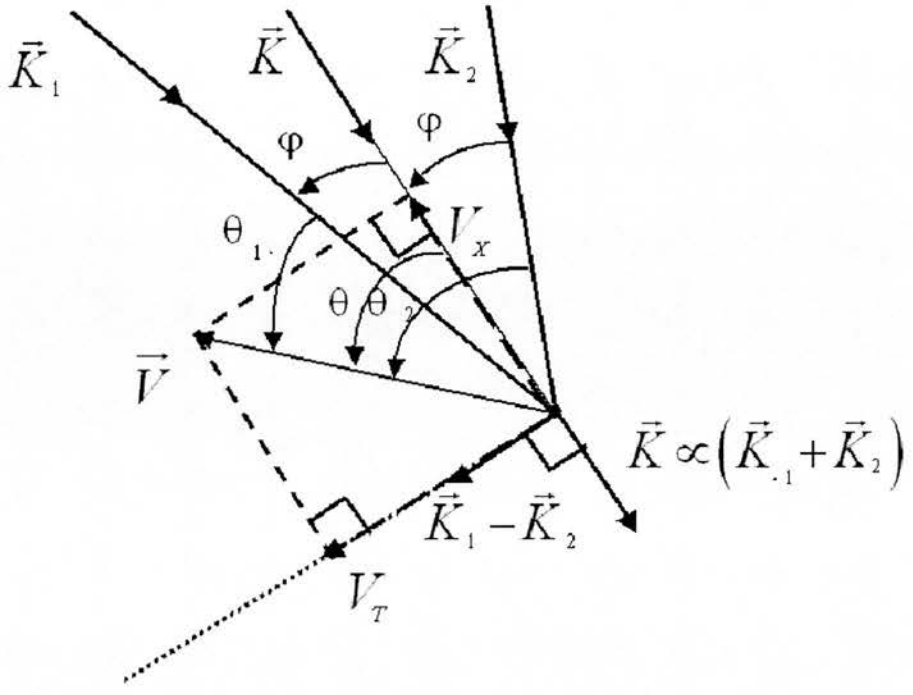

Figure 4-2: Aperture Receive Configuration

In **figure 4-2**, $\vec{K}$ is a unit vector in the direction of the transmitted ultrasound beam, and $\vec{K_1}$ and $\vec{K_2}$ are unit vectors parallel to the two receiving directions. If the position of the left and right sub-aperture centers are such that the vectors $\vec{K_1}$ and $\vec{K_2}$ subtend the same angle φ with respect to the transmit wave vector $\vec{K}$, the vector sum $\vec{K_1} + \vec{K_2}$ is parallel to the transmit beam-steering direction and therefore to $\vec{K}$. The vector difference $\vec{K_1} - \vec{K_2}$ is perpendicular to the beam-steering direction and therefore to $\vec{K}$. The targets move with a certain velocity $\vec{V}$, which is at an angle θ to the direction of the incident ultrasound beam.

If scatterers move with a velocity $\vec{V}$ past a sample volume in the insonified field of view, the mean Doppler frequency shifts $\overline{f_1}$ and $\overline{f_2}$ are given by the following equations (4-1):

$$\begin{aligned} \overline{f_1} &= \frac{|\vec{V}|\left[\cos(\theta_1)+\cos(\theta)\right]f_0}{c} \\ \overline{f_2} &= \frac{|\vec{V}|\left[\cos(\theta_2)+\cos(\theta)\right]f_0}{c} \end{aligned} \tag{4-1}$$

where c is the speed of the ultrasound wave in the medium insonified, f_0 is the transmit center frequency, θ_1 is the angle between the left receive beam and the velocity direction $\vec{V}$ and θ_2 is the angle between the right receive beam and the velocity direction.

By solving the geometrical equations it can be found that the orientation of the vector velocity is:

$$\theta = \tan^{-1}\left[\frac{\left(\overline{f_1}-\overline{f_2}\right)}{\left(\overline{f_1}+\overline{f_2}\right)}\times\frac{\left(\cos(\varphi)+1\right)}{\sin(\varphi)}\right] \tag{4-2}$$

It can also be shown that equation (4-1) can be expressed as function of scalar product of unit ultrasound wave vectors:

$$\begin{aligned} \overline{f_1}\times\frac{c}{f_0} &= \left(\overrightarrow{K_1}+\vec{K}\right)\bullet\vec{V} \\ \overline{f_2}\times\frac{c}{f_0} &= \left(\overrightarrow{K_2}+\vec{K}\right)\bullet\vec{V} \end{aligned} \tag{4-3}$$

By adding and subtracting the previous equations we obtain:

$$\begin{aligned} \left(\overline{f_1}+\overline{f_2}\right)\times\frac{c}{f_0} &= \left(\overrightarrow{K_1}+\overrightarrow{K_2}+2\vec{K}\right)\bullet\vec{V} \\ \left(\overline{f_1}-\overline{f_2}\right)\times\frac{c}{f_0} &= \left(\overrightarrow{K_1}+\overrightarrow{K_2}\right)\bullet\vec{V} \end{aligned} \tag{4-4}$$

The difference of the receive unit vectors $\left(\vec{K_1}-\vec{K_2}\right)$ is perpendicular to the transmit beam-steering direction and therefore to $\vec{K}$, while the sum $\left(\vec{K_1}+\vec{K_2}\right)$ is proportional to $\vec{K}$ and therefore the sum $\left(\vec{K_1}+\vec{K_2}+2\vec{K}\right)$ is parallel to $\vec{K}$. Thus the beam component V_B and the transverse component V_T of the vector velocity $\vec{V}$ can be calculated with the following equations:

$$\begin{aligned} V_B &= |\vec{V}|\cos(\theta) = \frac{\left(\vec{K_1}+\vec{K_2}\right)\bullet\vec{V}+2\vec{K}\bullet\vec{V}}{2\cos(\varphi)+2} \\ &= \left(\overline{f_1}+\overline{f_2}\right)\times\frac{c}{f_0\times\left(2\cos(\varphi)+2\right)} \end{aligned} \tag{4-5}$$

$$\begin{aligned} V_T &= |\vec{V}|\sin(\theta) = \frac{\left(\vec{K_1}-\vec{K_2}\right)\bullet\vec{V}}{2\sin(\varphi)} \\ &= \left(\overline{f_1}-\overline{f_2}\right)\times\frac{c}{2\sin(\varphi)\times f_0} \end{aligned} \tag{4-6}$$

For the regular Doppler technique, the complex received signal IQ (after the QBP filtering, c.f. chapter 1) sampled at the depth of interest for a narrow band pulse can be expressed as following:

$$s = A\exp\left(2\pi jT_{PRF}\overline{f}\right) = I + jQ \tag{4-7}$$

where c is the sound velocity, $\overline{f}$ is the Doppler mean frequency shift, T_{PRF} the time between two pulse emissions, A is the amplitude of the signal.

In the case of the crossbeam configuration, the two sub-apertures receive signals can be written as:

$$\begin{aligned} s_1 &= A\exp\left(2\pi jT_{PRF}\overline{f_1}\right) = I_1 + jQ_1 \\ s_2 &= A\exp\left(2\pi jT_{PRF}\overline{f_2}\right) = I_2 + jQ_2 \end{aligned} \tag{4-8}$$

By combining the two previous equations, the sum and difference Doppler frequency shifts ($\left(\overline{f_1}+\overline{f_2}\right)$ and $\left(\overline{f_1}-\overline{f_2}\right)$) can be deduced:

$$\begin{aligned} s_1 \times s_2 &= A^2 \exp\left(2\pi j T_{PRF}\left(\overline{f_1}+\overline{f_2}\right)\right) \\ s_1 \times s_2^* &= A^2 \exp\left(2\pi j T_{PRF}\left(\overline{f_1}-\overline{f_2}\right)\right) \end{aligned} \tag{4-9}$$

The two phases of the signals described in equations (4-9) are given by:

$$\begin{aligned} phaseShift_B &= 2\pi T_{PRF}\left(f_1+f_2\right) \\ phaseShift_T &= 2\pi T_{PRF}\left(f_1-f_2\right) \end{aligned} \tag{4-10}$$

where,

$$\begin{aligned} &phaseShift_T = \arctan \\ &\left(\frac{\mathrm{Im}\left(R_1(1)\right)\mathrm{Re}\left(R_2(1)\right)+\mathrm{Im}\left(R_2(1)\right)\mathrm{Re}\left(R_1(1)\right)}{\mathrm{Re}\left(R_1(1)\right)\mathrm{Re}\left(R_2(1)\right)-\mathrm{Im}\left(R_1(1)\right)\mathrm{Im}\left(R_2(1)\right)}\right) \\ &phaseShift_B = \arctan \\ &\left(\frac{\mathrm{Im}\left(R_1(1)\right)\mathrm{Re}\left(R_2(1)\right)-\mathrm{Im}\left(R_2(1)\right)\mathrm{Re}\left(R_1(1)\right)}{\mathrm{Re}\left(R_1(1)\right)\mathrm{Re}\left(R_2(1)\right)+\mathrm{Im}\left(R_1(1)\right)\mathrm{Im}\left(R_2(1)\right)}\right) \end{aligned} \tag{4-11}$$

where $R_i(k)$ represents the autocorrelation function of lag k (integer) of s_i and is expressed as:

$$R_i(k) = \sum_{n=0}^{n=N-k} s_i(n) \times s_i(n+k)^* \tag{4-12}$$

where N is the total number of pulses sent to form a line, i is equal to 1 or 2 and k represents the autocorrelation lag.

Therefore V_T and V_B can be deduced:

$$\begin{aligned} V_B &= \frac{phaseShift_B}{2\pi T_{prf}} \times \frac{c}{f_0 \times \left(2\cos(\varphi)+2\right)} \\ V_T &= \frac{phaseShift_T}{2\pi T_{prf}} \times \frac{c}{f_0 \times \left(2\sin(\varphi)\right)} \end{aligned} \tag{4-13}$$

This combination of the in phase and quadrature signals from the two receive apertures is called heterodyning (Overbeck, Beach et al. 1992) and is used to increase the dynamic range of the difference and sum of the Doppler frequency means. In fact the orientation of the vector velocity is a function of the difference and the sum of the Doppler frequency shifts obtained from the two receive apertures: $\frac{\left(\overline{f_1}-\overline{f_2}\right)}{\left(\overline{f_1}+\overline{f_2}\right)}$. The precision of the velocity angle estimation is therefore dependent on the dynamic range of the Doppler frequency shifts $\overline{f_1}$ and $\overline{f_2}$. The Doppler frequency shifts obtained from the ultrasound system (HDI 5000, Philips Ultrasound) have 8-bit of precision. To improve the angle accuracy, instead of calculating the sum and the difference of the Doppler frequency shifts in the 8-bit space, the sum and the difference of frequency shifts can be estimated by combining the IQ pairs coming from the two receive apertures (c.f. equations 4-9 and 4-10). The main advantage of heterodyning is that the Doppler frequency shift difference and the sum are now estimated directly with an 8-bit precision.

From observation made *in vitro* and *in vivo* for tissue motion (c.f. section 4-1), it can be seen that the angle variation of the vector velocity is slower than the variation of the velocity magnitude. The novel estimator uses this assumption to apply a low pass FIR filter to reduce temporal fluctuations of the angle estimation before calculating the velocity magnitude. The arctan function also increases "in a non-linear manner" the variability of the angle estimation. The FIR filtering is therefore applied before the arctan function on the ratio $\frac{\left(\overline{f_1}-\overline{f_2}\right)}{\left(\overline{f_1}+\overline{f_2}\right)}$, used in the final calculation of the angle (c.f. equation 4-2). This filter is a conventional averaging filter and uses from 2 to 20

taps (from 2 to 20 frames in the temporal dimension). The velocity magnitude is then calculated using the filtered angle using the following equation (4-14):

$$|\vec{V}| = V_B / c\cos(\theta) \qquad (4\text{-}14)$$

where θ has been filtered.

4.3. Validation

TDI mode is currently implemented on a commercial ultrasound system (Philips Ultrasound HDI 5000). This system has been modified to acquire data in reception from two separate apertures and to do the heterodyning or conventional vector Doppler processing. The accuracy and precision of the vector Doppler measurement are strongly dependent on the acquisition settings of the ultrasound system. The processing performance is studied through experimental tests using controlled-motion rotating phantoms.

The two main factors influencing the results are the processing of the data and the precision and accuracy of the TDI velocity estimate:

- Heterodyning and conventional vector Doppler estimations have been assessed separately with and without the filtering of the angle estimation.
- The accuracy and precision of the TDI mean frequency estimate will naturally influence the accuracy and precision of vector Doppler estimators. The accuracy is mainly determined by the velocity range used for acquisition. The precision is assessed by the number of pulses transmitted per line to estimate the vector Doppler estimation (c.f. the definition of ensemble length is in section 1.4.1.5).

4.3.1. Phantom Setup

An experimental setup for the validation of the two-component motion measurements has been built. This setup includes a moving tissue mimicking phantom, a PC driven controller and a DC-motor applied to a rotating stage.

The phantom consists of a circular layer of tissue mimicking material rotating in a tank with water and glycerol (speed of sound = 1540 m/s). The tissue mimicking (TMM) is agar-based with an attenuation of 0.5 ± 0.03 dB/cm/MHz from 3 to 10 MHz and an acoustic speed of 1541 ± 3 m/s at 20 degree Celsius. This tissue mimicking material has been described by Teirlinck et al. (Teirlinck, Bezemer et al. 1998) and consists of (% weight): 82.97% water; 11.21% glycerol; 0.46% benalkoniumchloride; 0.53% 400 grain SiC powder (Logitec Ltd, Glasgow, UK); 0.94% 3 microns Al_2O_3 powder (Logitec); 0.88% 0.3 micron Al_2O_3 powder (Logitec); 3.00% Struers agar (Merck Eurolab, Roskildevej, Denmark). The circular layer is rotated around its axis by a synchronous motor via a computer-controlled gearbox (Micropump model 120-000-1100, Concord, CA). The motor also rotates a disk with uniformly spaced holes near its side. Using an optical sensor, the rotational speed accuracy and variation are assessed by looking at the frequency and frequency standard deviation coming out of the optical sensor. The tank, where the tissue-mimicking wheel is immersed, is lined with an acoustic absorber (Ceram AB, Sweden). A transducer is held above the rotating disc so that the scan-plane intersects the disc parallel to the flat sides of the disc.

4.3.2. System Modification and Data Acquisition

An HDI 5000 system (Philips Ultrasound, Bothell, WA, USA) is used to acquire the echo and TDI two-component vector velocity data. The acquisition and signal

processing software of the HDI 5000 has been modified by the author to acquire the TDI vector Doppler information for both conventional and heterodyning estimation (c.f. section 4-2). The modifications consist of enabling the beamformer to simultaneously acquire two beams from the two receive sub-apertures. The per element Radio Frequency (RF) signals are digitized with a 10-bit A/D converter and the RF data are then focused, steered along the two directions parallel to $\vec{K}_1$ and $\vec{K}_2$, respectively for sub-apertures A and B, and summed to form two 18-bit RF signals. The signal path (software) has been modified by the author to process simultaneously these two signals and obtain two IQ pairs, one for each of the receive apertures (c.f. chapter 1, section 1.4.1.6). Then the system can perform one of the two different estimations, conventional vector Doppler and heterodyning:

- If the two IQ pairs are combined using equation (4-9), the beam component V_B and the transverse component V_T of the vector velocity $\vec{V}$ (heterodyning estimation) will be calculated (c.f. **figure 4-3**). V_B is proportional to $f_1 + f_2$ while V_T is proportional to $f_1 - f_2$ (c.f. equation 4-10).
- If there is no combination, the system will calculate the velocity component for each of the receive apertures V_1 and V_2 which are the projection of the vector velocity $\vec{V}$ along the direction $\vec{K}_1 + \vec{K}$ and $\vec{K}_2 + \vec{K}$ respectively (c.f. **figure 4-4**). V_1 is proportional to f_1 while V_2 is proportional to f_2.

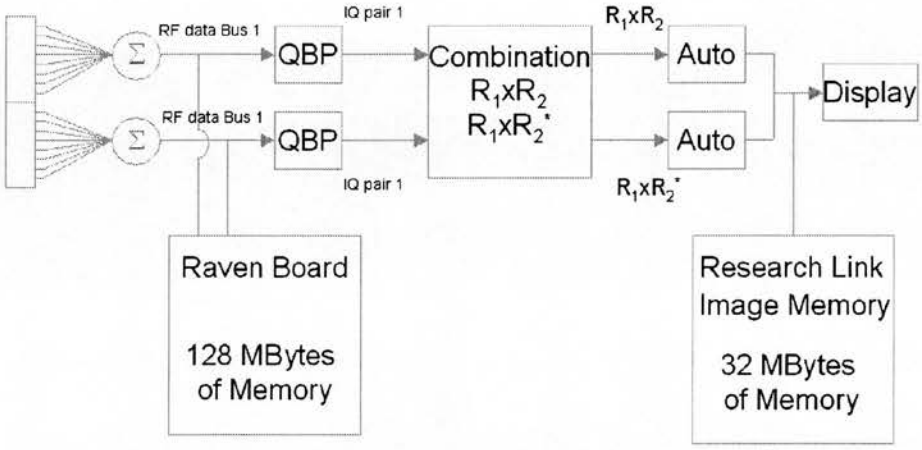

Figure 4-3: Signal path for the heterodyning estimator (combination of the two IQ pairs received from the two sub-apertures).

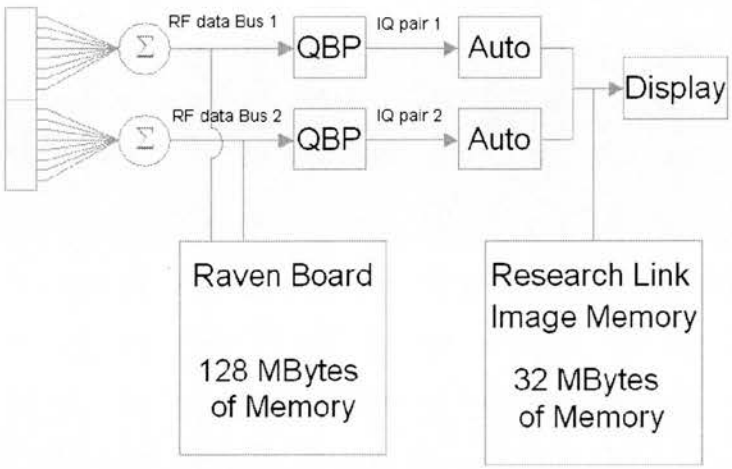

Figure 4-4: Signal path for the Vector Doppler estimator.

Figure 4-5 illustrates the data collected from the rotating phantom.

The 8-bit two-dimensional velocity estimates are then sent from the HDI 5000 image memory the directly to a PC workstation where they are processed using HDI Lab (c.f. section 3.8), an offline quantification package developed by Philips Ultrasound to support research. The velocity, as well as, some acquisition and display information data is sent to HDI Lab. A C++ HDI Lab plugin has been developed by the author to calculate the transverse, and beam velocity components, the velocity magnitude and the velocity orientation for both the heterodyning and vector Doppler estimation (c.f. **figure 4-6**).

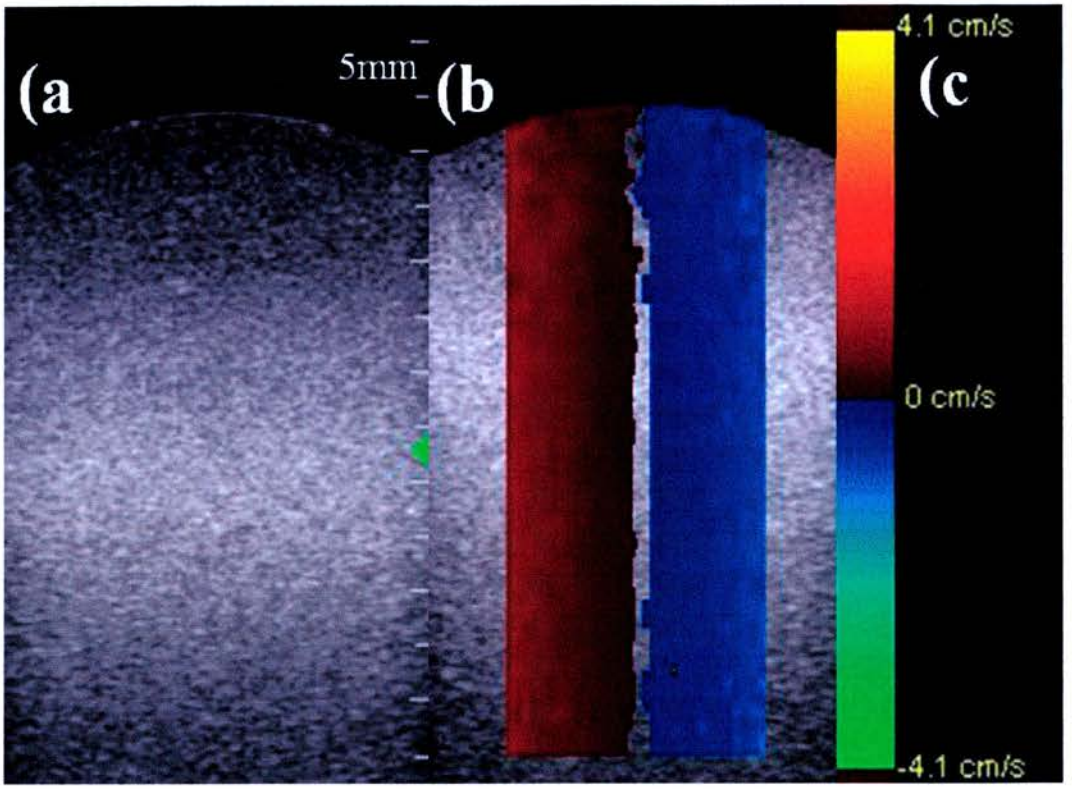

Figure 4-5: a) Conventional B-scan image of the agar-based rotating phantom. b) TDI colour-coded overlaid on B-mode. c) TDI colour bar with velocity scale.

4.3.3. Results of Validation

8-bit phase velocity data has been collected experimentally with and without heterodyning. The measured transverse and axial velocity fields are compared with the theoretical velocity field generated by knowing the center of rotation and the speed of the rotation used in the experiments (c.f. **figures 4-6, 4-7, 4-8 and 4-9**).

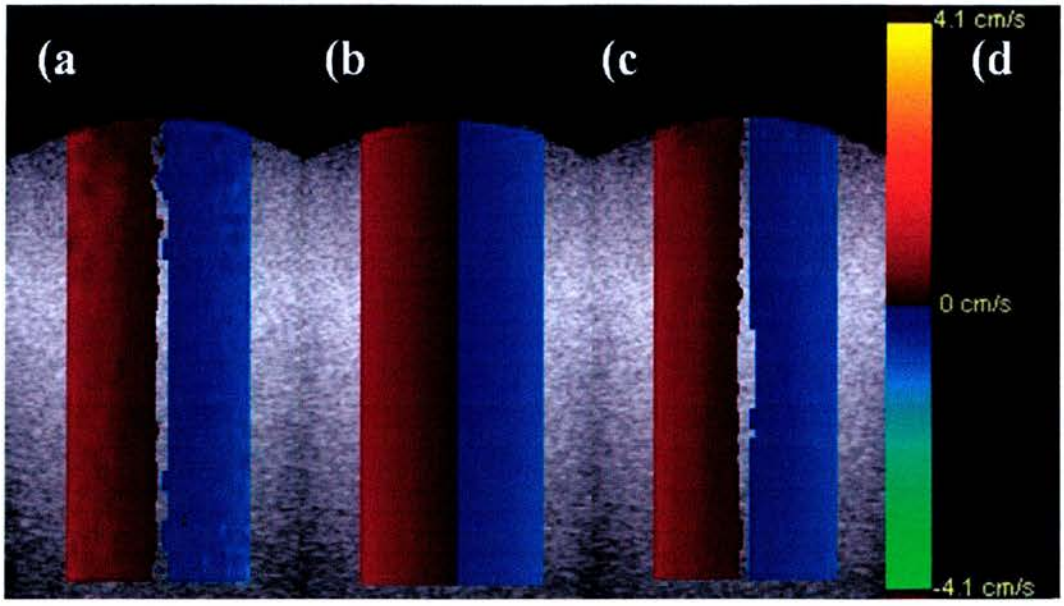

Figure 4-6: Rotating Phantom Validation Results: Axial Velocity. a) Instantaneous axial velocity colour 2D image. b) Theoretical axial velocity colour 2D image. c) Mean axial velocity over 50 frames colour 2D image. d) Colour bar with velocity scale.

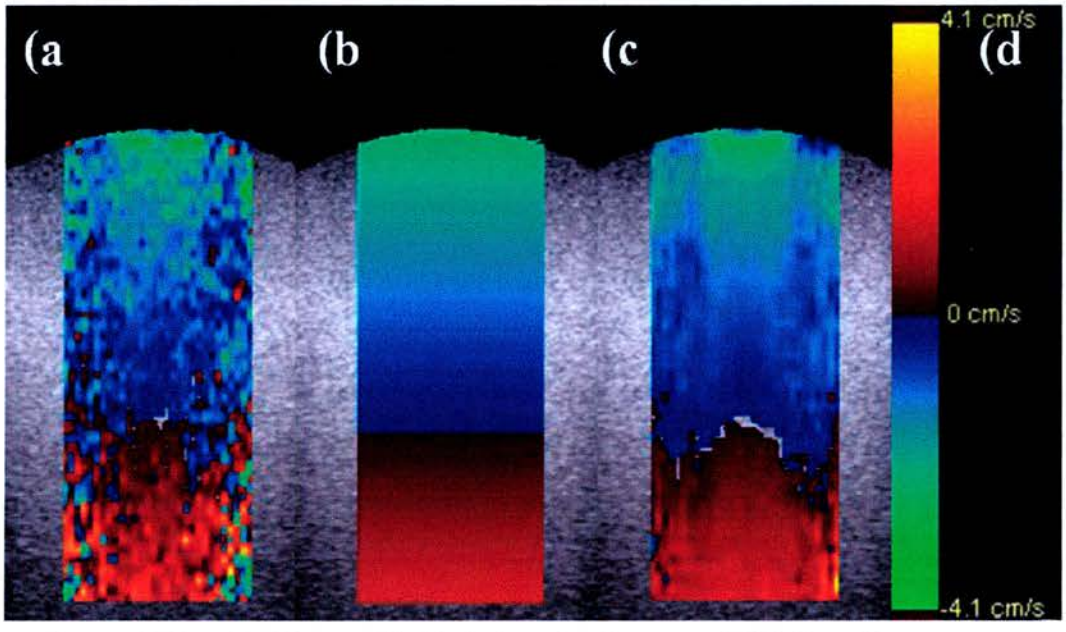

Figure 4-7: Rotating Phantom Validation Results: Transversal Velocity. a) Instantaneous transverse velocity colour 2D image. b) Theoretical transverse velocity colour 2D image. c) Mean transverse velocity over 50 frames colour 2D image. d) Colour bar with velocity scale.

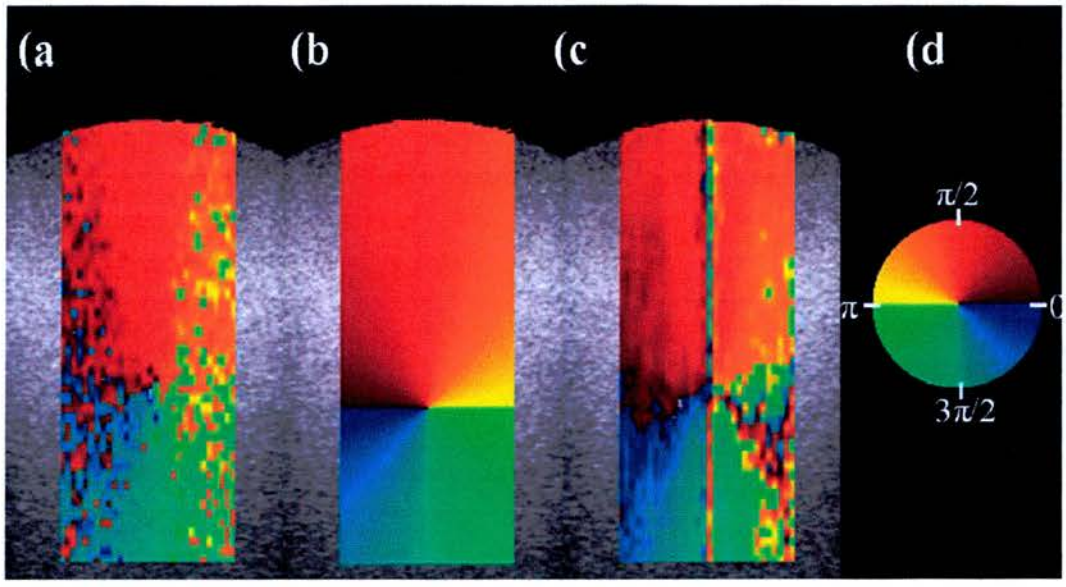

Figure 4-8: Rotating Phantom Validation Results: Orientation. a) Instantaneous velocity angle colour 2D image. b) Theoretical velocity angle colour 2D image. b) Mean velocity angle over 50 frames colour 2D image. d) Colour wheel with angle in radian.

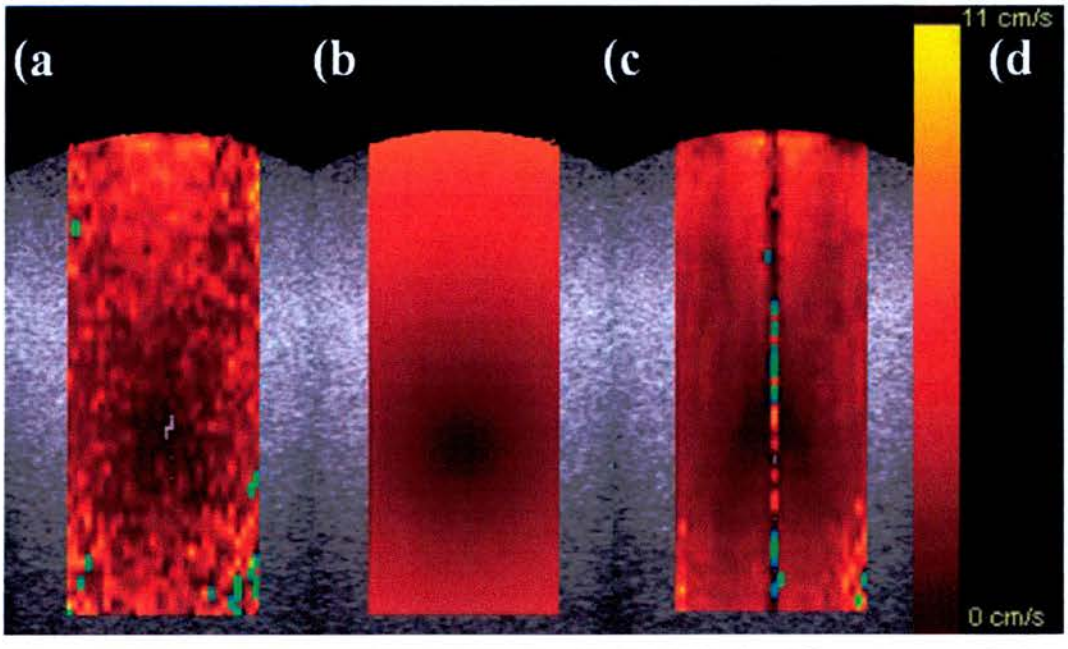

Figure 4-9: Rotating Phantom Validation Results: Absolute Velocity. a) Instantaneous velocity magnitude colour 2D image. b) Theoretical velocity magnitude colour 2D image. c) Mean velocity magnitude over 50 frames colour 2D image. d) Colour bar with velocity scale.

Standard deviation and bias are computed for all the configurations implemented in the scanner and different low pass filtering length for the vector velocity angle. These include velocity ranges (PRFs), sensitivity characteristics defined by the ensemble length (varying from 2 to 9) and filter length (varying from 2 to 20). The results presented in the following figures represent the mean bias and mean standard deviation across all angles and velocity magnitudes.

Figures 4-10 and **4-11** present standard deviation and bias of the angle and the magnitude of the vector velocity as a function of ensemble length for both vector Doppler and the heterodyning estimators.

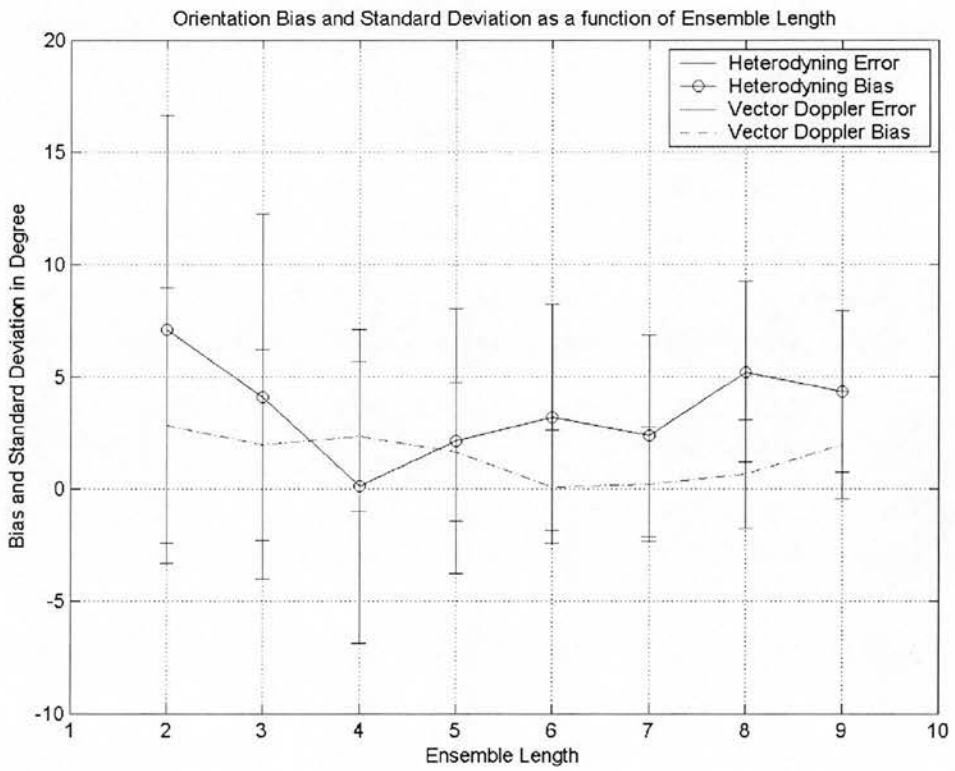

Figure 4-10: Standard deviation and bias in degree of the angle for the conventional vector Doppler and heterodyning estimators as a function of ensemble length (filter length = 20)

The overall angle bias is less than 3 degrees for the Vector Doppler Estimation (VDE) and less than 7 degrees for the Heterodyning Estimation (HE). The angle standard deviation decreases with increasing ensemble length. Overall the bias and standard deviation are smaller for VDE than for HE technique.

The bias of the velocity magnitude is also decreasing as a function of ensemble length for VDE and is below 5%. For HE the bias can be above 10% and the standard deviation is much higher than for conventional VDE. These results do not corroborate with section 4.2 where HE is introduced explicitly to reduce the standard deviation of the angle and velocity estimation. The principal reason for these results is that the combined IQ pair signals ($s_1 \times s_2$ and $s_1 \times s_2^*$, c.f. equations 4-9 and 4-10) have amplitudes in the order of the square of the original IQ pair signals (s_1 and s_2). The original IQ pairs are encoded on 16 bits. Therefore to not loose any precision the combined IQ pairs should be encoded on 32 bits. However, even though, the combination of the IQ pairs is done using 32-bit precision operation, the multiplication output (c.f. equation 4.9) is truncated down to 16 bits within the HDI 5000. The truncation is done so the combined IQ pair signals do not saturate however the lower bits get truncated and therefore some precision on the sum and the difference frequency shifts ($f_1 + f_2$ and $f_1 - f_2$) is lost. From the standard deviation results for the angle and the velocity magnitude this truncation is impacting the HE performance. Modifying the signal path of the system to support 32 bits IQ pairs would require some extensive hardware and software changes. Therefore HE could not be fully assessed on the commercial system used (HDI 5000). However a future system will certainly support 32 bit IQ pairs up to the phase calculation. In that case the HE performance should to be revisited.

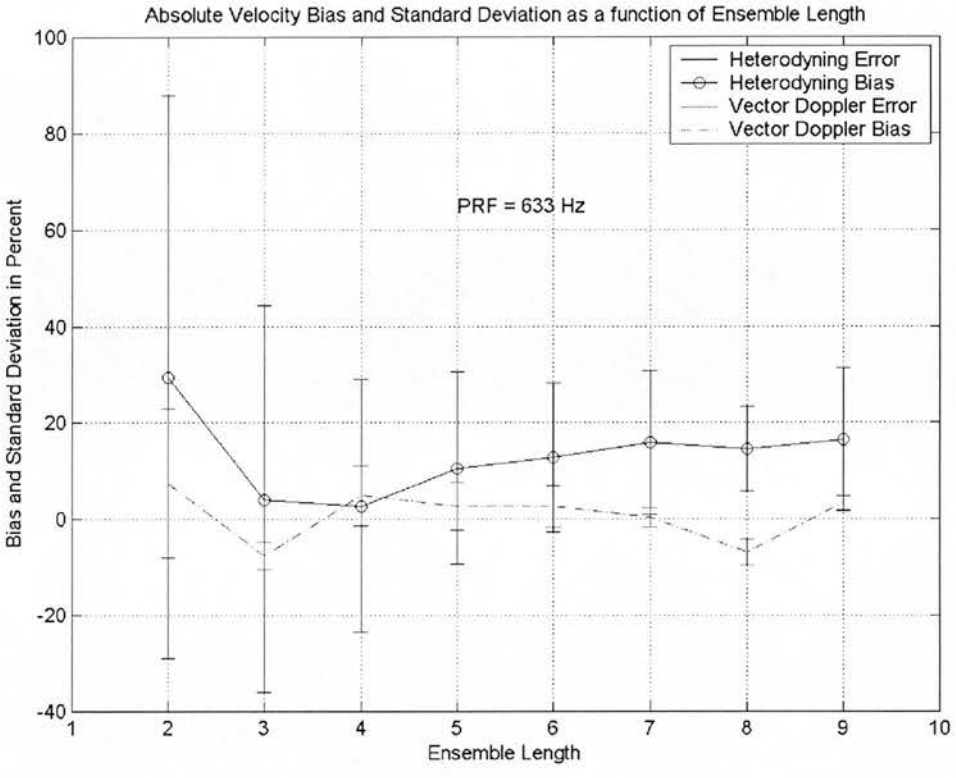

Figure 4-11: Standard deviation and bias in percent of the velocity magnitude for the conventional vector Doppler and heterodyning estimators as a function of ensemble length (filter length = 20)

Figures 4-12 and **4-13** present standard deviation and bias of the angle and the magnitude of the vector velocity as a function of filter length for both VDE and the HE.

The angle standard deviation is decreasing as a function of increasing filter length for both VDE and HE. However the bias and error are higher for HE than for VDE. With no filtering of the angle estimation the angle standard deviation is above 20 degrees, with a filter length of 20 it reduces below 7 degrees and the bias around 5 degrees, which offers improved quantification over the conventional single beam methods.

The bias of the magnitude is also decreasing as a function of filter length and is below 5% for VDE. This effect was expected (c.f. section 4.2) and this validation confirms the effect of the filter length on the estimation.

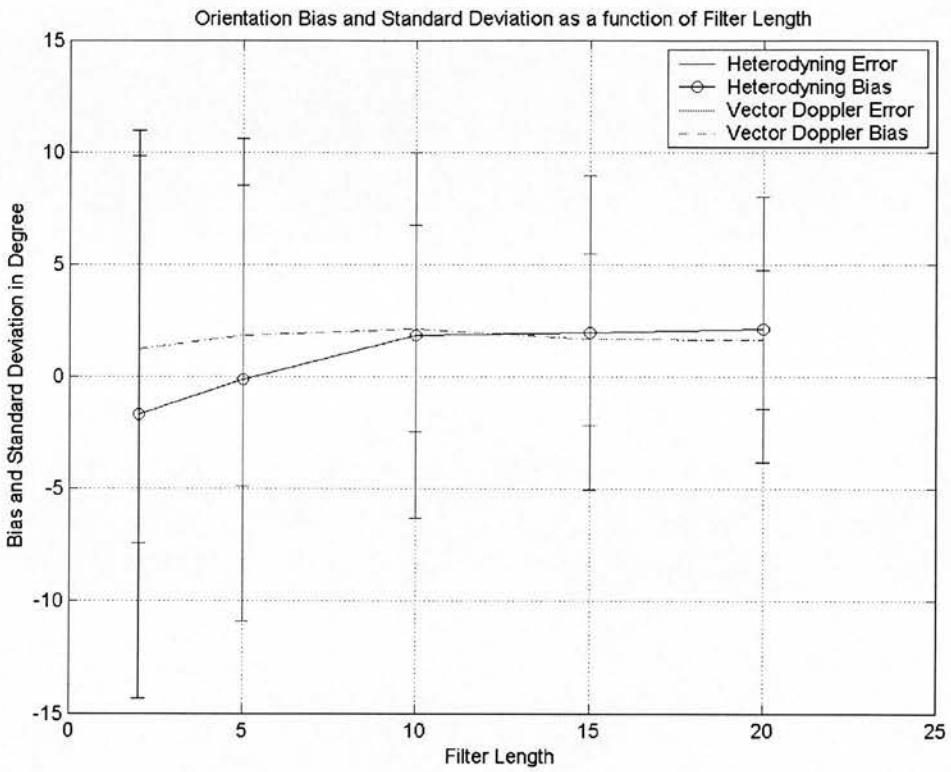

Figure 4-12: Standard Deviation and Bias in degree of the Angle for the conventional vector Doppler and heterodyning estimators as a function of filter length (ensemble length = 5)

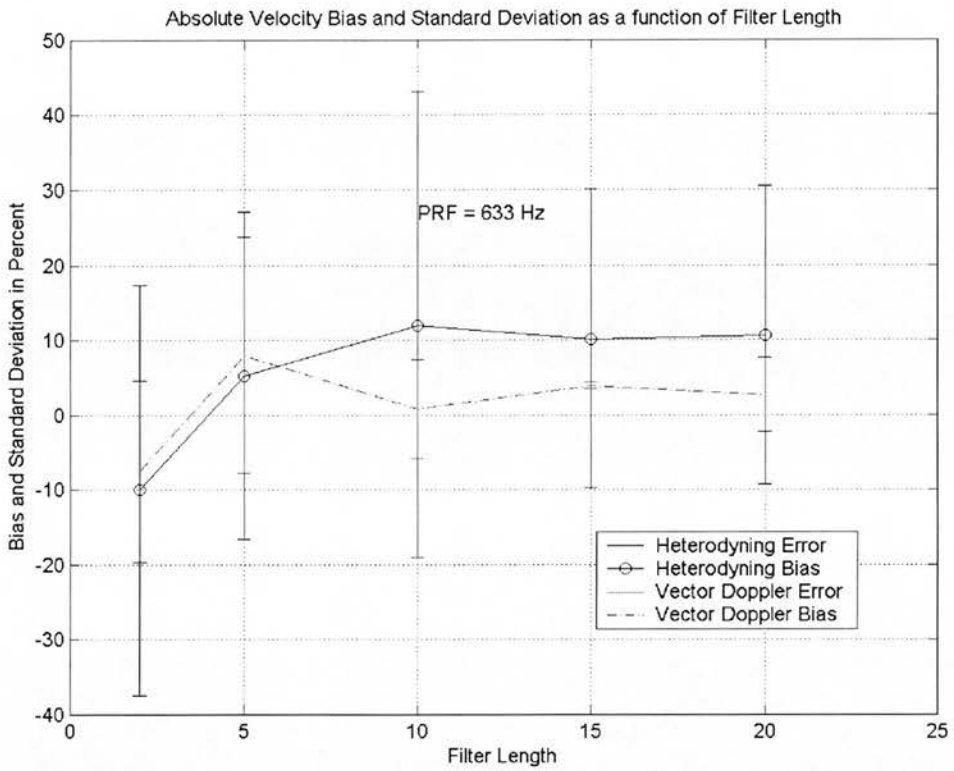

Figure 4-13: Standard Deviation and Bias in percent of the Magnitude for the conventional vector Doppler and heterodyning estimators as a function of filter length (Ensemble Length = 5)

Figures 4-14 and **4-15** present standard deviation and bias of the angle and the magnitude of the vector velocity as a function of PRF for both VDE and HE.

The angle bias is stable as a function of PRF for both VDE (5 degree bias) and HE (10 degree bias). However the standard deviation is higher for HE than for VDE.

The bias of the velocity magnitude does not vary with the PRF and is below 5% for VDE. However the standard deviation increases with the PRF, which is directly linked to the fact that the velocity precision decreases with increasing PRFs.

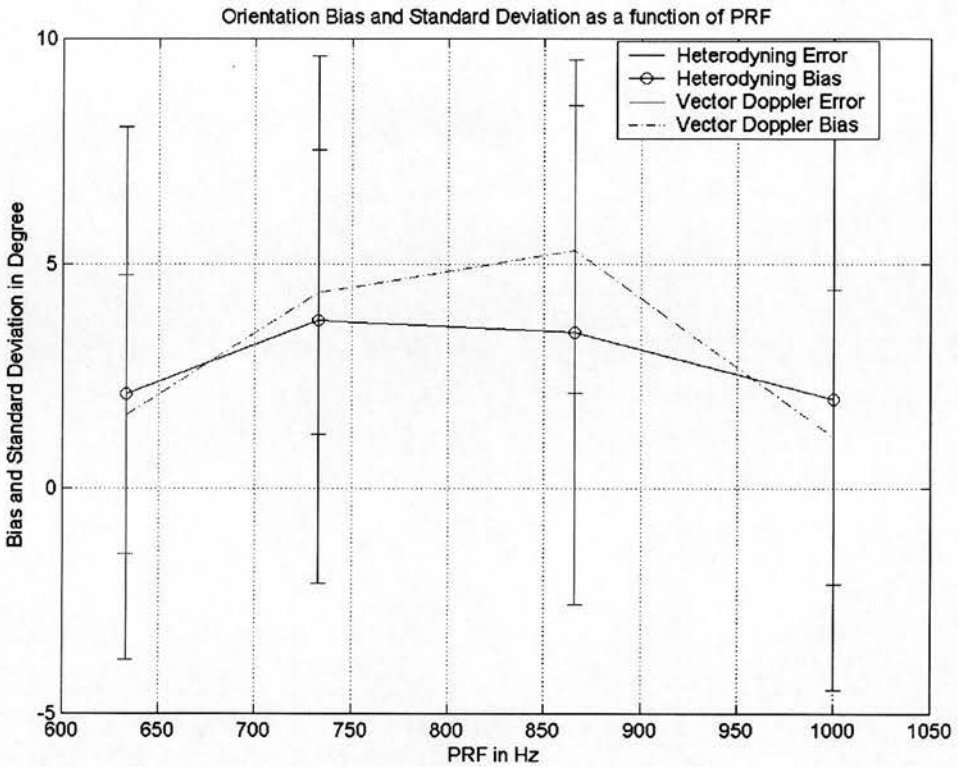

Figure 4-14: Standard Deviation and Bias in degree of the Angle for the conventional vector Doppler and heterodyning estimators as a function of PRF (filter length =20, ensemble length =5)

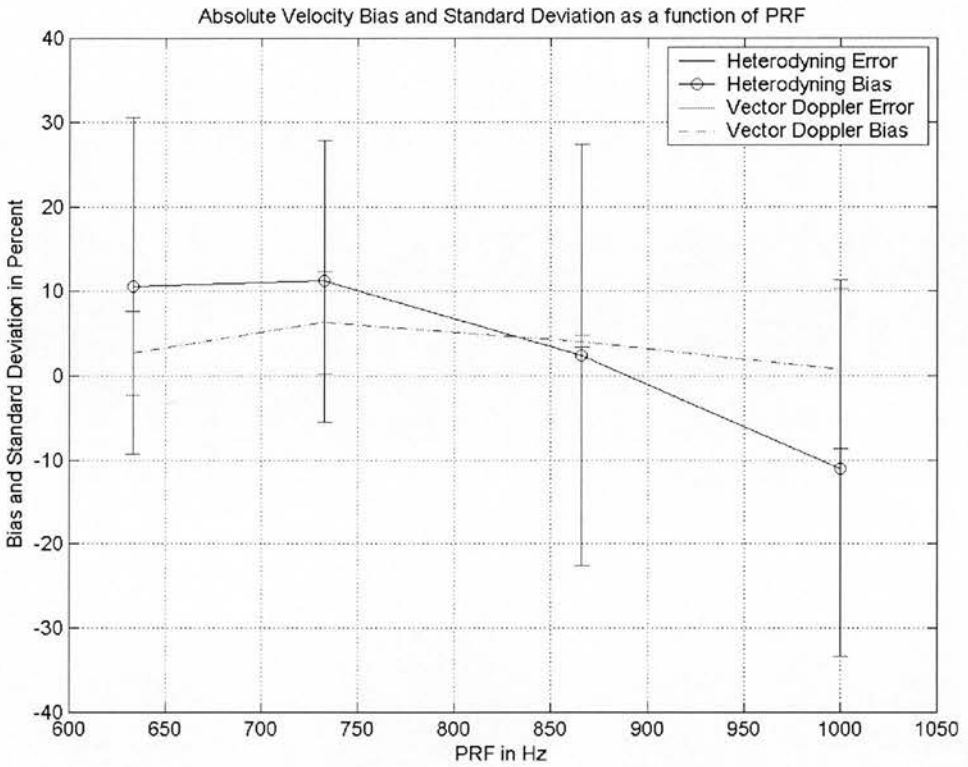

Figure 4-15: Standard Deviation and Bias in percent of the Magnitude of the conventional vector Doppler and heterodyning estimators as a function of PRF (filter length = 20, ensemble length = 5)

These results permit the definition of the best acquisition and processing settings to estimate the tissue vector velocity magnitude and orientation. One of the first conclusions is that vector Doppler estimation has a lower bias and standard deviation than the heterodyning because of the dynamic restriction within the processing chain of the HDI 5000 (see explanation above). Therefore this estimator should be used to assess two-component tissue vector velocities. The PRF should be set just above the aliasing point to reduce the standard deviation of the velocity magnitude. The ensemble length should be set to 4 or 5 to decrease the standard deviation and bias of the angle estimation and still allow very fast frame rate acquisition. The temporal

filtering decreases the standard deviation of both angle and velocity magnitude and should be set to 20. With these settings a bias less than 5 degree and a standard deviation around 5 degrees can be achieved for the angle estimation. The overall velocity magnitude estimator performance shows a bias less than 5% with a standard deviation less than 10%.

The standard deviation and bias values (5-10 %) demonstrate that a quantitative characterization of angle and velocity estimation can be performed.

4.4. Conclusion

In this chapter it has been demonstrated that vector TDI offers improved performance in terms of velocity magnitude estimation over conventional single beam TDI, though the clinical validation of this technique remains to be established. From the results presented in this chapter, it can be seen that two component tissue motions can be assessed, as quantitative tool. It is shown that the factors influencing the results are the ensemble length, the precision of the TDI estimates and the time window of the temporal filtering applied to the angle direction. The results indicate that the variance and bias of velocity magnitude and orientation estimates decrease with increasing EL, increasing precision of the TDI estimates and increasing time window. Using an EL of 4 or 5, 8 bits for the velocity estimate, and an observation time of one second, a 5-degree bias of the angle estimate is observed, with a variance below 5 degree averaged over all angles. A 5% bias of the velocity magnitude is observed, with a variance of 10%.

5. Real Time One-Component Strain Rate Imaging

5.1. Introduction

This section describes how the Tissue Doppler Imaging (TDI) technique can be adapted to allow deformation characterization of arterial and cardiac walls in two-dimensional images. Such a characterization relies on the definition of clinically relevant physiological parameters, a specific optimization of the TDI settings and the validation of the parameter measurements. The non-invasive quantification of regional tissue function is an important goal in the clinical environment, especially to assess myocardial and arterial mechanical properties (Bassiouny, Davis et al. 1989). A new ultrasonic method for quantifying regional deformation is introduced in this chapter based on the principle of strain rate. This technique has been investigated by Heimdal et al. and D'Hooge et al. (Heimdal, Stoylen et al. 1998; D'Hooge, Heimdal et al. 2000; D'Hooge, Konofagou et al. 2002). One-dimensional strain rate, since it is derived from 1-C TDI, is angle dependent. This problem can be partially corrected by making sure the insonification is parallel to the displacement direction during acquisition of the data sets. However this is not always possible due to the access window used for imaging. In cardiology applications especially, the heart is accessible only via a few windows due to ribs and lungs and therefore the ultrasound beam can always be parallel to the motion. In this chapter a technique is presented to assess the deformation along one direction that can be corrected for the Doppler angle dependence bias. This correction is made by a visual assessment of the deformation direction.

This chapter is organized as follows: in section 5-2, the definition of strain and strain rate is given; in section 5-3 the current techniques used for measuring strain rate are described; in section 5-4, physiological parameters are introduced and the principle

of their measurements is described; in section 5-5 a new estimator for one-component strain rate is described; in section 5-6, a phantom validation of the method is presented; in section 5-7 a correction for the one-component strain rate is proposed with a validation on a phantom; section 5-8 provides clinical example of one-component strain rate imaging.

5.2. One-Component Strain and Strain Rate Definitions

Strain is defined as the deformation of an object, normalized to its original shape. For a one-component object (i.e. an infinitesimally thin bar), the only possible deformation of the object is the lengthening or shortening. This is illustrated in **figure 5-1**. The relative amount of deformation is defined as strain. Strain, S, can thus be written as:

$$S = \frac{L - L_0}{L_0} \qquad (5\text{-}1)$$

with L the length of the object after deformation and L_0 its original length. Strain is therefore a dimensionless quantity (it is often expressed as a percentage).

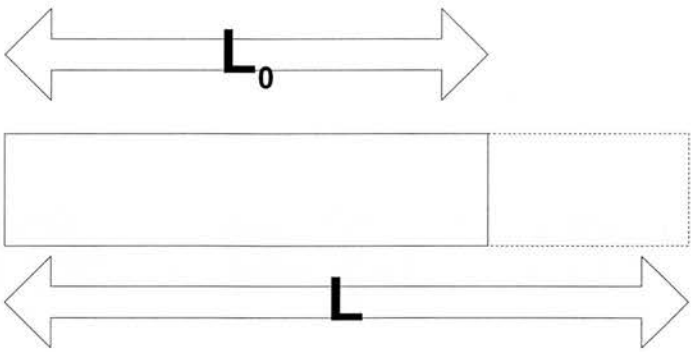

Figure 5-1: Deformation (strain of a one-component object is limited to lengthening or shortening. Strain is the deformation of an object relative to its original shape.

By convention equation 5-1 is defined such a way that the lengthening is represented as a positive value for strain, while the shortening is represented by a negative value. Strain rate is the speed at which the deformation (i.e. strain) occurs. It is represented by the symbol SR and has a unit s^{-1}. The rate of deformation is a tensor that describes the rate of change of a length in an object. For small displacements and infinitesimal strains, as the ones occurring from frame to frame in ultrasound imaging, the rate of deformation tensor is approximately equal to the time derivative of the infinitesimal strain tensor, thus explaining the term "strain rate". The rate of deformation is in the one-component case given as the spatial velocity gradient.

5.3. Existing Methods to Calculate Strain Rate

5.3.1. Myocardial Velocity Gradient

In 1994, Fleming et al. (Fleming, Xia et al. 1994) suggested using the gradient of the TDI velocity as a measure for the relative change in the heart wall thickness:

$$-\frac{dW}{dt}\Big/W=\frac{dv}{dx} \qquad (5\text{-}2)$$

Here, W is the instantaneous wall thickness and dv/dx is the velocity gradient across the wall. This gradient was found as the slope of the linear regression of the TDI velocity estimates. Only velocities measured with the ultrasound beam perpendicular to the heart were used.

In 1995, Uematsu et al. (Uematsu, Miyatake et al. 1995) expanded the method to be used also when the ultrasound beam crossed the heart wall at an angle less than 90 degrees. Short axis views were used, and the motion was assumed to be towards the center of the ventricle. The angle θ between the ultrasound beam and the assumed direction of the motion was used to angle correct the velocity data:

$$v_{corrected}=\frac{v_{measured}}{\cos\theta} \qquad (5\text{-}3)$$

The velocity profile between endocardium and the epicardium was then obtained for each radius from the center of the ventricle. The velocity gradient was finally found from the rate of inclination of each velocity profile by using least square linear regression.

5.3.2. Tracking-Based Strain Rate Imaging

In 1997, Kanai et al. (Kanai, Chiubachi et al. 1997) presented an offline strain rate imaging technique based on IQ cross-correlation. Initially, several points along an ultrasound beam perpendicular to the cardiac wall were manually chosen. The velocity $v(x,l)$ of point number x in frame number l was calculated using an IQ cross-correlation technique where the phase of the correlation function at peak magnitude was used to estimate the velocity.

$$v(x,l) = \frac{c}{2\pi \times T \times f_0} \tan^{-1}\left(C\left(x, dx_{\max}\right)\right) \qquad (5\text{-}4)$$

Here $dx_{\max}$ is the axial lag (along the ultrasound beam) that maximizes the cross-correlation function $|C(x,dx)|$. The IQ cross-correlation function is defined as:

$$C(x,dx) = \int_{x-W/2}^{x+W/2} \left[\begin{array}{l} \left[I(x',1) + jQ(x',1)\right] \\ \times \left[I(x'+dx,2) - jQ(x'+dx,2)\right] \end{array} \right] dx' \qquad (5\text{-}5)$$

where $IQ(x,1)$ and $IQ(x,2)$ were the axial IQ signals derived from pulse numbers 1 and 2, and W corresponded to the length of the pulse. The position x in frame l in the next frame was found then as:

$$x(l+1) = x(l) + T \times v(x,l) \qquad (5\text{-}6)$$

where T is the pulse repetition time. The local strain rate in each frame was finally calculated as:

$$SR(x,l) = \frac{v(x+dx,l) - v(x,l)}{dx} \qquad (5\text{-}7)$$

The strain rate was colour-coded superimposed on a grayscale M-mode image of the same position. The method was limited to areas where the ultrasound beam could be placed perpendicular to the heart wall.

5.3.3. Strain rate by tissue Doppler

This technique has first been introduced by Heimdal et al. (Heimdal, Stoylen et al. 1998; Stoylen, Heimdal et al. 1999; D'Hooge, Heimdal et al. 2000; Stoylen, Heimdal et al. 2000; Stoylen, Slordahl et al. 2001; D'Hooge, Konofagou et al. 2002). They have shown that longitudinal velocity gradient is equivalent to the measure of longitudinal strain rate. It can be shown that this is equal to the velocity gradient over

a fixed distance. In Heimdal et al. technique, strain rate by tissue Doppler measures the velocity gradient of two points over a segment with a fixed distance:

$$SR(x) = \frac{v(x+dx) - v(x)}{dx} = \frac{dv}{dx} \qquad (5\text{-}8)$$

This is a different algorithm from the velocity gradient (c.f. section 5.3.1), but it can be proved that the two techniques result in the same ratio. The distance dx is called the offset distance or strain rate length. Instead of measuring just the velocities at the ends of the offset distance, the velocity gradient / strain rate can be calculated as the slope of the regression line of all velocities along the offset distance as described originally. With perfect data, the values will be identical, both technique defining the slope. With imperfect data, this method will tend to make the method less sensitive to errors in velocity measurements, as the value is an average of more measurements. The velocity gradient can be measured by the strain rate imaging method, which is quicker than tracing the endo- and epicardial borders.

5.4. Description of Measured Quantities

The motion of biological structures seen by TDI is due to the interaction between internal mechanical forces (arterial pressure, myocardium contraction/relaxation strength) with tissues (arterial wall, myocardium). Using TDI sequences, it is possible to extract specific physiological parameters, which can be imaged and used to assess the deformation abilities of the cardiac and arterial walls.

In this section one-component rate of deformation (or one-component strain rate) is investigated. However before describing strain rate it is important to understand how other quantities, such as motion, dilation or strain can be derived from tissue velocities.

Let x be the coordinate of a point along the acoustic beam and inside the structure of interest. The displacement of this point M(x,t) is estimated by :

$$M(x,t) = \int_{t_0}^{t} V(x,u)du \qquad (5\text{-}9)$$

where V(x,t) is the velocity provided by the Tissue Doppler Imaging (TDI), and t_0 is for instance the beginning time of the cardiac cycle.

Strain is the representation of the deformation of a medium. Given two close positions x and (x+δx) along the acoustic beam and inside the structure of interest, the strain S(x,t) equals :

$$S(x,t) = \frac{M(x+\delta x,t) - M(x,t)}{\delta x} = \frac{\partial M(x,t)}{\partial x} \qquad (5\text{-}10)$$

The strain rate SR(x,t) represents the velocity of compression or dilation of the tissue. It is defined by:

$$SR(x,t) = \frac{\partial S(x,t)}{\partial t} \qquad (5\text{-}11)$$

From (5-9) and (5-10), it follows that the strain rate can be directly derived from the Tissue Doppler Imaging information:

$$SR(x,t) = \frac{\partial V(x,t)}{\partial x} \qquad (5\text{-}12)$$

From a physics point of view, strain rate (SR(x,t)) is equivalent to the spatial gradient of the velocity.

5.5. Real Time One-Component Strain Rate Estimator

In the previous sections 5-3-1 and 5-3-2, myocardial velocity gradient and tracking-based strain rate techniques are non real time estimators to visualize the rate of

deformation of the insonified structured. In this section a real strain rate estimator based on IQ signals is developed.

The derivation of the velocity signal as a function of depth can be calculated from the phase difference in between two $R(1)(x,t)$ estimates along the depth direction divided by the distance in between these two estimates. The calculation of the phase estimates $R(1)(x,t)$ is performed using the I and Q samples, according to the conventional lag-one autocorrelation approach:

$$R(1)(x,t)=\sum_{n=1}^{N-1}\left[\begin{array}{l}\left[I\left(x,t+\frac{n}{PRF}\right)+jQ\left(x,t+\frac{n}{PRF}\right)\right]\\ \times\left[I\left(x,t+\frac{(n+1)}{PRF}\right)-jQ\left(x,t+\frac{(n+1)}{PRF}\right)\right]\end{array}\right] \quad (5\text{-}13)$$

where N is the colour ensemble length and PRF is the pulse repetition frequency in Hz. To get the Doppler phase shift of the signal, the mean phase estimate is calculated with the following equation:

$$\theta(x,t)=\tan^{-1}\left(\frac{\mathrm{Im}\left[R(1)(x,t)\right]}{\mathrm{Re}\left[R(1)(x,t)\right]}\right) \quad (5\text{-}14)$$

The equations above represent the calculation of the Doppler phase shift. We can also define the strain rate estimate $SR(x,t)$ from $R(1)(x,t)$ estimates with the following equation:

$$SR(x,t)=\sum_{d=-D/2}^{D/2}\left[R(1)(x+d\times\delta x,t)\times R(1)(x+(d+1)\times\delta x,t)^{*}\right] \quad (5\text{-}15)$$

where D represents the kernel size (along depth), x is the depth along the acoustic beam, $R(1)(x+d\times\delta x,t)^*$ is the complex conjugate of $R(1)(x+d\times\delta x,t)$, d is an increment ranging from –D/2,… , D/2, and δx is the distance between to consecutive points along the acoustic beam. Then the strain rate phase and strain rate can be deduced using the following equations:

$$SRPhase(x,t)=\tan^{-1}\left(\frac{\mathrm{Im}\left[SR(x,t)\right]}{\mathrm{Re}\left[SR(x,t)\right]}\right) \qquad (5\text{-}16)$$

$$SR(x,t)=\frac{c\times PRF}{-4\pi\times f_0\times\delta x}SRPhase(x,t) \qquad (5\text{-}17)$$

To increase the robustness of the technique and if it is assumed that the strain rate is constant within the kernel another way of estimating the strain rate correlation is described by equation (5-17):

$$SR(x,t)=\sum_{k=1}^{D}\frac{1}{k}\left[\sum_{d=-D/2}^{D/2-k}\left[R(1)(x+d\times\delta x,t)\times R(1)(x+(d+1+k)\times\delta x,t)^*\right]\right] \qquad (5\text{-}18)$$

This last equation uses all possible autocorrelation lags.

The lag one autocorrelation function (R1) is a robust technique because it takes into account not only of the phase but also the magnitude of the signal when calculating the autocorrelation estimation. The R1 autocorrelation technique gives increased weight to the velocity estimates, which have a lowest variance (strong signals). The R1 autocorrelation technique is equivalent to a linear regression technique (fitting the velocity estimates with a straight line and calculating the slope of the line to estimate the strain rate) but allows weighing each velocity estimate with the power of the Doppler signal (or the strength of the Doppler signal).

5.6. Validation of One-Component Strain Rate Imaging

Strain rate is estimated through the TDI mode implemented on a commercial ultrasound system (Philips Ultrasound HDI 5000). The accuracy of the measurement is strongly dependent on the acquisition settings of the ultrasound system and the characteristics of the biologic motion/strain curves to be evaluated. The processing performance is studied through experimental tests using controlled-compressed agar-based phantoms.

The two main factors influencing the strain rate estimates are the scanning sequences and the precision of the TDI velocity estimate. The accuracy of the TDI estimate will naturally influence the accuracy of all the derived quantities. This is mainly determined by the velocity range and the ensemble length used for acquisition.

An experimental setup for the validation of strain rate measurements includes a phantom, a PC driven controller (MM4005, Micro-Controller) and a DC-motor applied to a translation stage (UTMCC.5HA). One block of agar shaped as a cylinder of 1.5 centimeter height and 8 centimeter diameter is used as the phantom. This phantom is laid on an acoustically transparent film and a steel plate driven by a piston is compressed in its main axis direction. The size of the steel plate is 5 by 5 centimeter. The transducer is placed underneath the film. The film and the phantom are acoustically coupled by some gel (Aquasonic, Parker Laboratories, Inc.). The surface where the phantom lies is flat and its size is 20 cm by 50 cm. The phantom is located in the middle of this surface to make sure that when the compression is applied the sides of the phantom are not constrained. **Figures 5-3** and **5-4** illustrate the phantom, the plate, the piston and the transducer setup. A HDI 5000 system (Philips Ultrasound, Bothell WA, USA) and a L12-5 linear transducer (5 to 10 MHz)

are used to acquire the 8-bit echo and TDI 8-bit (acquired with a 7.5 MHz transmit frequency) data (c.f. **Figures 5-2**). Loops of TDI and echo of at least 3 seconds are acquired for each acquisition setting.

Figure 5-2: Setup with HDI 5000 the phantom and the motor controller.

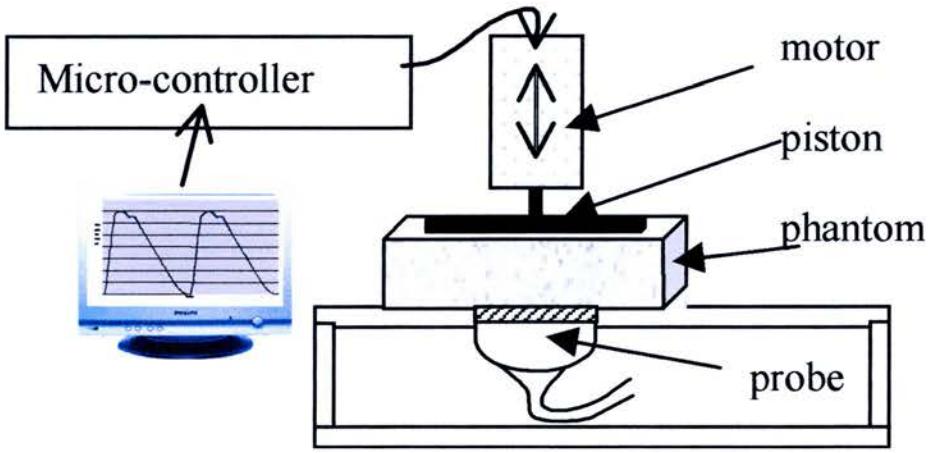

Figure 5-3: Setup for phantom validation of one-component strain rate.

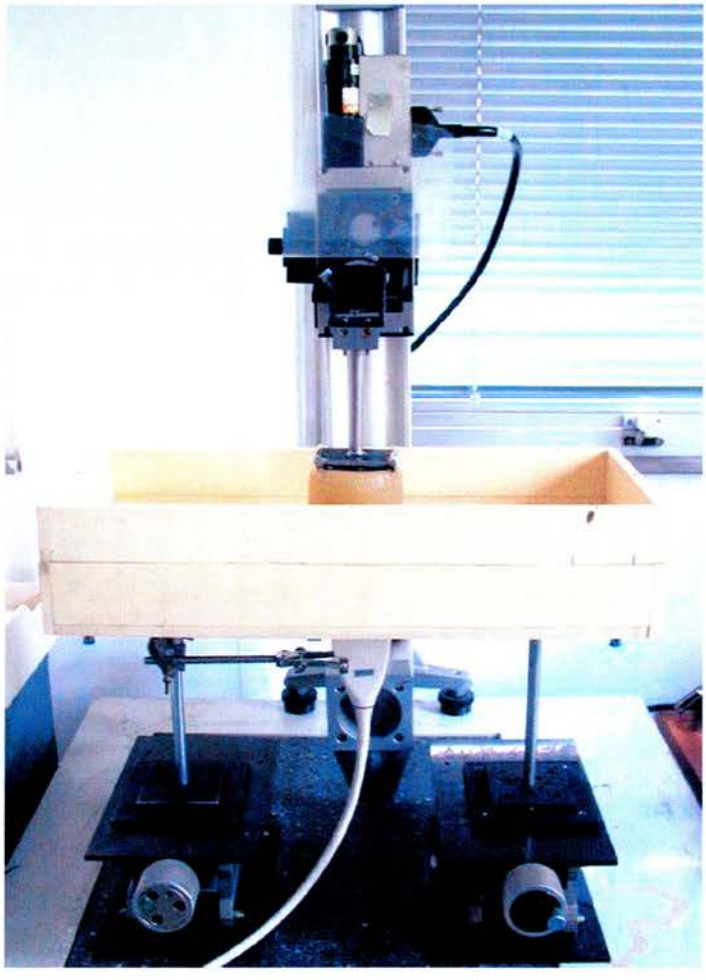

Figure 5-4: Setup for phantom validation of one-component strain rate.

To derive the strain rate information the strain kernel size, D in equation 5-15, is equal to 30 TDI samples along a line. The TDI colour box size is 84 samples deep by 7 lines wide. The mean strain rate and standard deviation strain rate are calculated on a Region of Interest (ROI) of 54 x 7 samples located in the middle on the phantom which corresponds to a 10 (width) x 10 (height) mm^2 region. The TDI colour box size and the ROI (in green) used to estimate the mean and the standard deviation of the strain rate are shown in **figure 5-5-a**. The resulting 2-D strain image is shown in **figure 5-5-b**. In **figure 5-5-a** the TDI image shows a linear gradient from top to bottom in the velocity estimates. The phantom region closed to the piston moves

faster (bright red colours) than the part that is closed to the transducer (dark red colours). In **figure 5-5-b the** 2D strain rate image shows no colour gradient the strain rate is constant throughout the ROI (except from some noise fluctuation).

Given that the phantom is compressed by a large enough plate (so the compression is applied equally on a 5 by 5 cm^2 surface), that gel is used so there is no friction between the membrane and the phantom, and the piston and the phantom, and the ROI used in located in the middle of the phantom and its size is small (10 by 10 mm^2) compared to the overall phantom size, the axial deformation applied to the agar phantom should be linear in the ROI.

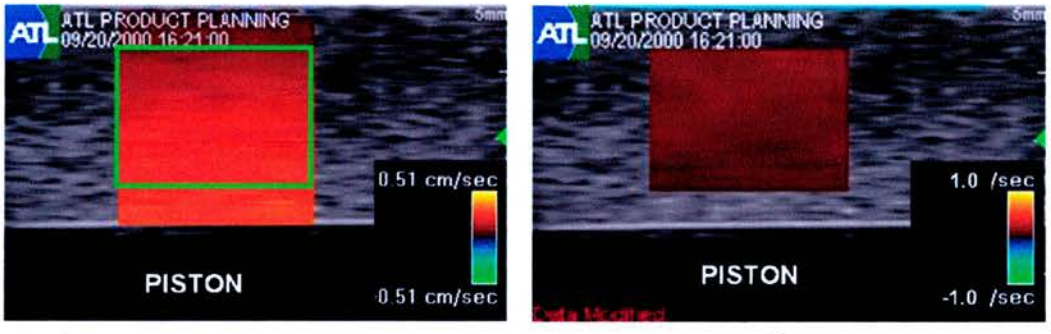

a b

Figure 5-5: Strain Agar Phantom and piston (at the bottom of the image). a) 2D and TDI image, with a linear gradient from top to bottom in the TDI velocity estimates. The phantom region closed to the piston moves faster (bright red colours) than the part that is closed to the transducer (dark red colours). The ROI used to calculate the strain rate mean and the strain rate standard deviation is shown in green. b) 2D strain rate image. No colour gradient is shown (strain rate is constant throughout the ROI).

Figure 5-6 plots the strain rate estimation, where constant strain rates are generated by the piston displacement. There is a good correlation at low values of strain rate, while the standard deviation and bias increase as a function of strain rate. For higher

compression the deformation might be less uniform than for lower compression. Therefore the high strain rates have increased bias and standard deviation.

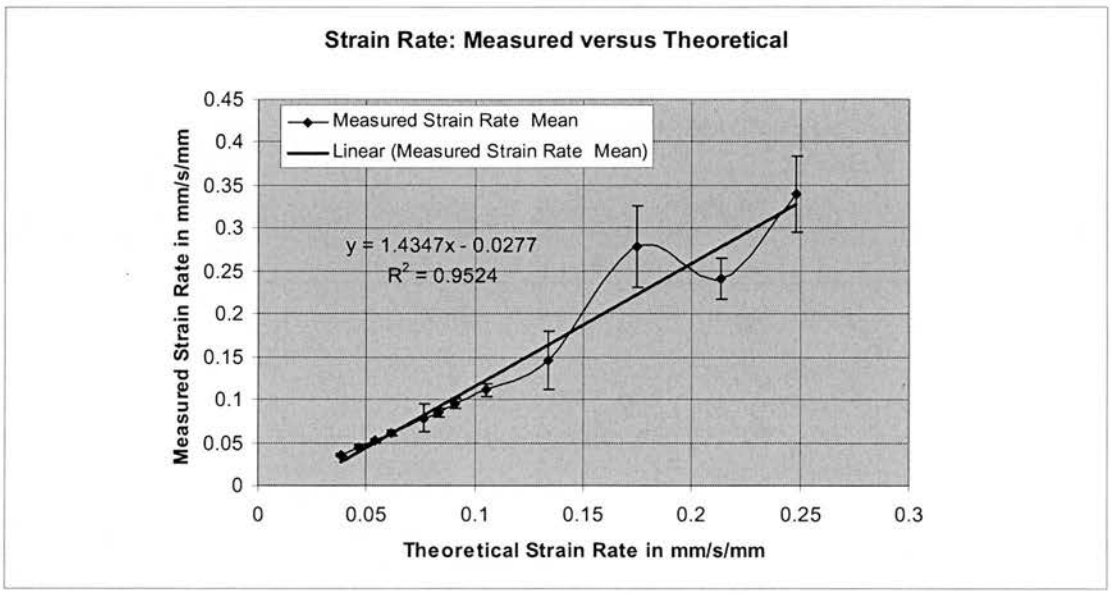

Figure 5-6: Measured one-component strain rate versus calculated

In **figure 5-7**, dynamic strain rates are used (Phantom with motion curve of **figure 5-8**) for the same evaluation. This good performance (accuracy ~5%) also leads to satisfactory quantification of dynamic strain rate. It is proposed that these measurements and their colour representation will allow acceptable quantitative strain rate characterization. The variation of standard deviation and bias are due to variation of the velocity estimate accuracy. Indeed the velocity can be encoded from 6 to 8 bits depending on the PRF, the maximum tissue ROI (region of interest) depth, and ensemble length. The inconsistence of the bias and the standard deviation in **figure 5-7** is due to the fact that the acquisition settings are different when the ensemble length is changed (MIN=2, MED=3, HIGH=4, MAX=5). Therefore the frame rate is different for each setting. The displacement applied to the phantom is a non linear curve c.f. **figure 5-8** and the change of the frame rate will generate strain

rate changes appearing within on acquired frame making the standard deviation and bias bigger. However the bias and standard deviation are still very low (less than 10%) even with a dynamic strain rate.

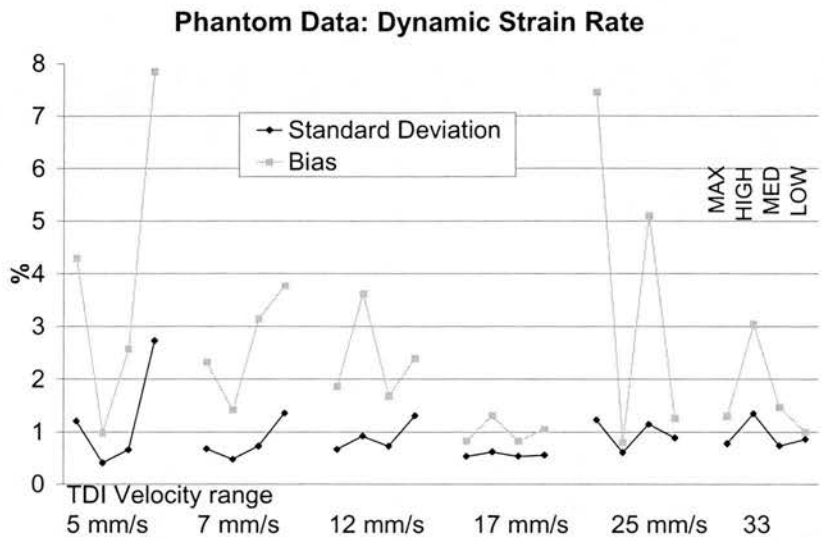

Figure 5-7: Standard Deviation and Bias of Dynamic Strain Rate estimation. MAX, HIGH, MED, LOW represents the ensemble length used to acquire the TDI information. MAX, HIGH, MED and LOW represents respectively ensemble lengths of 5, 4, 3 and 2.

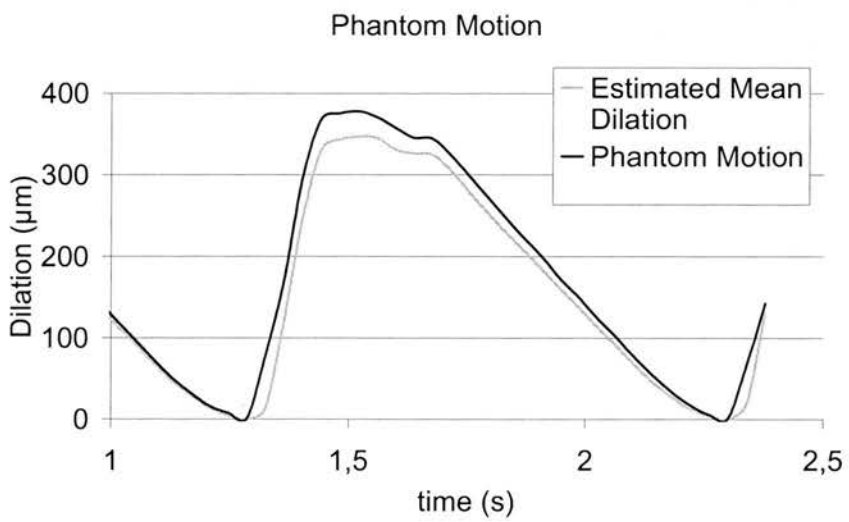

Figure 5-8: Simulated and Estimated Dilation curves.

5.7. Bias of the one-component strain rate estimator and correction

In this section a technique is proposed to correct for some of the limitations of one-component strain rate. It will be shown that if the strain rate is measured along the direction of deformation, part of the one-component strain rate bias can be corrected. The following figure illustrates a one-dimensional deformation with a TDI acquisition. The deformation or motion direction is not parallel to the direction of the ultrasound beams and an angle θ defines the angle between the two directions.

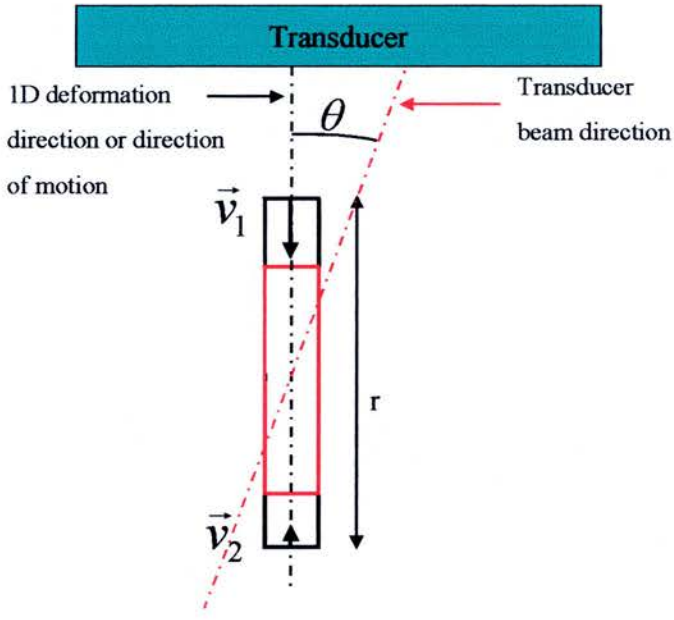

Figure 5-9: Deformation (strain of a one-dimensional object is limited to lengthening or shortening). Geometry of one-component strain with ultrasound acquisition.

The theoretical strain rate is defined by:

$$SR_{theoretical} = \frac{|\vec{v}_1| - |\vec{v}_2|}{r} \qquad (5\text{-}19)$$

where $|\vec{v}_1|$ and $|\vec{v}_2|$ are the velocity magnitudes. Because of the Doppler angle dependence, only the projection of $\vec{v}_1$ and $\vec{v}_2$ along the ultrasound beam can be measured with TDI. The non-corrected one-dimensional strain rate, called $SR_{noncorrected}$, is measured along the ultrasound beam as the following:

$$SR_{noncorrected} = \frac{|\vec{v}_1| \times \cos(\theta) - |\vec{v}_2| \times \cos(\theta)}{r/\cos(\theta)} = \frac{|\vec{v}_1| - |\vec{v}_2|}{r} \times (\cos(\theta))^2 \qquad (5\text{-}20)$$

In this method the velocities are underestimated but the length of the deformed object is overestimated, making the bias more important. Therefore measuring the strain rate information along the ultrasound beam introduces a bias defined by:

$$bias_{noncorrected} = \frac{SR_{noncorrected} - SR_{theoretical}}{SR_{theoretical}} = (\cos(\theta))^2 - 1 \qquad (5\text{-}21)$$

If now the direction of deformation is known and that the strain rate is calculated along this direction, the new one-component strain rate estimated called $SR_{corrected}$ is then defined by the following equation:

$$SR_{corrected} = \frac{|\vec{v}_1| \times \cos(\theta) - |\vec{v}_2| \times \cos(\theta)}{r} = \frac{|\vec{v}_1| - |\vec{v}_2|}{r} \times \cos(\theta) \qquad (5\text{-}22)$$

The corrected strain rate bias, called $bias_{corrected}$ is expressed as:

$$bias_{corrected} = \frac{SR_{corrected} - SR_{theoretical}}{SR_{theoretical}} = \cos(\theta) - 1 \qquad (5\text{-}23)$$

This latter bias is due to the fact that the velocity estimation is not corrected for its angle dependence. If we were to correct for the velocity angle (by assuming the velocity direction is parallel to the direction of deformation) then the strain rate estimation can be totally corrected.

The following figure illustrates the bias for both the non-corrected and corrected one-component strain rate as a function of angle between the deformation and the ultrasound beam.

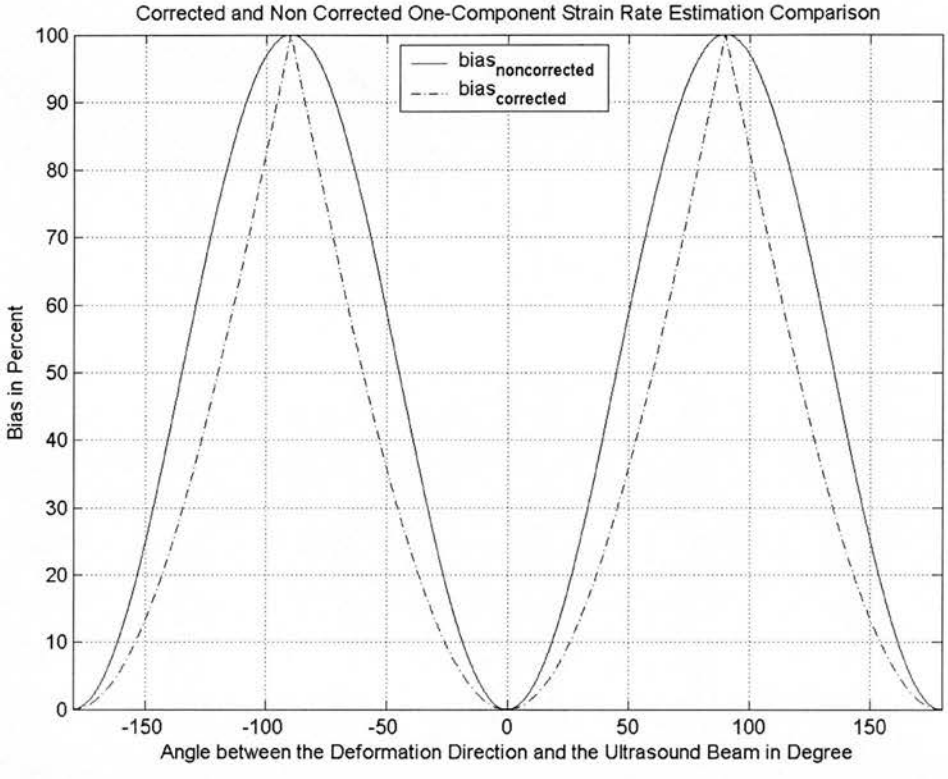

Figure 5-10: Comparison of non-corrected and corrected one-component strain rate absolute bias.

For example for angle θ equal to 20 degrees the corrected strain rate will be underestimated by 6 % and the uncorrected strain rate will be underestimated by 11.7 %. Globally the non-corrected estimation of strain rate is more underestimating the strain rate that the corrected estimation.

If the angle θ is equal to zero, the motion and deformation are both parallel to the ultrasound beam, the two estimations are equivalent, and the strain rate estimation has no bias.

To verify this theory an experiment has been performed using the setup showed in **figures 5-2**, **5-3** and **5-4**. Using a linear array transducer two acquisitions and three measurements are realized:

- The first one is a setup similar to the one described in section 5.6 where the acoustic beams used to acquire TDI are parallel to the piston displacement. Therefore the deformation is parallel to the acoustic beams. The strain rate is measured along the ultrasound beam and deformation direction (c.f. **figure 5-12-a**).
- The second one where the ultrasound beams are steered by 20 degrees from the perpendicular to the surface of the transducer. Therefore the deformation direction is tilted 20 degrees from the TDI acoustic beams. Two strain rate measurements are derived from this acquisition. One with the direction parallel to the TDI beams (**figure 5-12-c**) and one parallel to the deformation direction (**figure 5-12-b**).

Figure 5-11 illustrates the two types of acquisition described above.

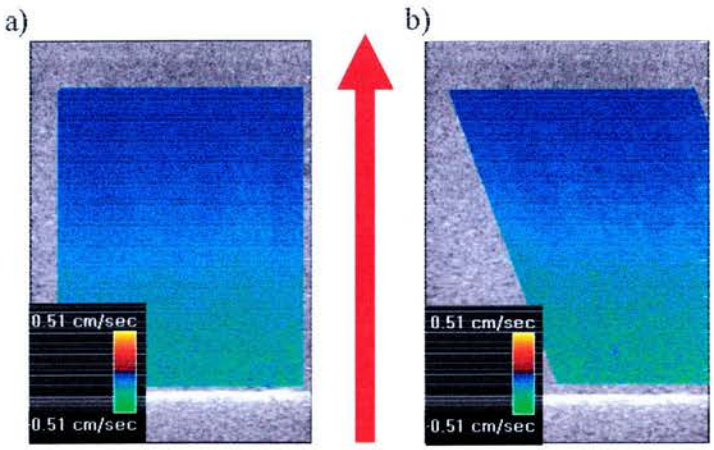

Figure 5-11: a) Straight acquisition of TDI with deformation direction parallel to the TDI ultrasound beam. b) Steered acquisition of TDI 20 degrees from the vertical. The red arrow represents the direction of deformation.

The displacement function of the piston is a saw function (which generates constant strain rates). A software package called QLab Strain Quantification (Philips Ultrasound, Bothell, WA, USA) has been developed to calculate strain rate. The author developed the algorithm and the code to calculate and display the strain rate information as a plugin to QLab. This package uses TDI velocity data collected from an ultrasound system, the HDI 5000 (Philips Ultrasound, Bothell, WA, USA) to derive the strain rate information (using equations 5-16 and 5-17). This software reconstructs a TDI velocity M-mode along a line defined by the user from the stack of two-dimensional velocity images collected from the ultrasound system. Then the software automatically derives the 1-D strain rate information along the M-line as a function of time and creates a "virtual" M-mode trace of the velocity and strain rate

along the direction of investigation (this software to derive strain rate information from Tissue Doppler information was written by the author in conjunction to a QLab software developer for the user interface). **Figure 5-12** illustrates how the user traces the M-line and **figure 5-13** shows the velocity and strain rate information derived from the M-line.

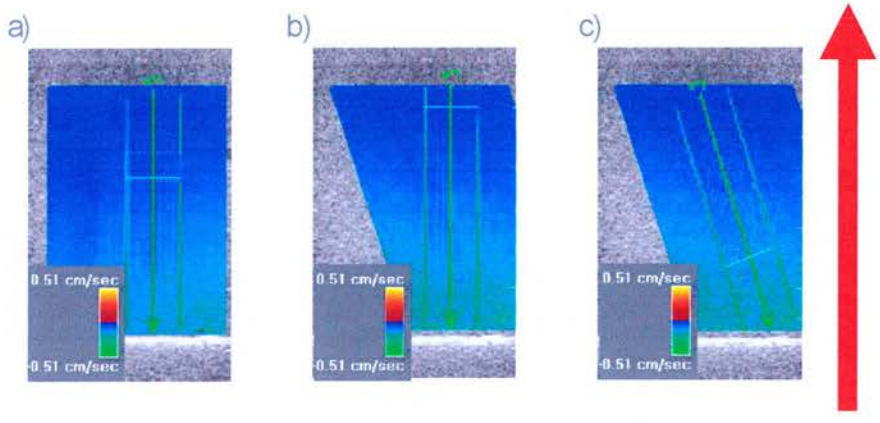

Figure 5-12: a) Straight acquisition of TDI and M-line (in green) with deformation direction parallel to the TDI ultrasound beam. b) Steered acquisition of TDI, 20 degrees from the vertical with a straight M-line. c) Steered TDI acquisition and steered M-line. The red arrow represents the direction of deformation.

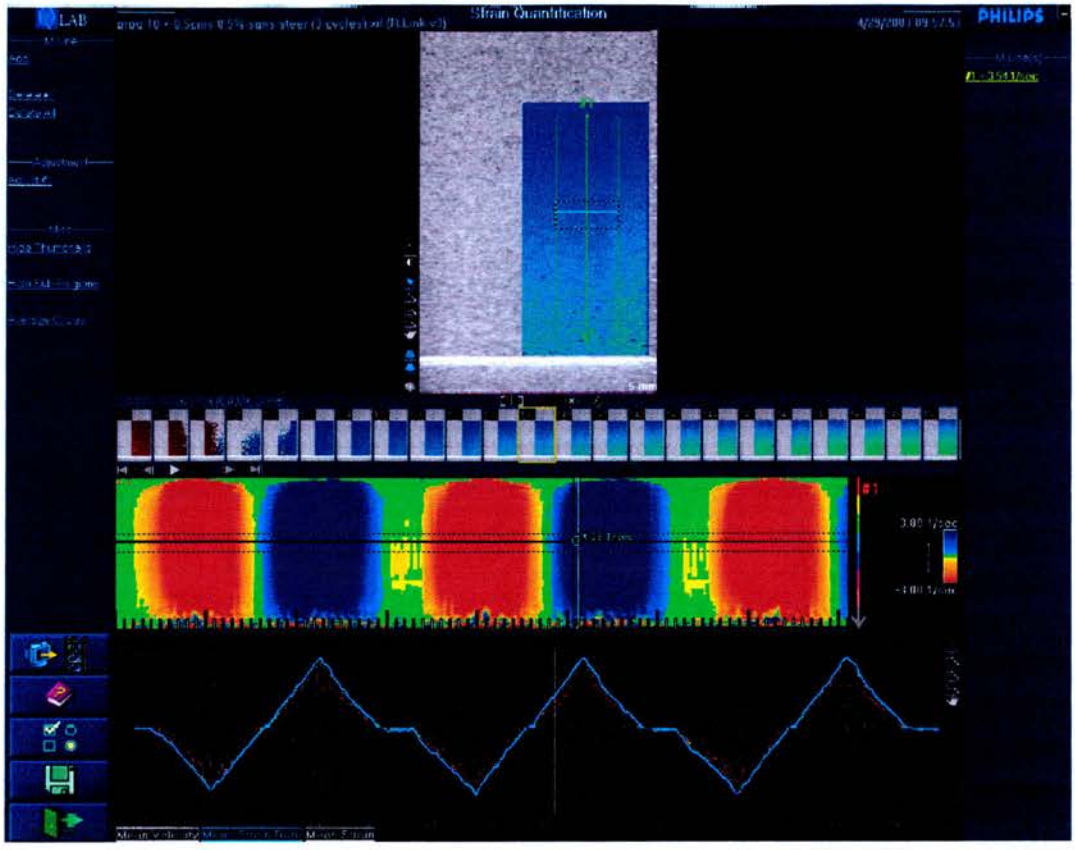

Figure 5-13: Two-dimensional TDI cineloop with the M-line with one-component strain rate m-mode and the mean strain rate graph below.

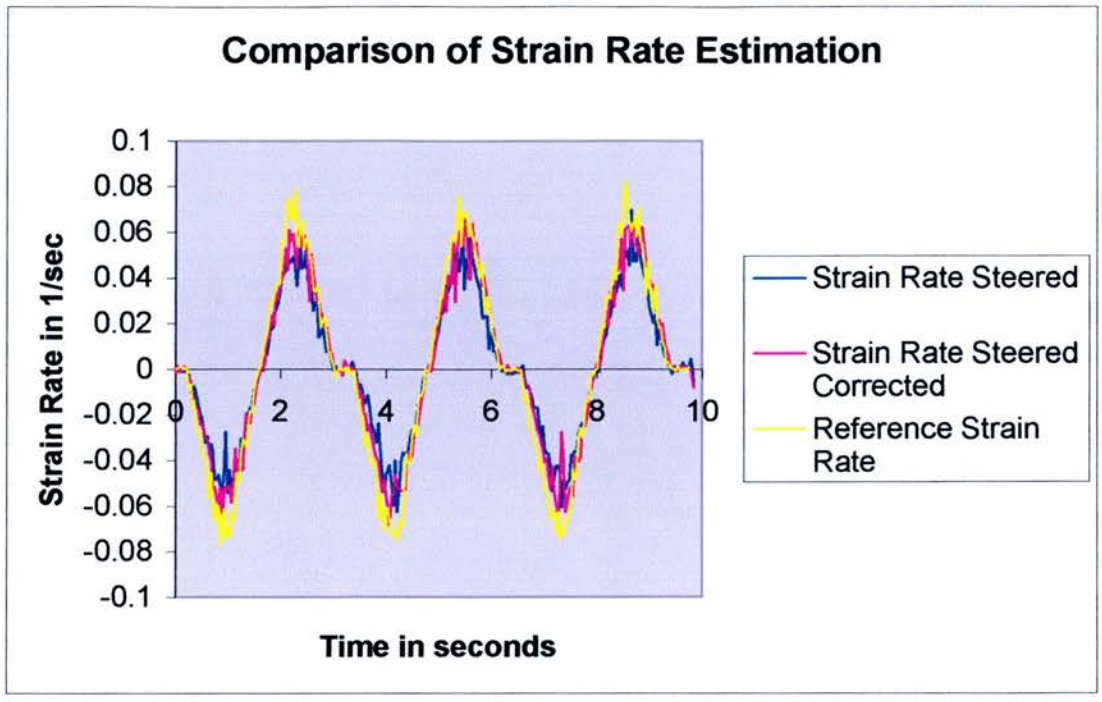

Figure 5-14: Yellow graph: Reference strain rate acquired with straight acquisition of TDI and M-line with deformation direction parallel to the TDI ultrasound beam. Pink graph: Corrected strain rate derived from a steered acquisition of TDI, 20 degrees from the vertical with a straight M-line. Dark blue graph: Steered TDI acquisition and steered M-line at 20 degrees.

Figure 5-14 represents the strain rate obtained in the 3 different configurations shown in **figure 5-12**. It can be seen that the corrected strain rate (pink trace) is closer to the reference strain rate (yellow curve) than the steered strain rate (blue line). The mean bias for the corrected estimator is -13% and for the non-corrected the value is -28 %, which validates the theory that one-component strain rate can be corrected by using the direction of deformation.

5.8. Clinical Example

Figure 5-15 presents examples of TDI and strain rate M-modes derived from TDI information. On the TDI display, blue shades represent tissue moving away from the

transducer and red colours represent motion towards the transducer. On the strain rate display, the blue colours represent dilation of the cardiac muscle and the red colours, compression. TDI and strain rate information presents a cyclic variation that can be divided into three main phases in the cardiac cycle: atrial filling (AF), systole (S), and early filling (EF). During the AF phase, the atria contract to eject blood in the ventricles through the mitral and tricuspid valves (the atrial septum is encoded in red colour).

During systole the ventricles are contracting (red) to eject blood in the aorta and in the pulmonary arteries. The systolic phase is followed by early filling where the ventricles are rapidly relaxing (expansion in blue) creating a differential pressure between the ventricles and the atria. This differential pressure pushes the mitral and tricuspid valves open and then allows the blood to flow from the atria into the ventricles.

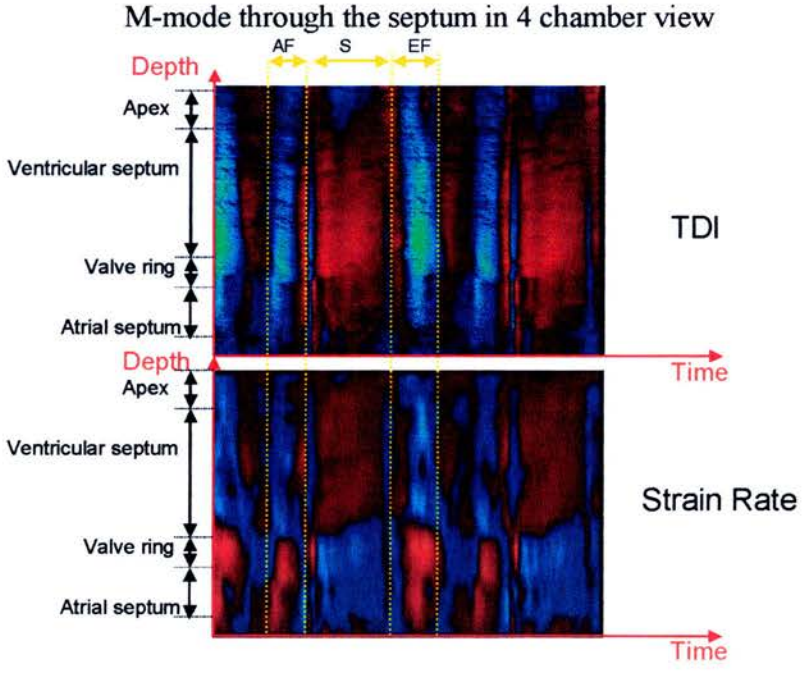

Figure 5-15: TDI and strain rate of the ventricular in a parasternal apical view of the heart.

The corrected strain rate imaging technique could be especially useful in cardiac applications where different deformation direction can be observed (longitudinal and circumferential shortening) in the same two-dimensional image. Future clinical implementation will involve the operator tracing a curved M-line along the myocardium along the wall in the apical 4-chamber view to assess the longitudinal deformation of the left ventricle (c.f. **figures 5-16** and **5-17**).

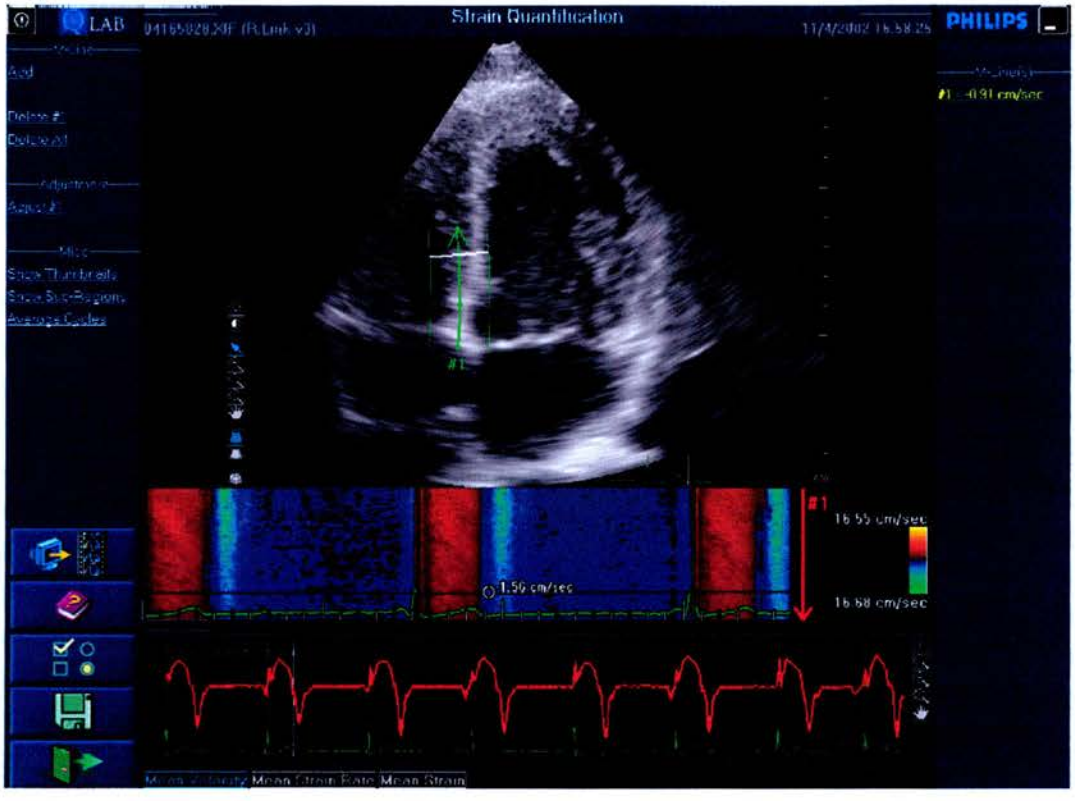

Figure 5-16: TDI of the heart left ventricle in a 4-chamber apical view, with a "virtual" TDI M-mode trace and a mean velocity trace below.

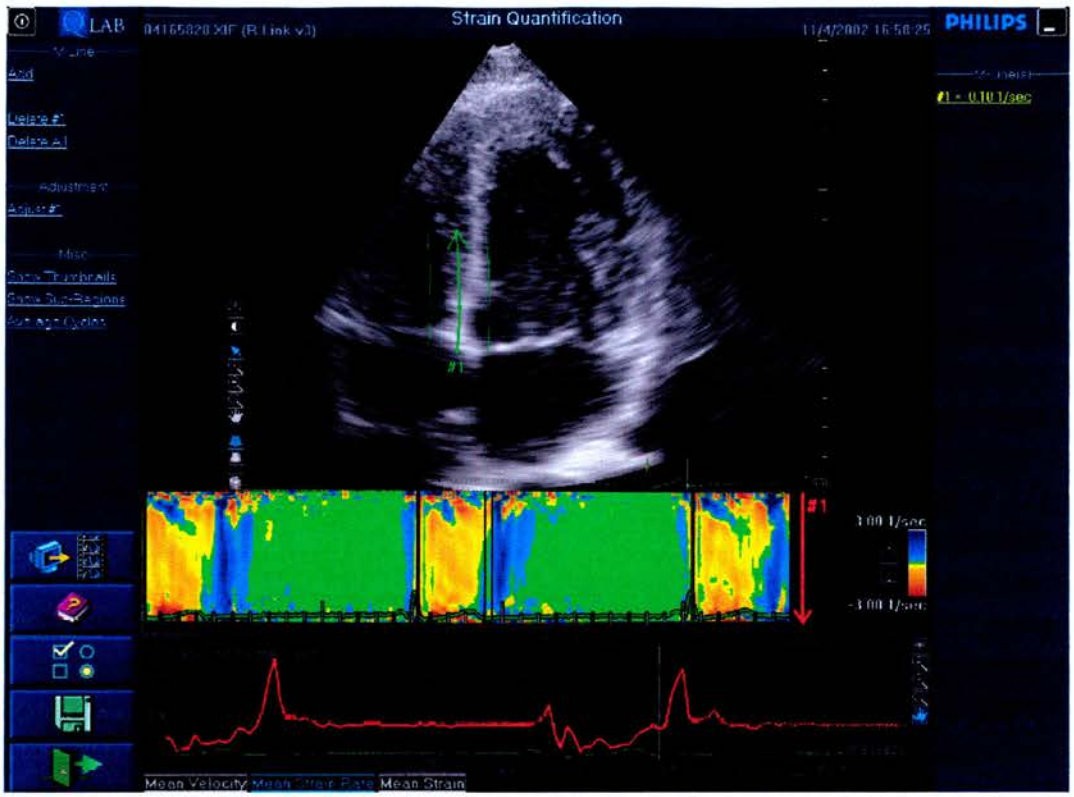

Figure 5-17: TDI of the heart left ventricle in a 4-chamber apical view, with a "virtual" strain M-mode trace and a mean strain trace below.

5.9. Conclusion

This technical validation step was essential for the evaluation of 1-C strain rate as a clinical parameter. From the results presented in this section, it can be seen that strain rate imaging can be considered as quantitative (bias less than 5% with a standard deviation less than 10%). When the strain rate is corrected by using the direction of deformation the error due to angle dependency is also reduced. This technique is particularly useful for cardiac applications where different deformation direction can be observed. The correction of the strain rate in cardiology application is especially

important due to the fact that the transducers used in these applications have very small apertures it is difficult to assess the velocity angle with a Doppler technique. Future work should consist of a large-scale clinical validation of these measurements.

6. Real Time Multi-Component Strain Rate

6.1. Introduction

The previous chapter presented a technique to assess the deformation along one direction and the possibility to correct for the Doppler angle dependence bias. However this correction can only be made by a visual assessment of the deformation direction. This problem can also be partially corrected by making sure the insonification is either parallel to the displacement direction during acquisition of the data sets. However the deformation of incompressible three-dimensional objects occurs in three dimensions (Aris 1962; Kundu 1990). Since the vessel walls and the heart can only be viewed from a limited number of views, and since the direction of motion varies throughout the cardiac cycle (Henson, Song et al. 2000; O'Dell, McCulloch et al. 2000; Kuijer, Marcus et al. 2002; Hu, Metaxas et al. 2003), not all strain rate components can be assessed using only one-component velocity acquisition.

To overcome these problems the following section describes a multi-component strain rate approach based on the vector Doppler velocity estimation developed in chapters 3 and 4.

This chapter is organized as follows: in section 6-2, the definition of three-dimension strain and strain rate tensor is provided; in section 6-3 a new autocorrelation based estimator for three-component strain rate is described; in section 6-4, a qualitative phantom validation of the method for the two-dimensional case is presented.

6.2. Three-Component Strain and Strain Rate Tensor

6.2.1. Strain Tensor

As seen in the previous chapter, one-component strain S_x can be described as the variation of an object size along the direction of deformation (c.f. **figure 6-1** and equation 6-1).

$$S_x = \frac{\delta u_x}{\delta x} \tag{6-1}$$

where u_x is the size of the deformed object along the x-axis.

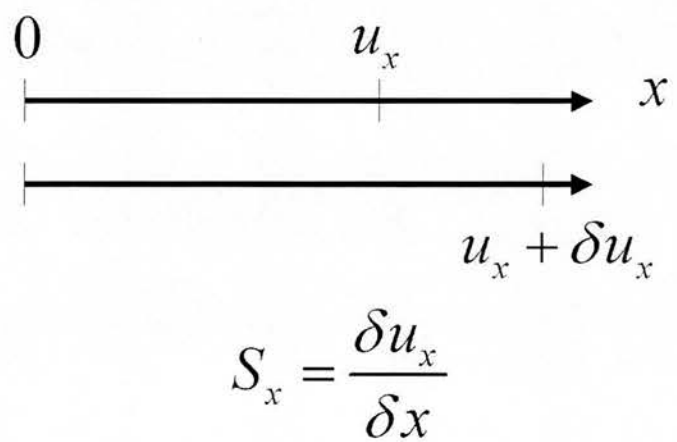

Figure 6-1: One-component strain along axis x. u_x represents the object size along the x-axis.

This approach can be extended to two dimensions and is illustrated **figure 6-2**.

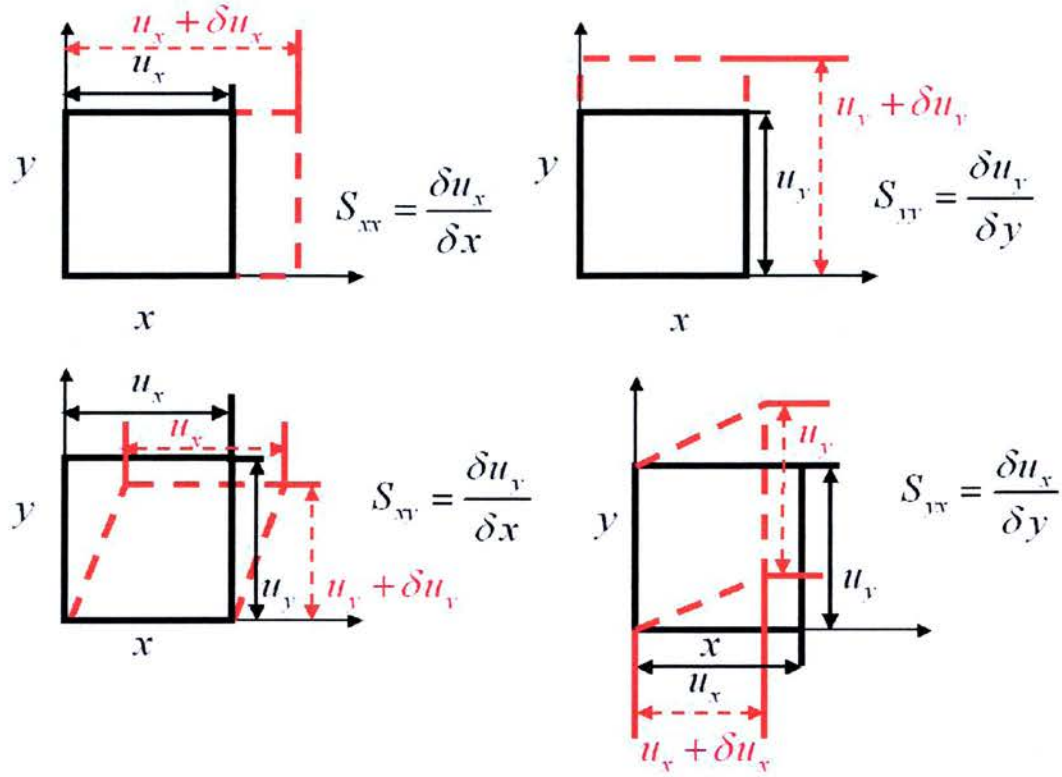

Figure 6-2: Strain tensor in two dimensions. Above are the two normal strains along the x- and y-axis. Below are the two shear strain components, movement of the borders relative to each other. u_x, u_y, and u_z represent the object sizes respectively along the x-axis, y-axis and z-axis.

Thus, in two dimensions, the strain becomes a tensor and has four components. Two components describe the deformations parallel to the displacement direction, along the x- and y-axis, respectively s_{xx} and s_{yy}:

$$s_{xx} = \frac{\delta u_x}{\delta x}$$
$$s_{yy} = \frac{\delta u_y}{\delta y} \qquad (6\text{-}2)$$

where u_x, u_y represent the object sizes respectively along the x-axis and y-axis. The other two components, s_{xy} and s_{yx}, are the shear components, which represent the deformation perpendicular to the main motion direction:

$$s_{xy} = \frac{\delta u_x}{\delta y}$$
$$s_{yx} = \frac{\delta u_y}{\delta x} \tag{6-3}$$

Shear strain components are characterized by the fact that the deformation occurring is appearing in the direction perpendicular to the direction of displacement, while for strain components, the deformation occurs in the direction of displacement.

The whole strain tensor, S, in the two-dimension case can be written as a matrix:

$$S = \begin{pmatrix} s_{xx} & s_{xy} \\ s_{yx} & s_{yy} \end{pmatrix} = \begin{pmatrix} \frac{\delta u_x}{\delta x} & \frac{\delta u_y}{\delta x} \\ \frac{\delta u_x}{\delta y} & \frac{\delta u_y}{\delta y} \end{pmatrix} \tag{6-4}$$

In three dimensions the tensor is extended to 9 components: 3 components along the main axis (on the diagonal of the tensor) and 6 shear strain components:

$$S = \begin{pmatrix} s_{xx} & s_{xy} & s_{xz} \\ s_{yx} & s_{yy} & s_{yz} \\ s_{zx} & s_{zy} & s_{zz} \end{pmatrix} = \begin{pmatrix} \frac{\delta u_x}{\delta x} & \frac{\delta u_y}{\delta x} & \frac{\delta u_z}{\delta x} \\ \frac{\delta u_x}{\delta y} & \frac{\delta u_y}{\delta y} & \frac{\delta u_z}{\delta y} \\ \frac{\delta u_x}{\delta z} & \frac{\delta u_y}{\delta z} & \frac{\delta u_z}{\delta z} \end{pmatrix} \tag{6-5}$$

The strain tensor is a symmetrical tensor. Therefore the following equation can be written:

$$\frac{\delta u_i}{\delta j} = \frac{\delta u_j}{\delta i} \tag{6-6}$$

where i and j are equal to x, y, or z. The strain components, s_{ij} can be written as the following:

$$s_{ij} = s_{ji} = \frac{1}{2}\left(\frac{\delta u_i}{\delta j} + \frac{\delta u_j}{\delta i}\right) \qquad (6\text{-}7)$$

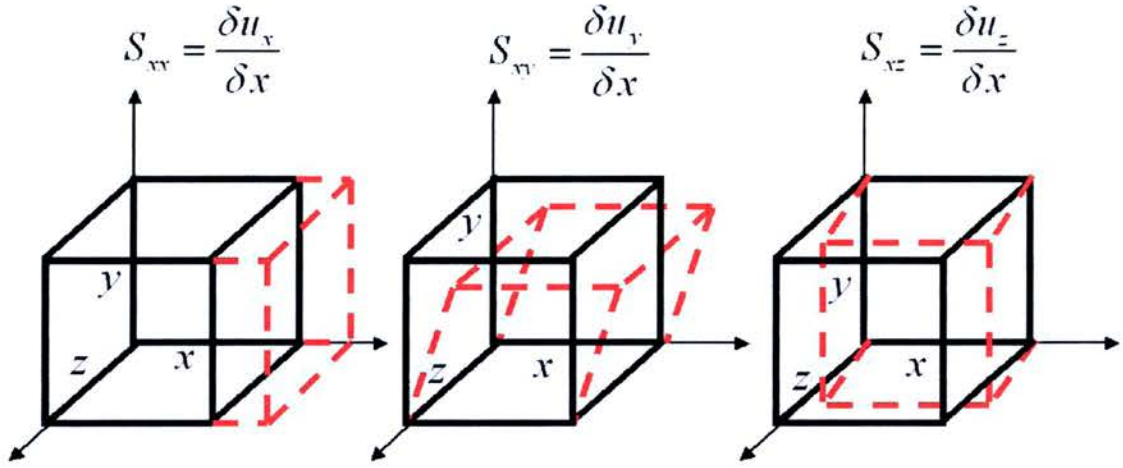

Figure 6-3: Strain tensor in three dimensions. Only the three strain components along the x-axis (one normal, two shear) are shown, but the y and z strains will be exactly the same and can be imagined by rotating the x images

Figure 6-3 illustrates three-dimension strain tensor. In **figure 6-3**, only the three deformation components along the x-axis (one normal, two shear) are shown, but the y and z strain components can be imagined by rotating the images.

6.2.2. Strain Rate Tensor

For small strains (linear deformation), small displacements, and displacement gradients, the strain rate tensor is equivalent to the time derivative of the strain tensor:

$$SR = \frac{\delta S}{\delta t} \tag{6-8}$$

To describe motion, the rate of deformation tensor or strain rate is commonly used and the components can be described as a function of the deformed object velocities:

$$\begin{aligned} sr_{ij} &= \frac{\delta s_{ij}}{\delta t} = \frac{\delta}{\delta t}\left(\frac{1}{2}\left(\frac{\delta u_i}{\delta j} + \frac{\delta u_j}{\delta i}\right)\right) \\ &= \frac{1}{2}\left(\frac{\delta}{\delta j}\left(\frac{\delta u_i}{\delta t}\right) + \frac{\delta}{\delta i}\left(\frac{\delta u_j}{\delta t}\right)\right) = \frac{1}{2}\left(\frac{\delta v_i}{\delta j} + \frac{\delta v_j}{\delta i}\right) \end{aligned} \tag{6-9}$$

Where i and j represent the different spatial axis x, y, z and v_i is the velocity projection along spatial axis i. Note, that the strain rate tensor can be derived from the instantaneous velocity field, which can be measured by ultrasound vector Doppler techniques (c.f. chapters 3 and 4).

Similarly to the strain tensor components, shear strain rate components are characterized by the fact that the deformation occurring is in the plane perpendicular to the direction of velocity, while for strain components, the deformation occurs in the direction of velocity.

6.3. Three-Component Strain Rate Estimator

In this section a method for calculating the strain rate tensor from three-component vector velocity is presented (this technique assumes that a three-component velocity estimate has been collected).

As seen above for small strains (linear deformation), small displacements and displacement gradients, the strain rate matrix sr_{ik} -element can be defined as:

$$sr_{ij}(t) = \frac{1}{2}\left(\frac{\delta v_i(t)}{\delta j} + \frac{\delta v_j(t)}{\delta i}\right) \tag{6-10}$$

where v_j is the velocity projection along the j[th] axis.

Thus the strain rate components are represented by the coefficient with $i = j$ and the shear strain rate components by the coefficients with $i \neq j$. The strain rate correlation estimate $\hat{S}R_{ij}(...,i,...,j,...,t)$ can be defined from lag-one autocorrelation estimates $\hat{R}1$, with the following equation:

$$\hat{S}R_{ij}(...,i,...,j,...,t) = \sum_{d=-D/2}^{D/2}\left[\begin{array}{l}\hat{R}1_j(...,i+d\times\delta i,...,j,...,t) \\ \times\hat{R}1_j(...,i+(d+1)\times\delta i,...,j,...,t)^*\end{array}\right] \tag{6-11}$$

$$\hat{S}R_{ji}(...,i,...,j,...,t) = \sum_{d=-D/2}^{D/2}\left[\begin{array}{l}\hat{R}1_i(...,i,...,j+d\times\delta j,...,t) \\ \times\hat{R}1_i(...,i,...,j+(d+1)\times\delta j,...,t)^*\end{array}\right] \tag{6-12}$$

where j represents the j[th] axis, $\hat{R}1_i(j)$ is the lag-one autocorrelation estimate along the i-axis direction, $\hat{R}1_i(j)^*$ is the complex conjugate of $\hat{R}1_i(j)$, i=x, y, z, and j=x, y, z. Then the strain rate component can be deduced using the following equations:

$$SRPhase_{ik}(...,i,...,j,...,t) = \arctan\left(\frac{\mathrm{Im}\left[\hat{S}R_{ik}(...,i,...,j,...,t)\right]}{\mathrm{Re}\left[\hat{S}R_{ik}(...,i,...,j,...,t)\right]}\right) \tag{6-13}$$

$$SRPhase_{ki}(...,i,...,j,...,t) = \arctan\left(\frac{\mathrm{Im}\left[\hat{S}R_{ki}(...,i,...,j,...,t)\right]}{\mathrm{Re}\left[\hat{S}R_{ki}(...,i,...,j,...,t)\right]}\right) \tag{6-14}$$

$$sr_{ij}(...,i,...,j,...,t) = \frac{c \times PRF}{-8\pi \times f_0} \left[\begin{array}{l} \frac{1}{\delta i} SRPhase_{ij}(...,i,...,j,...,t) \\ + \frac{1}{\delta j} SRPhase_{ji}(...,i,...,j,...,t) \end{array} \right] \quad (6\text{-}15)$$

To increase the robustness of the technique and if it is assumed that the strain rate has a linear variation within the kernel size the strain rate correlation estimate can be averaged in a three-dimensional kernel.

6.4. Two-Component Strain Rate Validation

A HDI 5000 system (Philips Ultrasound, Bothell WA, USA) and a L12-5 linear transducer (5 to 10 MHz) are used to acquire the 8-bit echo and TDI 8-bit (acquired with a 7.5 MHz transmit frequency) data. A TDI vector Doppler has been developed and validated (c.f. chapter 4). This system is used to acquire two-component vector tissue velocity estimate.

6.4.1. Phantom Setup

An experimental setup has been built to qualitatively assess the two-component strain rate. This setup includes a flow phantom, a PC driven controller and a DC-motor applied to a fluid gear pump.

The tissue-mimicking flow phantom, with a straight tube, and the blood-mimicking fluid (BMF) have been described by Ramnarine et al. (Ramnarine, Nassiri et al. 1998; Teirlinck, Bezemer et al. 1998; Ramnarine, Anderson et al. 2001). Briefly the tissue mimicking (TMM) is agar-based with an attenuation of 0.5 ± 0.03 dB/cm/MHz from 3 to 10 MHz and an acoustic speed of 1541 ± 3 m/s at 20 degree Celsius. The BMF is driven by a computer-controlled gear pump, and is a suspension of 5 μm Orgasol particles in a mixture of water, glycerin, dextran and surfactant, having an

acoustic speed of 1548 ± 5 m/s. The TMM is cast around a rod. After the TMM has set the rod is removed by sliding it through the hole leaving a wall-less vessel lumen of 8 mm diameter. This phantom is used as a model for carotid application even though an 8-mm lumen is significantly larger than that of a typical internal carotid artery. This value is a compromise because phantoms are too fragile for narrower lumen size. The inlet length is greater than 20 cm and is sufficiently long to assume that any deformation due to cyclic BMF pressure variation is only in the plane perpendicular to the vessel axis in the middle of the phantom. The scan plane of the TDI acquisition is set to be perpendicular to the vessel axis.

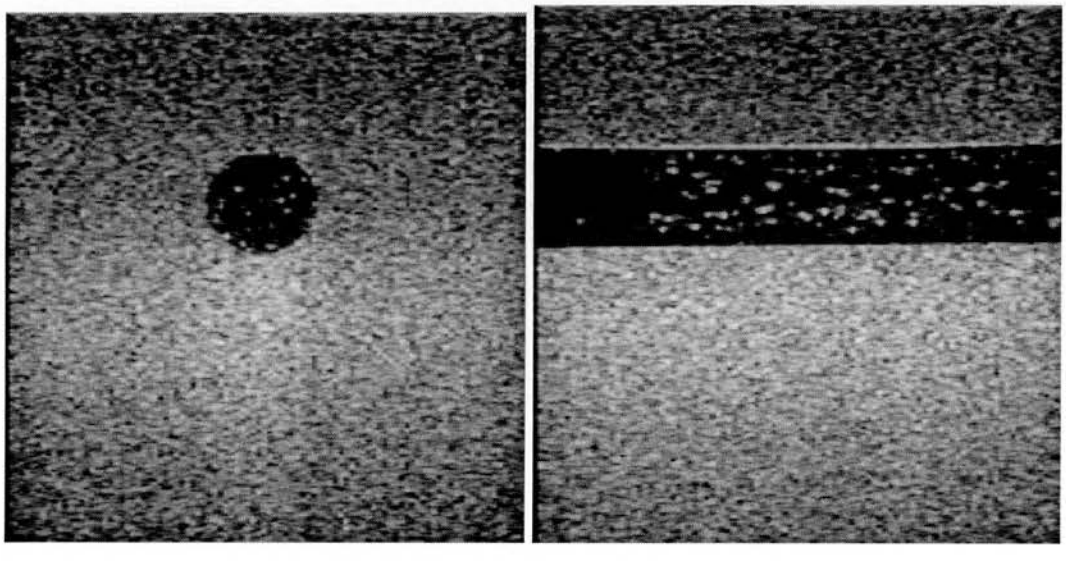

Figure 6-4: Transverse and longitudinal B-mode images of the wall less phantom.

6.4.2. Results of Validation

By applying a cyclic flow pressure variation (via a gear pump) in the flow phantom, a circumferential deformation is applied to the surrounding tissue mimicking. **Figure 6-5-a** illustrates for a circumferential dilation (positive flow pressure in the vessel

lumen) and **figure 6-5-b** a circumferential compression (negative flow pressure in the vessel lumen). Unfortunately since the phantom is cast in a tank the external walls are not free and the circumferential deformation is not uniform in the two-dimensional plane perpendicular to the vessel axis where the acquisition is made. Therefore this setup cannot be used for quantitative validation of two-component strain rate. However it can be used for qualitative assessment. **Figure 6-6** illustrates the deformation projections (axial and transverse) that should be observed when vessel lumen dilates.

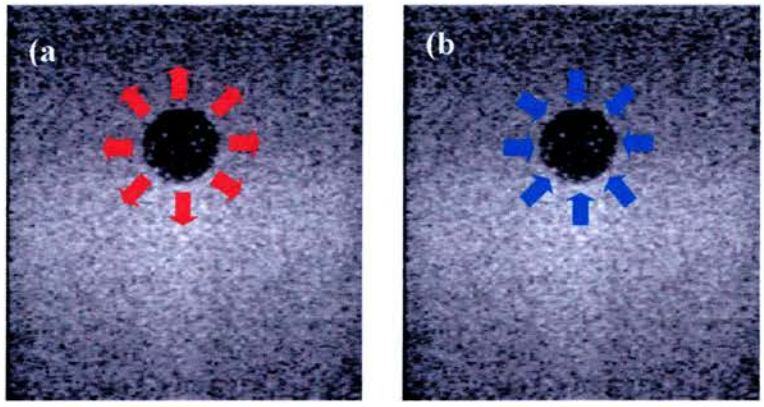

Figure 6-5: Short axis B-mode images of the wall less phantom. a) The red arrows represent the dilation deformation directions of the vessel wall when a positive flow pressure is applied in the vessel lumen. b) The blue arrows represent the compression deformation directions of the vessel wall when a negative flow pressure is applied in the vessel lumen.

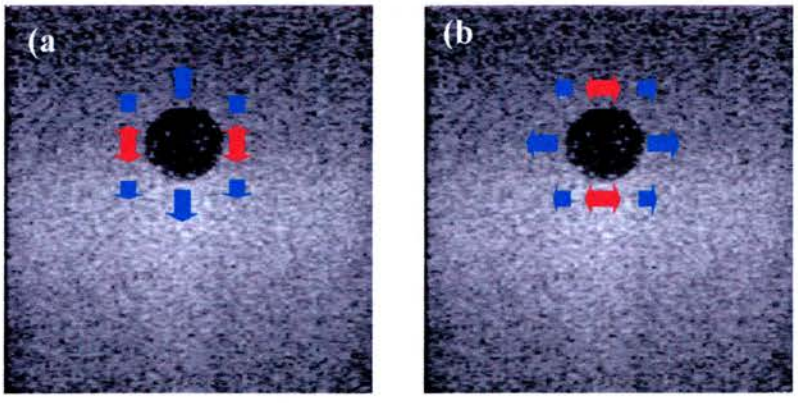

Figure 6-6: Vessel lumen dilating. The red arrows represent the dilation deformation and the blue arrows the compression deformation a) Axial deformation component. b) Tranverse deformation component.

Two-component vector velocity field from the moving tissue is acquired. A plugin quantification tool using HDI Lab (provided by Philips Ultrasound, Bothell, WA, USA) has been developed by the author to derive and display two-component strain rate images from two-component TDI velocity estimates based on equation 6-14 with D equal to 0.5 centimeters (the number of lateral and axial samples are automatically calculated from this kernel size). The images are showing agreement with the expected deformation patterns (c.f. **figure 6-7**).

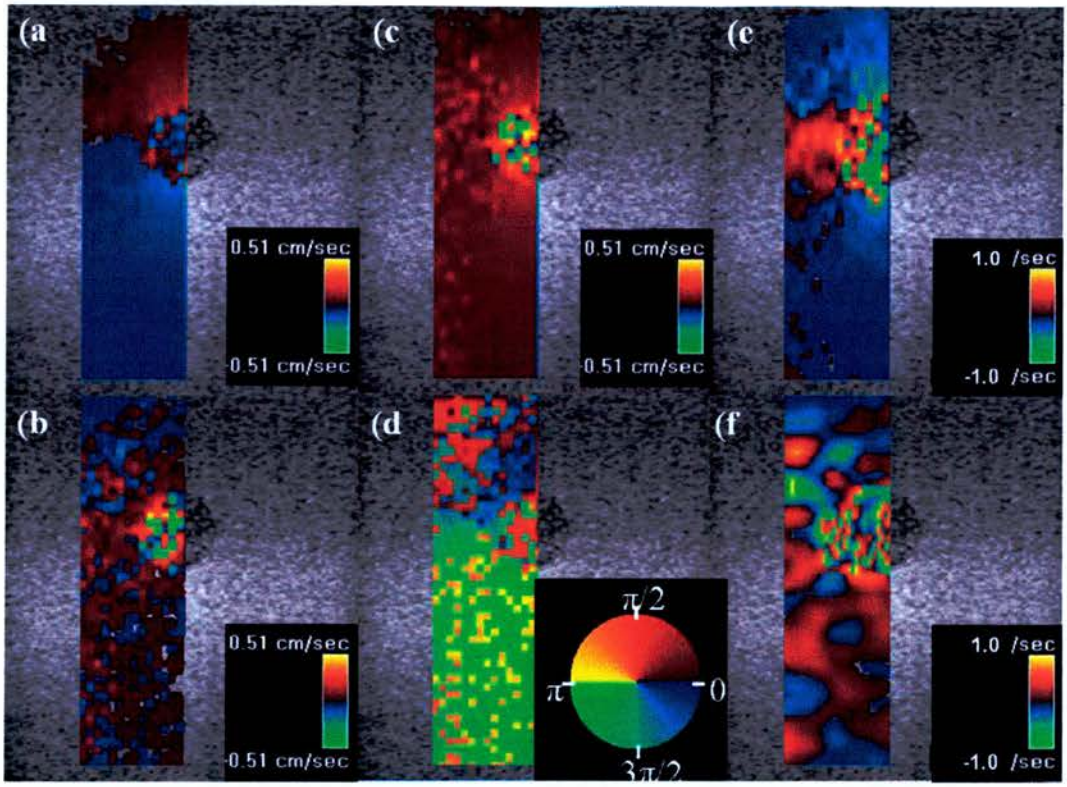

Figure 6-7: Transverse B-mode images of the wall less phantom during compression. a) Axial velocity component (red hues represent vertical motion toward the transducer and blue hues vertical motion away from the transducers). b) Transverse velocity component (red hues represent horizontal motion toward to the left and blue hues horizontal motion to the right). c) Absolute velocity magnitude (the brighter hues represent the highest absolute velocities). d) Velocity orientation. e) Axial deformation dilation (red pixels represent dilation and blue pixels represent compression). f) Transverse deformation dilation (red pixels represent dilation and blue pixels represent compression).

Figure 6-7-a represents the axial velocity component where red hues represent vertical motion toward the transducer and blue hues vertical motion away from the transducers. **Figure 6-7-b** represents the transverse velocity component where red hues represent horizontal motion toward to the left and blue hues horizontal motion to the right. **Figure 6-7-c** represents the absolute velocity magnitude where the brighter hues represent the highest absolute velocities. Figure **6-7-d** represents the

velocity orientation. **Figure 6-7-e** represents axial deformation dilation where the red pixels represent dilation and blue pixels represent compression. **Figure 6-7-f** represents the transverse deformation dilation where red pixels represent dilation and blue pixels represent compression.

In **Figure 6-7-f,** the transverse deformation shows a lot of noise. This noise is due to the fact that fewer samples are used in the lateral dimension than in the axial dimension for the same kernel size in centimeter. The axial resolution (number of samples per centimeter) is higher than the lateral resolution (number of lines per centimeter transmitted in the 2D TDI). The number of axial samples is between 50 to 60 samples per centimeter and the number of line in the acquisition setting is 10 to 12 lines per centimeters. This noise is also linked to the fact that the lateral velocity estimate (c.f. **figure 6-7-b**) is noisier (more variance c.f. chapter 4) than the axial velocity estimate. To improve the lateral strain rate estimate a larger TDI box could be used with a higher lateral resolution (higher number of lines per centimeter).

Some of the lateral and axial strain rate estimations near the vessel wall are biased by the fact that there is no deformation in the vessel lumen. A better experiment setup would have been to use an experiment similar to the setup that was used in section 5.7 where steered TDI is used but the compression is still along the vertical axis of the agar phantom and collected vector Doppler TDI information to derive lateral and axial strain rates. However this experiment could have only assessed the axial and lateral deformations for one velocity orientation.

6.5. Conclusion

We have derived the full strain rate tensor from three-component vector velocity. A novel estimator has been also generated from autocorrelation method which allows

real time computation of axial strain rate. The technique has been qualitatively assessed on a flow phantom and showed good visual correlation. However this technique needs to be further validated *in vivo* with a more quantifiable phantom where known two-component deformation can be applied. A new technique based on speckle tracking has been published to estimate axial and lateral strain rate components (Kaluzynski, Chen et al. 2001; Langeland, D'Hooge et al. 2005). Some extension of this work could be the comparison of our Doppler based technique with the speckle tracking technique.

7. Conclusions and Future Directions

The goal of this thesis was to develop Doppler ultrasound based methods to detect and quantify tissue dynamic and biomechanics properties for cardiac and vascular applications.

The first aim of this dissertation was to overcome some of the Doppler technique angle limitation for tissue motion imaging. A new method was derived from multiple receive beams to assess two-component tissue motion. First a real time pulsed wave Doppler prototype was realized to understand the one-dimensional problem (chapter 3). This prototype showed that accurate measurements of two-component velocity vector could be made. This technique was expanded to two-dimension in the following chapter (chapter 4). A new algorithm was also derived to improve the reliability of the velocity and angle estimates. Heterodyning and conventional vector velocity algorithms were assessed. It was shown that conventional vector Doppler estimation was more precise and that reliable two-component vector velocity estimation can be achieved with a bias around 5% and an error of 10% in real time (Criton, Steel et al. 2002). Therefore dynamic properties of tissue can be quantified with this new technique. One direct application of this technique is Arterial Wall Motion (AWM) (Bonnefous, Montaudon et al. 1996; Bonnefous, Criton et al. 2000). AWM is a novel technique to assess dynamic properties of the artery and is based on one-component tissue velocity estimates. By getting the two-component vector velocity of moving tissue more accurate estimation of the arterial wall displacements could be achieved.

The second goal of this research work was to assess deformation capabilities of tissue. A new technique was generated to assess self-induced deformation of the

myocardium. To measure the deformation, a one-component strain rate imaging technique was developed. A new algorithm estimation, derived from velocity information for real time implementation in an ultrasound scanner, was tested *in vitro* and assessed *in vivo*. The *in vitro* experiments involved cyclic compressions of an agar-based tissue-mimicking phantom, and was used to validate the method. The results showed that strain rate could be used as a quantification tool for tissue deformation (with accuracy around 5%).

The last goal of this thesis was to correct for the angle bias in the strain rate estimation. The angle dependence of the one-component strain rate estimation was first assessed. A first method to estimate one-component strain rate in any direction in the two-dimensional image not necessarily along the ultrasound beam was developed. The method allowed correcting for the strain rate bias along any user-defined direction (except perpendicular to the ultrasound beam). An *in vitro* experiment was performed to validate this theory. This new technique was implemented on an offline quantification tool (QLab, Philips Ultrasound, Bothell, Wa, USA) and applied to *in-vivo* cardiac data.

In the following chapter a second method to correct for angle dependence was developed. The full strain rate tensor was derived from three-component vector velocity. A new estimator was also generated from autocorrelation method. This technique was qualitatively assessed *in vitro* using a flow phantom. By applying a cyclic flow pressure (via a gear pump) on the flow phantom a circumferential deformation was applied to the surrounding tissue mimicking. Two-component vector velocity from the moving tissue was acquired and two two-component strain

rate images were derived. The images showed agreement with the expected deformation pattern.

The use of strain rate imaging in the clinical setting needs further studies. Other suggestions to fully assess strain rate imaging technique is to acquire a three-dimensional three-component tissue vector velocity field to allow a full quantification of the strain rate and the shear strain rate in all parts of the left ventricle and the vessel wall. These could be achieved with two-dimensional arrays, which can acquire in real time volumes of data.

Further studies could be performed to compare multi-component strain rate obtained from Doppler based technique with technique based on speckle tracking (Kaluzynski, Chen et al. 2001; Langeland, D'Hooge et al. 2005) for different clinical applications. Speckle tracking techniques are less dependent on the aperture size than vector Doppler. Therefore cardiac applications, where the window of imaging is very small (due to small space between the ribs), speckle tracking techniques could be more appropriate than the vector technique, even though it might require more computation power and therefore might not be real time. For vessel wall applications, where large linear arrays can be used, Doppler based strain rate technique might be better suited. Vector Doppler technique also requires less computation power for real time implementation, which is crucial in a clinical context.

References

Alam, M. (1991). "The atrioventricular plane displacement as a means of evaluating left ventricular systolic function in acute myocardial infarction." Clin Cardiol **14**(7): 588-94.

Alam, M., G. Rosenhamer, et al. (1992). "Atrioventricular plane displacement and left ventricular function. Left atrioventricular plane displacement is related to both systolic and diastolic left ventricular performance in patients with chronic heart failure." J Am Soc Echocardiogr **5**(4): 427-33.

Anderson, M. E. (1997). "Spatial Quadrature: A Novel Technique for Multi-Dimensional Velocity Estimation." IEEE UFFC Proceedings **1**: 1233-1238.

Anderson, M. E. (1998). "Multi-Dimensional Velocity Estimation with Ultrasound Using Spatial Quadrature." IEEE Trans UFFC **45**(3): 852-861.

Anderson, M. E. (1998). "Real-Time Implementation of Lateral Estimation Using Spatial Quadrature." IEEE Trans UFFC **1**: 1483-1487.

Anderson, M. E. (2000). "A Heterodyning Demodulation Technique for Spatial Quadrature." IEEE UFFC Proceedings **1**: 1487-1490.

Anderson, M. E., L. N. Bohs, et al. (1999). "A Comparison of Flow Tracking Techniques: Spatial Quadrature with Phase-Sensitive Axial Demodulation versus Speckle Tracking." IEEE UFFC Proceedings **1**: 1471-1475.

Anderson, M. E. and R. F. Kerr (2001). "In Vivo Lateral Flow Estimation with Spatial Quadrature." IEEE UFFC Proceedings: 1445-49.

Angelsen, B. A. J. (2000). Ultrasound Imaging: Waves, Signals, and Signal Processing, Emantec.

Arbeille, P., M. H. Bouin-Pineau, et al. (1999). "Accuracy of the main Doppler methods for evaluating the degree of carotid stenoses (continuous wave, pulsed wave, and color Doppler)." Ultrasound Med Biol **25**(1): 65-73.

Aris, R. (1962). Vectors, Tensors and Basic Equations of Fluid Mechanics.

Armour, J. A. and W. C. Randall (1970). "Structural basis for cardiac function." Am J Physiol **218**(6): 1517-23.

Ashrafzadeh, A. R., K. J. Dormer, et al. (1989). "A two-dimensional Doppler ultrasonic probe for flow measurement." Biomed Instrum Technol **23**(4): 301-7.

Assmann, P. E., C. J. Slager, et al. (1988). "Two-dimensional echocardiographic analysis of the dynamic geometry of the left ventricle: the basis for an improved model of wall motion." J Am Soc Echocardiogr **1**(6): 393-405.

Bashford, G. R. and O. T. von Ramm (1995). "Speckle structure in three dimensions." J Acoust Soc Am **98**(1): 35-42.

Bassiouny, H. S., H. Davis, et al. (1989). "Critical carotid stenoses: morphologic and chemical similarity between symptomatic and asymptomatic plaques." J Vasc Surg **9**(2): 202-12.

Behar, V., D. Adam, et al. (2003). "A new method of ultrasound color flow mapping." Ultrasonics **41**(5): 385-95.

Bluth, E. I., A. T. Stavros, et al. (1988). "Carotid duplex sonography: a multicenter recommendation for standardized imaging and Doppler criteria." Radiographics **8**(3): 487-506.

Bonnefous, O. (1988). "Measurement Of the Complete (3D) Velocity Vector of Blood Flows." IEEE Trans UFFC: 795-799.

Bonnefous, O., A. Criton, et al. (2000). "New TDI Developments for Vascular and Cardiac Applications." IEEE UFFC Proceedings: 1285-1290.

Bonnefous, O., M. Montaudon, et al. (1996). "Non Invasive Echographic Techniques for Arterial Wall Characterization." Ultrasonics Symposium Proceedings.

Bonnefous, O., M. Montaudon, et al. (1996). "Non Invasive Echographic Techniques for Arterial Wall Characterization." IEEE UFFC Proceedings: 1059-1064.

Bonnefous, O. and P. Pesque (1986). "Time domain formulation of pulse-Doppler ultrasound and blood velocity estimation by cross correlation." Ultrason Imaging **8**(2): 73-85.

Buda, A. J., E. J. Delp, et al. (1983). "Automatic computer processing of digital 2-dimensional echocardiograms." Am J Cardiol **52**(3): 384-9.

Canny, J. (1986). "A Computational Approach to Edge Detection." IEEE Trans Pattern Anal. Machine Intelligence **8**: 670-698.

Caro, C. G., J. M. Fitz-Gerald, et al. (1971). "Atheroma: a new hypothesis. Atheroma and arterial wall shear. Observation, correlation and proposal of a shear dependent mass transfer mechanism for atherogenesis." Br Med J **2**(762): 651.

Cathignol, D., K. Dickerson, et al. (1994). "On the spectral properties of Doppler thread phantoms." Ultrasound Med Biol **20**(7): 601-10.

Censor, D. and V. L. Newhouse (1986). "Theory of Ultrasound Doppler-Spectra Velocimetry for Abitrary beam and Flow Configurations." IEEE UFFC Proceedings: 923-931.

Censor, D., V. L. Newhouse, et al. (1988). "Theory of ultrasound Doppler-spectra velocimetry for arbitrary beam and flow configurations." IEEE Trans Biomed Eng **35**(9): 740-51.

Chen, J. C., A. J. Salvian, et al. (1998). "Predictive ability of duplex ultrasonography for internal carotid artery stenosis of 70%-99%: a comparative study." Ann Vasc Surg **12**(3): 244-7.

Cloutier, G., K. K. Shung, et al. (1993). "Experimental Evaluation of Intrinsic and Nonstationary Ultrasonic Doppler Spectral Broadening in Steady and Pulsatile Flow Loop Models." IEEE Trans UFFC **40**(6): 786-795.

Criton, A., R. Steel, et al. (2002). "Real Time Vector Doppler for Tissue Motion." IEEE UFFC Proceedings: 1529-1534.

Derumeaux, G., R. Douillet, et al. (1999). "[Distinguishing between physiologic hypertrophy in athletes and primary hypertrophic cardiomyopathies. Importance of tissue color Doppler]." Arch Mal Coeur Vaiss **92**(2): 201-10.

D'Hooge, J., A. Heimdal, et al. (2000). "Regional strain and strain rate measurements by cardiac ultrasound: principles, implementation and limitations." Eur J Echocardiogr **1**(3): 154-70.

D'Hooge, J., E. Konofagou, et al. (2002). "Two-dimensional ultrasonic strain rate measurement of the human heart in vivo." IEEE Trans Ultrason Ferroelectr Freq Control **49**(2): 281-6.

Ding, Z., H. Zhu, et al. (2002). "Coronary artery dynamics in vivo." Ann Biomed Eng **30**(4): 419-29.

Dotti, D., R. Lombardi, et al. (1992). "Vectorial measurement of blood velocity by means of ultrasound." Med Biol Eng Comput **30**(2): 219-25.

Dunmire, B., K. W. Beach, et al. (2000). "Cross-beam vector Doppler ultrasound for angle-independent velocity measurements." Ultrasound Med Biol **26**(8): 1213-35.

Evans, D. H. and W. N. McDicken (2000). Doppler Ultrasound: Physics, Instrumental, and Clinical Applications, 2nd Edition, John Wiley & Sons; 2nd edition.

Fei, D. Y. and C. T. Fu (1999). "New method to obtain ultrasonic angle independent Doppler color images using a sector transducer." Ann Biomed Eng **27**(2): 187-93.

Fei, D. Y., C. T. Fu, et al. (1994). "Angle independent Doppler color imaging: determination of accuracy and a method of display." Ultrasound Med Biol **20**(2): 147-55.

Fei, D. Y., C. T. Fu, et al. (1995). "Computer implementation in the reconstruction of 2-D flow velocity fields in ultrasound Doppler color imaging." Comput Biol Med **25**(6): 495-503.

Fei, D. Y., D. D. Liu, et al. (1997). "Feasibility of angle independent Doppler color imaging for in vivo application: preliminary study on carotid arteries." Ultrasound Med Biol **23**(1): 59-67.

Friedland, N. and D. Adam (1989). "Automatic Ventricular Cavity Boundary Detection from Sequential Ultrasound Images using Simulated Anealing." IEEE Trans Medical Imaging **8**(4).

Galderisi, M., P. Caso, et al. (1999). "Myocardial diastolic impairment caused by left ventricular hypertrophy involves basal septum more than other walls: analysis by pulsed Doppler tissue imaging." J Hypertens **17**(5): 685-93.

Garcia, M. J., L. Rodriguez, et al. (1996). "Myocardial wall velocity assessment by pulsed Doppler tissue imaging: characteristic findings in normal subjects." Am Heart J **132**(3): 648-56.

Gardiner, W. M. and M. D. Fox (1989). "Color-flow US imaging through the analysis of speckle motion." Radiology **172**(3): 866-8.

Gehlbach, S. M. and R. E. Alvarez (1981). "Digital ultrasound imaging techniques using vector sampling and raster line reconstruction." Ultrason Imaging **3**(1): 83-107.

Geiser, E. A., D. A. Conetta, et al. (1990). "A second-generation computer-based edge detection algorithm for short-axis, two-dimensional echocardiographic images: accuracy and improvement in interobserver variability." J Am Soc Echocardiogr **3**(2): 79-90.

Geiser, E. A., L. H. Oliver, et al. (1988). "Clinical validation of an edge detection algorithm for two-dimensional echocardiographic short-axis images." J Am Soc Echocardiogr **1**(6): 410-21.

Giarre, M., B. Dousse, et al. (1996). "Velocity vector reconstruction for color flow Doppler: experimental evaluation of a new geometrical method." Ultrasound Med Biol **22**(1): 75-88.

Glagov, S. (1994). "Intimal hyperplasia, vascular modeling, and the restenosis problem." Circulation **89**(6): 2888-91.

Guidi, G., C. Licciardello, et al. (2000). "Intrinsic spectral broadening (ISB) in ultrasound Doppler as a combination of transit time and local geometrical broadening." Ultrasound Med Biol **26**(5): 853-62.

Hamilton, W. F. and J. H. Rompf (1932). "Movement of the base of the ventricle and the relative constancy of the cardiac volume." Am J Physiol **102**: 559-565.

Heimdal, A., A. Stoylen, et al. (1998). "Real-time strain rate imaging of the left ventricle by ultrasound." J Am Soc Echocardiogr **11**(11): 1013-9.

Hein, I. A. (1994). "Three-Dimensional Blood Flow Velocity Vector Estimation with a Triple-Beam Ultrasonic Lens." IEEE UFFC Proceedings: 1737-1742.

Hein, I. A. (1995). "Triple-Beam Lens Transducers for Three-Dimensional Ultrasonic Fluid Flow Estimation." IEEE Trans UFFC **42**(5): 854-869.

Hein, I. A. and W. D. O'Brien, Jr. (1993). "Current Time-Domain Methods for Assessing Tissue Motion by Analysis from Reflected Ultrasound Echoes-A Review." IEEE Trans UFFC **40**(4): 84-102.

Henson, R. E., S. K. Song, et al. (2000). "Left ventricular torsion is equal in mice and humans." Am J Physiol Heart Circ Physiol **278**(4): H1117-23.

Hofer, M., G. Rappitsch, et al. (1996). "Numerical study of wall mechanics and fluid dynamics in end-to-side anastomoses and correlation to intimal hyperplasia." J Biomech **29**(10): 1297-308.

Hoffman, E. A. and E. L. Ritman (1985). "Invariant total heart volume in the intact thorax. Shape and dimensions of cardiac chambers: importance of CT section thickness and orientation." Am J Physiol **249**(4 Pt 2): H883-90.

Horn, B. K. P. and B. G. Schunck (1981). "Determining Optical Flow." Artificial Intelligence: 17:185.

Hoskins, P. R. (1996). "Accuracy of maximum velocity estimates made using Doppler ultrasound systems." Br J Radiol **69**(818): 172-7.

Hoskins, P. R. (1997). "Peak velocity estimation in arterial stenosis models using colour vector Doppler." Ultrasound Med Biol **23**(6): 889-97.

Hoskins, P. R. (1999). "A comparison of single- and dual-beam methods for maximum velocity estimation." Ultrasound Med Biol **25**(4): 583-92.

Hoskins, P. R. (2002). "Ultrasound techniques for measurement of blood flow and tissue motion." Biorheology **39**(3-4): 451-9.

Hoskins, P. R., P. J. Fish, et al. (1999). "Finite beam-width ray model for geometric spectral broadening." Ultrasound Med Biol **25**(3): 391-404.

Hosono, M., Y. Nakano, et al. (1995). "Three-dimensional display of cardiac structures using reconstructed magnetic resonance imaging." J Digit Imaging **8**(3): 105-15.

Hu, Z., D. Metaxas, et al. (2003). "In vivo strain and stress estimation of the heart left and right ventricles from MRI images." Med Image Anal **7**(4): 435-44.

Jensen, J. A. (1993). "Implementation of ultrasound time-domain cross-correlation blood velocity estimators." IEEE Trans Biomed Eng **40**(5): 468-74.

Jensen, J. A. (2001). "A new estimator for vector velocity estimation." IEEE Trans Ultrason Ferroelectr Freq Control **48**(4): 886-94.

Jensen, J. A. (2001). "A New Estimator for Vector Velocity Estimation." IEEE Trans UFFC **48**(4): 886-894.

Jensen, J. A. (2003). "Directional velocity estimation using focusing along the flow direction. I: Theory and simulation." IEEE Trans Ultrason Ferroelectr Freq Control **50**(7): 857-72.

Jensen, J. A. and P. Munk (1998). "A New Method for Estimation of Velocity Vectors." IEEE Trans UFFC **45**(3): 837-851.

Jensen, J. A. and P. Munk (1998). "Performance of a Vector Velocity Estimator." IEEE UFFC Proceedings: 1489-1493.

Jensen, J. A. and P. Munk (1999). "An Improved Estimation and Focusing Scheme for Vector Velocity Estimation." IEEE UFFC Proceedings: 1465-1470.

Jensen, J. A. and N. B. Svendsen (1992). "Calculation of Pressure Fields from Arbitrarily Shaped, Apodized, and Excited Ultrasound Transducers." IEEE Trans UFFC **39**(2): 262-267.

Jmor, S., T. El-Atrozy, et al. (1999). "Grading internal carotid artery stenosis using B-mode ultrasound (in vivo study)." Eur J Vasc Endovasc Surg **18**(4): 315-22.

Jogestrand, T., M. Lindqvist, et al. (2002). "Diagnostic performance of duplex ultrasonography in the detection of high grade internal carotid artery stenosis." Eur J Vasc Endovasc Surg **23**(6): 510-8.

Kalman, P. G., K. W. Johnston, et al. (1985). "In vitro comparison of alternative methods for quantifying the severity of Doppler spectral broadening for the diagnosis of carotid arterial occlusive disease." Ultrasound Med Biol **11**(3): 435-40.

Kaluzynski, K., X. Chen, et al. (2001). "Strain rate imaging using two-dimensional speckle tracking." IEEE Trans Ultrason Ferroelectr Freq Control **48**(4): 1111-23.

Kanai, H., N. Chiubachi, et al. (1997). "Noninvasive Evaluation of Spatial Distribution of Thickness Change in Myocadium." IEEE Trans UFFC: 1177-1180.

Kasai, C., K. Namekawa, et al. (1985). "Real-Time Two-Dimensional Blood Flow Imaging Using and Autocorrelation Technique." IEEE Trans. Ultrasonics, Ferroelectrics and Frequency controls **SU-32**(3): 458-464.

Kassam, M. S., R. S. Cobbold, et al. (1982). "Method for estimating the Doppler mean velocity waveform." Ultrasound Med Biol **8**(5): 537-44.

Katz, W. E., V. K. Gulati, et al. (1997). "Quantitative evaluation of the segmental left ventricular response to dobutamine stress by tissue Doppler echocardiography." Am J Cardiol **79**(8): 1036-42.

Kohler, T. R. and A. Jawien (1992). "Flow affects development of intimal hyperplasia after arterial injury in rats." Arterioscler Thromb **12**(8): 963-71.

Ku, D. N., D. P. Giddens, et al. (1985). "Hemodynamics of the normal human carotid bifurcation: in vitro and in vivo studies." Ultrasound Med Biol **11**(1): 13-26.

Kuijer, J. P., J. T. Marcus, et al. (2002). "Three-dimensional myocardial strains at end-systole and during diastole in the left ventricle of normal humans." J Cardiovasc Magn Reson **4**(3): 341-51.

Kundu, P., K. (1990). Fluid Mechanics.

Lakatta, E. G. and D. Levy (2003). "Arterial and cardiac aging: major shareholders in cardiovascular disease enterprises: Part I: aging arteries: a "set up" for vascular disease." Circulation **107**(1): 139-46.

Langeland, S., J. D'Hooge, et al. (2005). "Experimental validation of a new ultrasound method for the simultaneous assessment of radial and longitudinal myocardial deformation independent of insonation angle." Circulation **112**(14): 2157-62.

Lee, B. R., H. K. Chiang, et al. (1999). "Implementation of spectral width Doppler in pulsatile flow measurements." Ultrasound Med Biol **25**(8): 1221-7.

Lee, B. R., H. K. Chiang, et al. (1999). "Doppler angle and flow velocity estimations using the classic and tranverse Doppler effects." IEEE Trans UFFC **46**(1): 252-256.

Li, P. C., C. J. Cheng, et al. (2001). "On velocity estimation using speckle decorrelation." IEEE Trans Ultrason Ferroelectr Freq Control **48**(4): 1084-91.

Liu, S. Q. (1999). "Biomechanical basis of vascular tissue engineering." Crit Rev Biomed Eng **27**(1-2): 75-148.

Liu, Y., Y. Lai, et al. (2001). "Pulsatile flow simulation in arterial vascular segments with intravascular ultrasound images." Med Eng Phys **23**(8): 583-95.

Lubinski, M. A., S. Y. Emelianov, et al. (1999). "Adaptive Strain Estimation Using Retrospective Processing." IEEE Trans UFFC **46**(1): 97-107.

Lubinski, M. A., S. Y. Emelianov, et al. (1999). "Speckle Tracking Methods for Ultrasonic Elasticity Imaging Using Short-Time Correlation." IEEE Trans UFFC.

Mailloux, G. E., M. Bertrand, et al. (1984). "Texture analysis of ultrasound B-mode images by segmentation." Ultrason Imaging **6**(3): 262-77.

Mailloux, G. E., A. Bleau, et al. (1987). "Computer analysis of heart motion from two-dimensional echocardiograms." IEEE Trans Biomed Eng **34**(5): 356-64.

Maniatis, T. A., R. S. Cobbold, et al. (1994). "Two-dimensional velocity reconstruction strategies for color flow Doppler ultrasound images." Ultrasound Med Biol **20**(2): 137-45.

Mankad, S., S. Murali, et al. (1999). "Evaluation of the potential role of color-coded tissue Doppler echocardiography in the detection of allograft rejection in heart transplant recipients." Am Heart J **138**(4 Pt 1): 721-30.

Maurice, R. L., J. Ohayon, et al. (2004). "Noninvasive vascular elastography: theoretical framework." IEEE Trans Med Imaging **23**(2): 164-80.

McArdle, A., V. L. Newhouse, et al. (1995). "Demonstration of Three-Dimensional Vector Flow Estimation Using Bandwidth and Two Transducers on a Flow Phantom." Ultrasound Med Biol **21**(5): 679-92.

McDicken, W. N., G. R. Sutherland, et al. (1992). "Colour Doppler velocity imaging of the myocardium." Ultrasound Med Biol **18**(6-7): 651-4.

Meunier, J., M. Bertrand, et al. (1988). "Local Myocardial Deformation Computed from Speckle Motion." Proc Compt. Cardiology: 133-136.

Morin, J. F., K. W. Johnston, et al. (1988). "Factors affecting the continuous wave Doppler spectrum for the diagnosis of carotid arterial disease." Ultrasound Med Biol **14**(3): 175-89.

Morsy, A. A. and O. T. Von Ramm (1998). "3D ultrasound tissue motion tracking using correlation search." Ultrason Imaging **20**(3): 151-9.

Munk, P. and J. A. Jensen (2000). "A new approach for the estimation of the axial velocity using ultrasound." Ultrasonics **37**(10): 661-5.

Newhouse, V. L., D. Censor, et al. (1987). "Ultrasound Doppler probing of flows transverse with respect to beam axis." IEEE Trans Biomed Eng **34**(10): 779-89.

Newhouse, V. L., K. Dickerson, et al. (1994). "Three-Dimensional Vector Flow Estimation Using Two Transducers and Spectral Width." IEEE Trans UFFC **41**(1): 90-95.

Newhouse, V. L., E. S. Furgason, et al. (1980). "The Dependence of Ultrasound Doppler Bandwidth on Beam Geometry." IEEE Trans UFFC **27**(2): 50-59.

Newhouse, V. L., P. LeCong, et al. (1980). "On increasing the range of pulsed Doppler systems for blood flow measurement." Ultrasound Med Biol **6**(3): 233-7.

Newhouse, V. L. and J. Reid (1990). "Invariance of Doppler Bandwidth with Flow Axis Displacement." IEEE UFFC Proceedings: 1533-1536.

Newhouse, V. L. and J. Reid (1991). "Invariance of the Doppler bandwidth with flow displacement in the illuminating field." J Acoust Soc Am **90**(5): 2595-601.

Newhouse, V. L., L. W. Varner, et al. (1977). "Geometrical spectrum broadening in ultrasonic Doppler systems." IEEE Trans Biomed Eng **24**(5): 478-80.

O'Boyle, J. E., A. F. Parisi, et al. (1983). "Quantitative detection of regional left ventricular contraction abnormalities by 2-dimensional echocardiography. Comparison of myocardial thickening and thinning and endocardial motion in a canine model." Am J Cardiol **51**(10): 1732-8.

O'Dell, W. G. and A. D. McCulloch (2000). "Imaging three-dimensional cardiac function." Annu Rev Biomed Eng **2**: 431-56.

O'Dell, W. G., A. D. McCulloch, et al. (2000). "Imaging three-dimensional cardiac function. Functional evaluation of the heart with magnetic resonance imaging." Annu Rev Biomed Eng **2**(6): 431-56.

Overbeck, J. R., K. W. Beach, et al. (1992). "Vector Doppler: accurate measurement of blood velocity in two dimensions." Ultrasound Med Biol **18**(1): 19-31.

Papademetris, X., A. J. Sinusas, et al. (2001). "Estimation of 3D left ventricular deformation from echocardiography." Med Image Anal **5**(1): 17-28.

Pasquet, A., G. Armstrong, et al. (2000). "Correlation of myocardial Doppler velocity response to exercise with independent evidence of myocardial ischemia by dual-isotope single-photon emission computed tomography." Am J Cardiol **85**(5): 536-42.

Perktold, K. and G. Rappitsch (1995). "Computer simulation of local blood flow and vessel mechanics in a compliant carotid artery bifurcation model." J Biomech **28**(7): 845-56.

Phillips, P. J., A. P. Kadi, et al. (1995). "Feasibility study for a two-dimensional diagnostic ultrasound velocity mapping system." Ultrasound Med Biol **21**(2): 217-29.

Powalowski (1988). "Ultrasonic System for Non Invasive Measurement of Hemodynamic Parameters of Human Arterial Vascular System." Archives of Acoustics **13**(1-2): 89-108.

Ramnarine, K. V., T. Anderson, et al. (2001). "Construction and geometric stability of physiological flow rate wall-less stenosis phantoms." Ultrasound Med Biol **27**(2): 245-50.

Ramnarine, K. V., D. K. Nassiri, et al. (1998). "Validation of a new blood-mimicking fluid for use in Doppler flow test objects." Ultrasound Med Biol **24**(3): 451-9.

Richardson, P. D. (2002). "Biomechanics of plaque rupture: progress, problems, and new frontiers." Ann Biomed Eng **30**(4): 524-36.

Robinson, M. L., D. Sacks, et al. (1988). "Diagnostic criteria for carotid duplex sonography." AJR Am J Roentgenol **151**(5): 1045-9.

Routh, H. F., T. L. Pusateri, et al. (1990). "Preliminary Studies into High Velocity Transverse Blood Flow Measurement." IEEE UFFC Proceedings.

Ryan, L. K. and F. S. Foster (1997). "Ultrasonic measurement of differential displacement and strain in a vascular model." Ultrason Imaging **19**(1): 19-38.

Scabia, M., M. Calzolai, et al. (2000). "A real-time two-dimensional pulsed-wave Doppler system." Ultrasound Med Biol **26**(1): 121-31.

Schiller, N. B. (1985). "Echocardiography: current status and future prospects." Int J Card Imaging **1**(1): 41-60.

Schrank, E., D. J. Phillips, et al. (1990). "A triangulation method for the quantitative measurement of arterial blood velocity magnitude and direction in humans." Ultrasound Med Biol **16**(5): 499-509.

Severino, S., P. Caso, et al. (2000). "Involvement of right ventricle in left ventricular hypertrophic cardiomyopathy: analysis by pulsed Doppler tissue imaging." Eur J Echocardiogr **1**(4): 281-8.

Severino, S., P. Caso, et al. (1998). "Use of pulsed Doppler tissue imaging to assess regional left ventricular diastolic dysfunction in hypertrophic cardiomyopathy." Am J Cardiol **82**(11): 1394-8.

Slager, C. J., T. E. Hooghoudt, et al. (1986). "Quantitative assessment of regional left ventricular motion using endocardial landmarks." J Am Coll Cardiol **7**(2): 317-26.

Steel, R. and P. J. Fish (2002). "Error propagation bounds in dual and triple beam vector Doppler ultrasound." IEEE Trans Ultrason Ferroelectr Freq Control **49**(9): 1222-30.

Steel, R., P. J. Fish, et al. (2003). "Velocity fluctuation reduction in vector Doppler ultrasound using a hybrid single/dual-beam algorithm." IEEE Trans Ultrason Ferroelectr Freq Control **50**(1): 89-93.

Steel, R., K. V. Ramnarine, et al. (2003). "Angle-Dependence and Reproducibility of Dual-Beam Vector Doppler Ultrasound in the Common Carotid Artery of Normal Volunteers." Ultrasound Med Biol **30**(2): 271-6.

Steel, R., K. V. Ramnarine, et al. (2004). "Angle-dependence and reproducibility of dual-beam vector Doppler ultrasound in the common carotid arteries of normal volunteers." Ultrasound Med Biol **30**(2): 271-6.

Stepanishen, P. R. (1971). "Transient Radiation from Pistons in an Infinite Planar Baffle." J Acoust Soc Am **49**: 1629-1638.

Stoylen, A., A. Heimdal, et al. (1999). "Strain Rate Imaging by Ultrasound in the Diagnosis of Regional Dysfunction of the Left Ventricle." Echocardiography **16**(4): 321-329.

Stoylen, A., A. Heimdal, et al. (2000). "Strain rate imaging by ultrasonography in the diagnosis of coronary artery disease." J Am Soc Echocardiogr **13**(12): 1053-64.

Stoylen, A., S. Slordahl, et al. (2001). "Strain rate imaging in normal and reduced diastolic function: comparison with pulsed Doppler tissue imaging of the mitral annulus." J Am Soc Echocardiogr **14**(4): 264-74.

Streeter, D. D., Jr., H. M. Spotnitz, et al. (1969). "Fiber orientation in the canine left ventricle during diastole and systole." Circ Res **24**(3): 339-47.

Strony, J., A. Beaudoin, et al. (1993). "Analysis of shear stress and hemodynamic factors in a model of coronary artery stenosis and thrombosis." Am J Physiol **265**(5 Pt 2): H1787-96.

Sutherland, G. R., M. J. Stewart, et al. (1994). "Color Doppler myocardial imaging: a new technique for the assessment of myocardial function." J Am Soc Echocardiogr **7**(5): 441-58.

Taratorin, A. M. and S. Sideman (1995). "3D functional mapping of left ventricular dynamics." Comput Med Imaging Graph **19**(1): 113-29.

Teirlinck, C. J., R. A. Bezemer, et al. (1998). "Development of an example flow test object and comparison of five of these test objects, constructed in various laboratories." Ultrasonics **36**(1-5): 653-60.

Tortoli, P., G. Guidi, et al. (1992). "Experimental Proof of Doppler Bandwitdh Invariance." IEEE Trans UFFC **39**(2): 196-203.

Tortoli, P., G. Guidi, et al. (1993). "Transverse Doppler spectral analysis for a correct interpretation of flow sonograms." Ultrasound Med Biol **19**(2): 115-21.

Trahey, G. E., J. W. Allison, et al. (1987). "Angle independent ultrasonic detection of blood flow." IEEE Trans Biomed Eng **34**(12): 965-7.

Trahey, G. E., S. M. Hubbard, et al. (1988). "Angle independent ultrasonic blood flow detection by frame-to-frame correlation of B-mode images." Ultrasonics **26**(5): 271-6.

Tupholme, G. E. (1969). "Generation of Acoutics Pulses by Baffled Plane Pistons." Mathematika **16**: 209-224.

Uematsu, M., K. Miyatake, et al. (1995). "Myocardial velocity gradient as a new indicator of regional left ventricular contraction: detection by a two-dimensional tissue Doppler imaging technique." J Am Coll Cardiol **26**(1): 217-23.

Uematsu, S. (1981). "Determination of volume of arterial blood flow by an ultrasonic device." J Clin Ultrasound **9**(5): 209-16.

Wei-qi, W. and Y. Lin-xin (1982). "A double beam Doppler ultrasound method for quantitative blood flow velocity measurement." Ultrasound Med Biol **8**(4): 421-5.

Weydahl, E. S. and J. E. Moore (2001). "Dynamic curvature strongly affects wall shear rates in a coronary artery bifurcation model." J Biomech **34**(9): 1189-96.

Wilson, K., M. Whyman, et al. (1999). "The relationship between abdominal aortic aneurysm wall compliance, maximum diameter and growth rate." Cardiovasc Surg **7**(2): 208-13.

Wilson, K. A., P. R. Hoskins, et al. (2000). "Ultrasonic measurement of abdominal aortic aneurysm wall compliance: a reproducibility study." J Vasc Surg **31**(3): 507-13.

Wilson, L. S. and R. W. Gill (1993). "Measurement of two-dimensional blood velocity vectors by the ultrasonic speckle projection technique." Ultrason Imaging **15**(4): 286-303.

Yeh, C. K. and P. C. Li (2002). "Doppler angle estimation of pulsatile flows using AR modeling." Ultrason Imaging **24**(2): 65-80.

Yeh, C. K. and P. C. Li (2002). "Doppler angle estimation using AR modeling." IEEE Trans Ultrason Ferroelectr Freq Control **49**(6): 683-92.

Young, A. A., C. M. Kramer, et al. (1994). "Three-dimensional left ventricular deformation in hypertrophic cardiomyopathy." Circulation **90**(2): 854-67.

Zhu, H. and M. H. Friedman (2003). "Relationship between the dynamic geometry and wall thickness of a human coronary artery." Arterioscler Thromb Vasc Biol **23**(12): 2260-5. Epub 2003 Sep 18.

Published Papers

2 papers have been published during the completion of the PhD:

Bonnefous, O., A. Criton, et al. (2000). "New TDI Developments for Vascular and Cardiac Applications." IEEE UFFC Proceedings: 1285-1290.

Criton, A., R. Steel, et al. (2002). "Real Time Vector Doppler for Tissue Motion." IEEE UFFC Proceedings: 1529-1534.

NEW TDI DEVELOPMENTS FOR VASCULAR AND CARDIAC APPLICATIONS

O. Bonnefous[1], A. Criton[2], L. Germond[1], and E. Denis[1]
[1]Laboratoires d'électronique Philips, 22 av. Descartes, BP 15, 94453 Limeil-Brévannes, France
[2]ATL, 22100 Bothell Everett Highway 9802-8431, PO Box 3003 98041-3003, Bothell, Washington, USA

Abstract - Tissue Doppler Imaging can show the biomechanical properties of living tissues in both vascular and cardiac applications. Technical validation of new quantitative methods implemented into a commercial ultrasound system is described. This includes simulations taking into account physiologic mechanical events, and data generation using motion phantoms. The results are promising since the measurement accuracy of parameters such as arterial dilation, cardiac wall thickening, myocardium strain rates is on the order 5-10 %. It is also shown that strain sequences can correctly represent physical phenomena.

I. INTRODUCTION

This paper describes how the Tissue Doppler Imaging (TDI) technique can be adapted to allow functional characterization of arterial and cardiac walls in 2D images. Such a characterization relies on the definition of clinically relevant physiological parameters, a specific optimization of the TDI settings and the validation of the parameter measurements.

The paper is organized as follows: in section II, the TDI principle is briefly reviewed; in section III, physiological parameters are introduced and the principle of their measurements is described; in section IV, the computer simulations used to optimize the TDI settings are presented and a phantom validation of the method is discussed; finally, in section V some clinical examples are provided.

II. PRINCIPLE OF TDI

TDI is a relatively new ultrasound modality [1], which estimates the component of the tissue velocity vector projected on the acoustic beam. The displacements of the structures of interest induce phase shifts on successive high frequency ultrasound echoes backscattered by the moving medium. These phase shifts are processed to estimate the local velocity of the objects under examination. The velocity values are color-coded for the visualization, and superimposed on the corresponding anatomical grayscale image.

The signal processing performed in TDI is similar to that used by Color Doppler systems to image blood flow. However, modifications of the echographic settings are necessary. As, the tissue velocity is low compared to the blood velocity and the tissue signal amplitudes are high compared to the blood signal amplitudes. These modifications include shorter ensemble length, lower Pulse Repetition Frequencies (PRFs) and deactivation of the wall filter.

III. PHYSIOLOGICAL PARAMETERS DESCRIPTION AND MEASUREMENTS

The motion of biological structures seen by TDI is due to the interaction between internal mechanical forces (arterial pressure, myocardium contraction/relaxation strength) with tissues (arterial wall, myocardium. Using TDI sequences, it is possible to extract specific physiological parameters, which can be imaged and used to the biomechanical functions of the cardiac and arterial walls.

In this paper four parameters are considered *(i)* motion, *(ii)* arterial dilation or myocardial thickening, *(iii)* intramural strain rate and *(iv)* strain and it is described in this section how they can be derived from the tissue velocities.

Motion estimation

Wall edges are first extracted automatically from the B-mode images of the sequence using an edge detector algorithm. The position of the structures is then mapped on the TDI data planes. Based on the location of the moving structures, the algorithm performs local time integration of the TDI velocity values. It computes the wall displacement curves as a function of time throughout the cardiac cycle, and as a function of position.

Let z be the coordinate of a point along the acoustic beam and inside the structure of interest. The displacement of this point M(z,t) is estimated by :

$$M(z,t) = \int_{t_0} V(z,u)du \qquad (1)$$

where V(z,t) is the velocity provided by the TDI, and t_0 is for instance the beginning time of the cardiac cycle.

Arterial dilation or myocardial thickening

This parameter describes the relative displacement of points located on opposite sides of a structure. This definition corresponds to both the dilation of an artery or the thickening of the myocardium.

Let z_1 and z_2 be the positions of two points located on opposite edges of the structure along the acoustic beam. The wall dilation or thickening $D(z_1,z_2,t)$ is calculated by subtracting the motion tracking information at the positions z_1 and z_2:

$$D(z_1,z_2,t) = M(z_1,t) - M(z_2,t) \quad (2)$$

Intramural strain and strain rate

Strain

Strain is the representation of the compressibility ability of a medium. Given two close positions z and (z+δz) along the acoustic beam and inside the structure of interest, the strain S(z,t) equals :

$$S(z,t) = \frac{M(z+\delta z,t) - M(z,t)}{\delta z} = \frac{\partial M(z,t)}{\partial z} \quad (3)$$

Strain rate

The strain rate SR(z,t) represents the velocity of compression or dilation of the tissue. It is defined by:

$$SR(z,t) = \frac{\partial S(z,t)}{\partial t} \qquad (4)$$

From (1) and (3), it follows that the strain rate can be directly derived from the TDI information:

$$SR(z,t) = \frac{\partial V(z,t)}{\partial z} \qquad (5)$$

Equations (4) and (5) can also be combined to derive the strain directly from the TDI information:

$$S(z,t) = \int_{t_0} \frac{\partial V(z,u)}{\partial z} du \qquad (6)$$

Equations (5) and (6) are used in section IV to estimate the strain and strain rate.

IV. Optimal TDI settings

The four parameters described previously are estimated through the TDI mode implemented on a commercial ultrasound system (ATL HDI 5000). The accuracy of their measurement is strongly dependent on the acquisition settings of the ultrasound system and the characteristics of the biologic motion/strain curves that we want to evaluate. The processing performance is studied through numerical simulations of the system and through experimental tests using controlled-motion phantoms.

The two main factors influencing the results are the scanning sequences and the precision of the TDI velocity estimate:

- The scanning sequence used for TDI induces time delays in the velocity estimation, which means that a 2D frame of a sequence does not represent an instantaneous map of the velocity field. This asynchronism influences the computation of motion curves (cf. equation 1) since a time reference t_0 is required to perform the velocity integration. The asynchronism produces motion artifacts that could be mistakenly interpreted as natural biomechanical effects. The numerical and experimental validations presented below allow the evaluation of the resynchronization step applied to the TDI sequences to suppress these artifacts. This correction is based on a Shannon time interpolation between the frames of the sequence.
- The accuracy of the TDI estimate will naturally influence the accuracy of all the derived quantities. This is mainly determined by the velocity range used for acquisition.

Computer simulation

The simulation principle consists of defining point scatterers randomly distributed in 2D, parallel layers, moving symmetrically relatively to a medial axis. The motion curve used is the dilation of a normal carotid acquired *in vivo*. This moving medium is virtually « scanned » using typical HDI 5000 acquisition sequences; each RF signal is generated taking into account the position of the scatterers as a function of time considered. The ultrasound beams, which define the contribution of the scatterers, are Gaussian shaped. At this stage, impulse responses of the medium are obtained, which are then convolved with an acoustic pulse transmitted by the probe. The

sequence of RF signals is constructed following this scheme. Then, the signals are processed to produce TDI sequences, comprising echo and TDI color data.

Phantom Data generation.

An experimental setup for the validation of the motion measurements and another for the validation of the strain and strain rate measurements have been built. Each setup includes a phantom, a PC driven controller (MM4005, Micro-Controller) and a DC-motor applied to a translation stage (UTMCC.5HA).
A phantom made of two layers of agar is used for the motion validation. One layer is glued to a moving piston, while the other layer is fixed and connected to the probe. Water is used as the propagating medium between the two layers (Figure 1).
For the strain and strain rate validations, the phantom is made of one block of agar. It is fixed to the probe. The piston is then used to compress the phantom (Figure 2). The HDI 5000 system is used to acquire the echo and TDI color data.

Results of validation

The data generated numerically or experimentally are compared to the reference curves used in the simulations or experiments. Figures 3 and 4 show the dilation curves estimated from computed data and from phantom acquired data respectively. Dilation/Strain curves are estimated for each scanning position of the image, allowing the comparison of the results along the transversal axis. Standard deviation and bias are computed for all the configurations implemented in the scanner. This includes velocity ranges (PRFs), and sensitivity characteristics (MAX, HIGH, MED, LOW) defined by the ensemble length.

Figures 5 and 6 present standard deviation and bias of dilation estimation, for numeric and experimental TDI data respectively. It is shown on simulated data (Figure 5) the effectiveness of the resynchronization step applied to the color data. This is less visible for the experimental results. These are polluted by a high frequency vibration due to an oscillation of the water generated by the fast displacement of the piston (Figure 6). The standard deviation and bias values (5-10 %) demonstrate that a quantitative characterization of dilation can be made. The exception is for the lowest velocity range where the frame rate is too low to allow a correct reconstruction of the motion curves. The decrease of the bias with the increased velocity range, exhibited by the experimental results is due to a better time sampling of the artefactual high frequency vibration. This is due to the increase of frame rate with the velocity range.

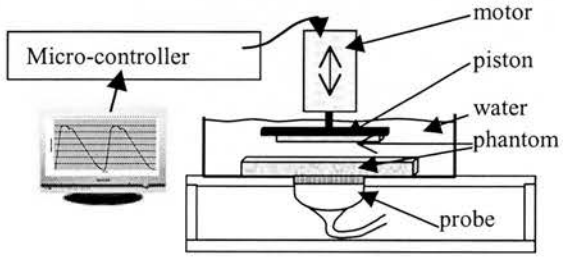

Figure 1: Setup for phantom validation of dilation

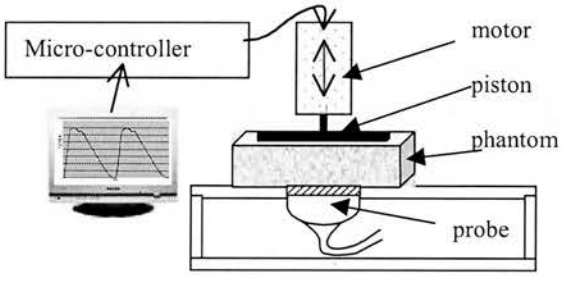

Figure 2: Setup for phantom validation of strain

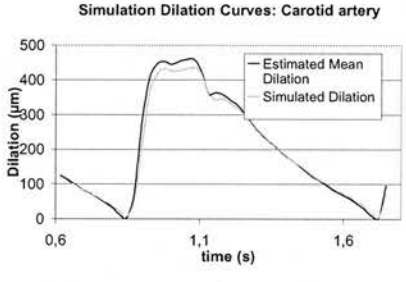

Figure 3: Simulated and Estimated Dilation curves. Numerical Data

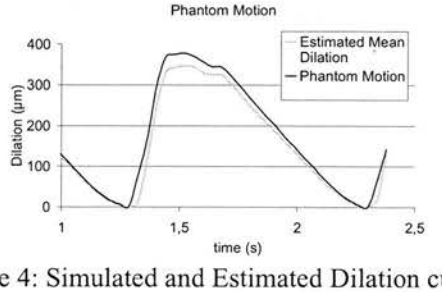

Figure 4: Simulated and Estimated Dilation curves. Experimental Data

Dilation

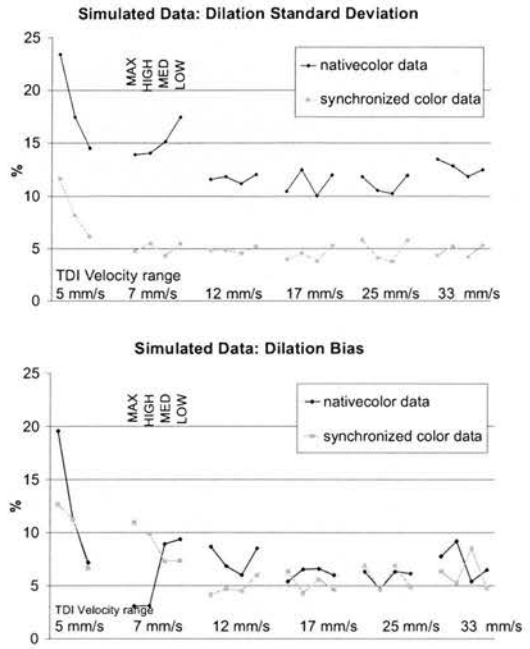

Figure 5: Standard Deviation and Bias of Dilation estimation. Simulated Data

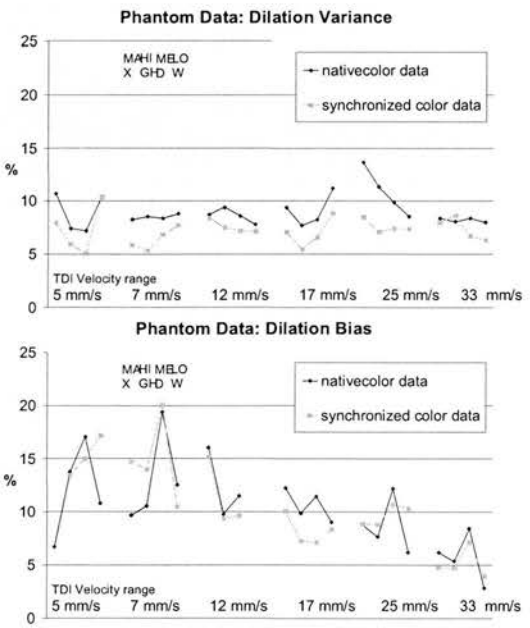

Figure 6: Standard Deviation and Bias of Dilation estimation. Experimental Data

Strain and Strain rate

Figure 7 plots the strain rate estimation, using experimental data where constant strain rates are generated by the piston displacement. There is a good correlation at low values of strain rate, while the standard deviation increases as a function of strain rate due to the decrease of available sampling points.

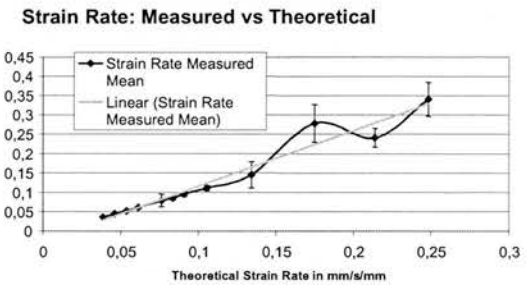

Figure 7: Strain rate estimation

In Figure 8, dynamic strain rates are used (Phantom with motion curve of Figure 4) for the same evaluation. This good performance (accuracy ~5%) also leads to satisfactory quantification of dynamic strain rate. Figure 9 presents the evaluation of the standard deviation and bias of strain estimation for experimental TDI data.

The relatively good performance of strain rate measurements lead to satisfactory estimation of strain: the maximum strain being around 22 µm/mm, standard deviation and bias around 20% represent errors of 2.2 µm/mm. It is proposed that these measurements and their color representation will allow acceptable qualitative strain characterization.

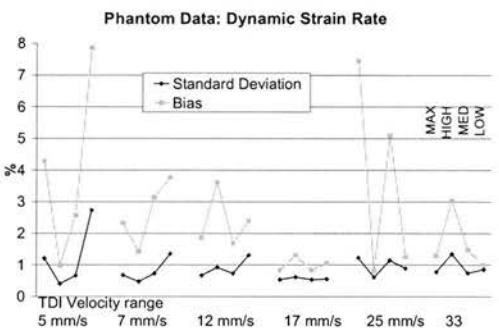

Figure 8: Standard Deviation and Bias of Dynamic Strain Rate estimation. Experimental Data.

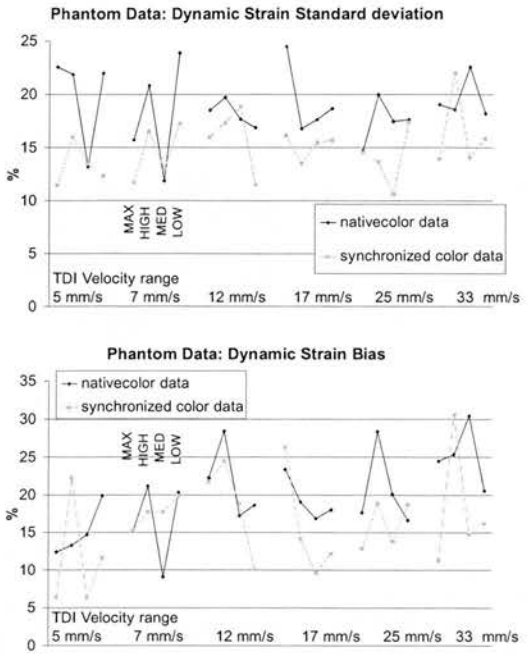

Figure 9: Standard Deviation and Bias of Dynamic Strain estimation. Experimental Data.

V. CLINICAL EXAMPLES

Carotid artery

The main risk associated with a lesion of the carotid artery is a cerebro-vascular incident due to the rupture of plaque present at the lesion location. Currently, the diagnosis is based on the percentage of lumen reduction of the stenosis and on the visual assessment of plaque morphology. However, the specificity of the diagnosis is very poor since 95% of the endarterectomies performed for stenoses of more than 60% prove to be unnecessary. Until now no pre-operative, non-invasive technique can discriminate plaque types or stratify stroke risk with sufficient reliability to support clinical decision-making.

Our work aims at providing non-invasive criteria to assess more precisely the risk of rupture. It is based on the hypothesis that the mechanical features of the plaque influence its probability of rupture. The complex composition of a plaque (including fibrous material, focal calcifications, soft necrotic lipid pools) is the cause of heterogeneous stress-strain rates that ultimately lead to rupture [2].

These hypotheses have been visually assessed on a data set of 50 normal arteries and 40 carotid arteries with stenoses over 70%. For normal arteries, all the points exhibit synchronized and homogeneous motion whereas, in the presence of atheromatous plaque, there exist localized spatio-temporal motion discontinuities.

The pathological example presented in Figure 10 corresponds to a 90% stenosis with a calcified plaque. It represents the wall motion at the systolic peak. The characteristics are an overdilation proximal to the stenosis and a large wall displacement gradient at the edge of the plaque.

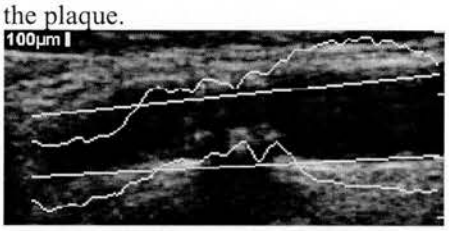

Figure 10: Wall motion discontinuities for a stenosis of 90%

Figure 11 displays the strain inside the wall and plaque tissue demonstrating that intramural distension coincides with large lateral strains (light gray) of the arterial wall. Another observation is that calcified structures are not compressed when surrounding tissues are strongly stressed.

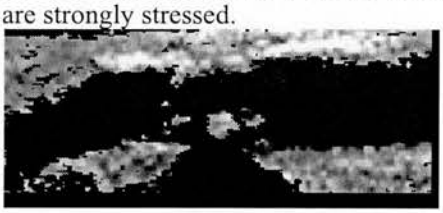

Figure 11: Strain for stenosis

Cardiac muscle

Regional cardiac wall impairment function precedes changes in more global indices of function due to compensatory hyperactivity of healthy tissue surrounding the impaired wall segment [3].

One of the goals of a clinical validation is to verify that the functional parameters can assess the normal function (contraction and dilation) of the myocardium throughout the cardiac cycle.

Figure 12 illustrates the motion tracking of the epicardial and endocardial borders of the ventricle posterior wall on an M-mode image of the parasternal

apical view of the heart. From the wall tracking traces wall thickening can be deducted (c.f. Figure 13).

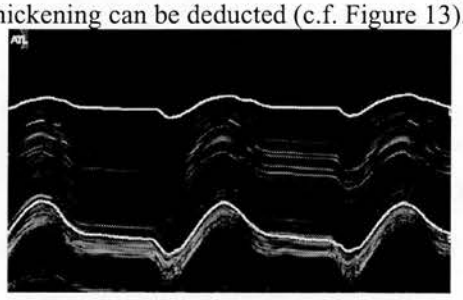

Figure 12: Motion tracking of the ventricular wall (Mitral valve ring and apex in white traces) on an M-mode of a parasternal apical view of the heart.

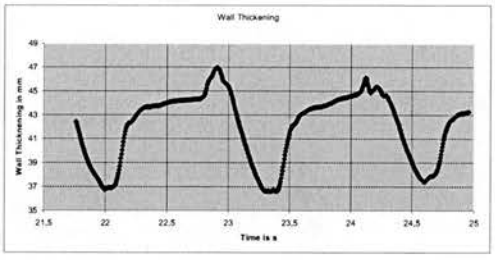

Figure 13: Wall thickening of the ventricular in a parasternal apical view of the heart

Figure 14 presents an example of a TDI M-mode and the strain rate M-mode derived from the TDI information. On the TDI display, light grays represent tissue moving away from the transducer and dark grays represent motion towards the transducer. On the strain rate display, the light grays represent dilation of the cardiac muscle and the dark grays, compression. TDI and strain rate information presents a cyclic variation that can be divided into three main phases in the cardiac cycle: atrial filling (AF), systole (S), and early filling (EF). During the AF phase, the atria contract to eject blood in the ventricles through the mitral valves (the atrial septum is encoded in dark gray).

During systole the ventricles are contracting (dark gray shades) to eject blood in the aorta and in the pulmonary arteries. The systolic phase is followed by early filling where the ventricles are rapidly relaxing (expansion in light gray) creating a differential pressure between the ventricles and the atria. This differential pressure pushes the mitral valves open and then allows the blood to flow from the atria within the ventricles.

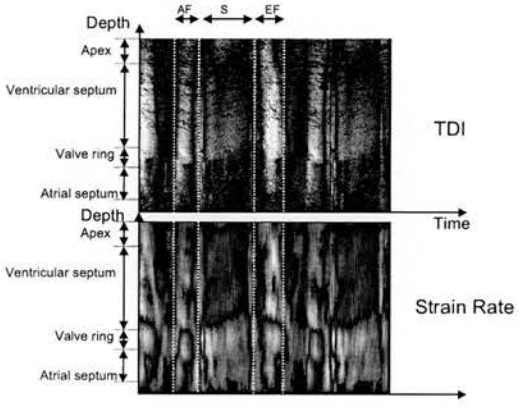

Figure 14: TDI and strain rate of the ventricular in a parasternal apical view of the heart.

VI. Conclusion

This technical validation step was essential for the evaluation of potential clinical parameters. Using simulated and experimental data allowed an understanding of the impact of artifacts and the effectiveness of the proposed corrections.

From the results presented in this paper, it can be seen that motion and strain rate imaging can be considered as quantitative, whereas strain can be used as visualization tool.

The next step consists in large scale clinical validations of these measurements.

VII. References

[1] McDicken W., Sutherland G., Moran C., and Gordon L., "Color Doppler Velocity of the Myocardium," Ultrasound Med. Biol. 1992; 18, 651-654.

[2] Vito RP, Whang MC, Giddens DP, et al. Stress analysis of the diseased arterial cross-section, ASME. Adv Bioeg Proc 1990;273-276.

[3] Isaaz K., Thompson A., Ethevenot G., Cloez J.L., Brembilla B., Pernod C. (1989) Doppler echocardiographic measurement of low velocity motion of the left ventricular posterior wall. Am. J. Cardiol 64:66-75.

REAL TIME VECTOR DOPPLER FOR TISSUE MOTION

A. Criton[1], R. Steel[2], P. R. Hoskins[2], W. N. McDicken[2], and H. F. Routh[3]
[1]Philips Ultrasound, Bothell, Washington, USA
[2]Department of Medical and Radiological Sciences, University of Edinburgh, Edinburgh, UK
[3]Philips Research, Briarcliff Manor, New York, USA

Abstract - Tissue Doppler Imaging (TDI) can reveal biomechanical properties of moving tissues for vascular and cardiac imaging. However, a major drawback of these measurements is that the motion estimation is limited to the component along the ultrasound beam axis. Cardiac and vessel wall motion studies have shown that complex three-dimensional motions can be observed, and that there is a clinical need to fully assess the three components of the vector motion. This work describes how TDI can be extended by acquiring a real time two-component velocity vector via a dual beam vector Doppler technique. A vector Doppler velocity estimator using a small interbeam angle can suffer from both bias and large variance. This estimator is also strongly dependent on the settings of the echographic system. To reduce the large bias and variance, most vector velocity techniques use a very large ensemble length (EL) (>20), which does not allow real time implementation. We propose a new processing technique, which reduces the bias and the standard deviation of the vector velocity estimate. The new method assumes that the vector velocity angle varies slowly over the cardiac cycle. The angle can then be estimated using a large time window. The performance of this new technique has been tested experimentally using a tissue mimicking rotating phantom. It is shown that the factors influencing the results are the EL, the precision of the TDI estimates and the time window. The results indicate that the variance and bias of velocity magnitude and orientation estimates decrease with increasing EL, increasing precision of the TDI estimates and increasing time window. Using an EL of 9, 8 bits for the velocity estimate, and an observation time of one second, a 5-degree bias of the angle estimate is observed, with a variance below 7 degree averaged over all angles. A 10% bias of the velocity magnitude is observed, with a variance of 1%. In conclusion, TDI can be improved with vector Doppler providing two-dimensional tissue motion estimation, enabling more accurate biomechanical tissue property assessment.

Introduction

This paper describes how Tissue Doppler Imaging (TDI) can be adapted to acquire a real time two-component velocity vector via a dual beam vector Doppler technique.

The paper is organized as follows: in section I, the TDI principle is briefly reviewed; in section II, the dual beam vector Doppler technique and the novel processing technique to reduce error and variance of the velocity estimate are described; in section III, a phantom validation to optimize the TDI settings is presented.

I. PRINCIPLE OF TDI

TDI is a relatively new ultrasound modality [1], which estimates the component of the tissue velocity vector projected on the acoustic beam. The displacements of the structures of interest induce phase shifts on successive high frequency ultrasound echoes backscattered by the moving medium. These phase shifts are processed to estimate the local velocity of the objects under examination. The velocity values are color-coded for the visualization, and superimposed on the corresponding anatomical grayscale image.

The signal processing performed in TDI is similar to that used by Color Doppler systems to image blood flow. However, modifications of the echographic settings are necessary. As, the tissue velocity is low compared to the blood velocity and the tissue signal amplitudes are high compared to the blood signal amplitudes. These modifications include shorter ensemble length, lower Pulse Repetition Frequencies (PRFs) and deactivation of the wall filter.

II. Description of the Vector Doppler System and Novel Estimator

The ultrasound system for measuring true velocity has a linear phased transmit receive transducer array which has a crossbeam configuration capable of resolving two orthogonal components of the velocity vector (within the plane of the transducer). This approach utilizes a single transducer array, transmitting ultrasound from a transmit aperture and receiving backscattered echoes from two sub-arrays defined by two sets of elements, on either side of the transmit array. The system is capable of resolving the radial velocity component in the acoustic beamsteering direction and the transverse component at right angle to the beamsteering direction. Figure 1 illustrates such a device.

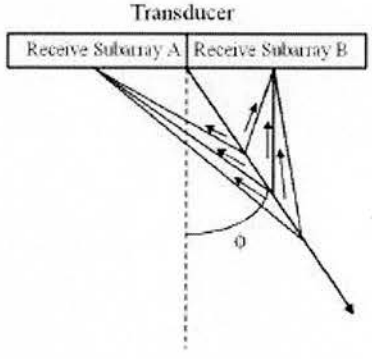

Figure 1: Aperture Receive Configuration

The transmit aperture transmit an acoustic beam steered in the direction □. The angle □ is measured from a normal to the array. In reception the echoes backscattered from moving targets are received by the left and right receiver sub arrays simultaneously.

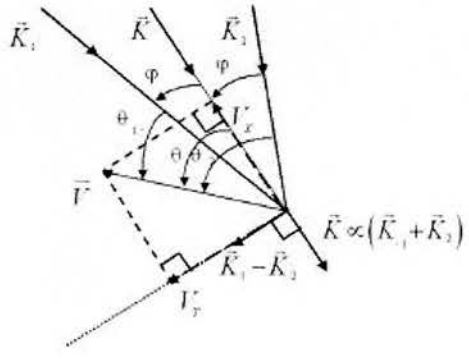

Figure 2: Aperture Receive Configuration

In figure 2, $\vec{K}$ is a unit vector in the direction of the transmitted ultrasound wave vector, and $\overrightarrow{K_1}$ and $\overrightarrow{K_2}$ are unit center ultrasound wave vectors for the two receiving directions. The position of the center in left and right sub-apertures must be such that the center wave vectors $\overrightarrow{K_1}$ and $\overrightarrow{K_2}$ subtend the same angle □ with respect to the transmit wave vector $\vec{K}$. In this configuration the vector sum $\overrightarrow{K_1}+\overrightarrow{K_2}$ is parallel to the transmit beamsteering direction and therefore to $\vec{K}$ and the vector difference $\overrightarrow{K_1}-\overrightarrow{K_2}$ is perpendicular to the beamsteering direction and therefore to $\vec{K}$. The targets move with a certain velocity $\vec{V}$, which is at an angle □ to the direction of the incident ultrasound beam.

If scatterers move with a velocity $\vec{V}$ past a sample volume in the insonified field of view, the mean Doppler frequency shifts $\overline{f_1}$ and $\overline{f_1}$ are given using the following equations (1):

$$\overline{f_1}=\frac{|\vec{V}|[\cos(\theta_1)+\cos(\theta)]f_0}{c}$$
$$\overline{f_2}=\frac{|\vec{V}|[\cos(\theta_2)+\cos(\theta)]f_0}{c} \quad (1)$$

where c is the celerity of the ultrasound wave in the medium insonified, f_0 is the transmit center frequency, θ_1 is the angle between the left receive beam and the velocity vector $\vec{V}$ and θ_2 is the angle between the right receive beam and the velocity vector.

By solving the geometrical equations it can be found that the orientation of the vector velocity is:

$$\theta=\tan^{-1}\left[\frac{(\overline{f_1}-\overline{f_2})}{(\overline{f_1}+\overline{f_2})}\times\frac{(\cos(\varphi)+1)}{\sin(\varphi)}\right] \quad (2)$$

It can also be shown that equation (1) can be expressed as function of scalar product of unit ultrasound wave vectors:

$$\overline{f_1}\times\frac{c}{f_0}=(\overrightarrow{K_1}+\vec{K})\bullet\vec{V}$$
$$\overline{f_2}\times\frac{c}{f_0}=(\overrightarrow{K_2}+\vec{K})\bullet\vec{V} \quad (3)$$

By adding and subtracting the previous equations we obtain:

$$\left(\overline{f_1}+\overline{f_2}\right)\times\frac{c}{f_0}=\left(\overrightarrow{K_1}+\overrightarrow{K_2}\right)\bullet\vec{V}+2\vec{K}\bullet\vec{V}$$
$$\left(\overline{f_1}-\overline{f_2}\right)\times\frac{c}{f_0}=\left(\overrightarrow{K_1}-\overrightarrow{K_2}\right)\bullet\vec{V} \quad (4)$$

The difference of the receive unit vectors $\left(\overrightarrow{K_1}-\overrightarrow{K_2}\right)$ is perpendicular to the transmit beamsteering direction and therefore to $\vec{K}$, while the sum $\left(\overrightarrow{K_1}+\overrightarrow{K_2}\right)$ is proportional to $\vec{K}$ and therefore the sum $\left(\overrightarrow{K_1}+\overrightarrow{K_2}+2\vec{K}\right)$ is parallel to $\vec{K}$. Thus the beam component V_B and the transverse component V_T of the vector velocity $\vec{V}$ can be calculated with the following equations:

$$V_B=|\vec{V}|\cos(\theta)=\frac{\left(\overrightarrow{K_1}+\overrightarrow{K_2}\right)\bullet\vec{V}+2\vec{K}\bullet\vec{V}}{2\cos(\varphi)+2} \quad (5)$$
$$=\left(\overline{f_1}+\overline{f_2}\right)\times\frac{c}{f_0\times\left(2\cos(\varphi)+2\right)}$$

$$V_T=|\vec{V}|\sin(\theta)=\frac{\left(\overrightarrow{K_1}-\overrightarrow{K_2}\right)\bullet\vec{V}}{2\sin(\varphi)} \quad (6)$$
$$=\left(\overline{f_A}-\overline{f_B}\right)\times\frac{c}{2\sin(\varphi)\times f_0}$$

For the regular Doppler technique, the complex received signal (after the Hilbert transform) sampled at the depth of interest for a narrow band pulse can be expressed as following:

$$s=A\exp\left(2\pi jT_{PRF}\overline{f}\right)=I+jQ \quad (7)$$

where c is the sound velocity, $\overline{f}$ is the Doppler mean frequency shift, T_{PRF} the time between two pulse emissions, A is the amplitude of the signal

In the case of the crossbeam configuration, the two sub-apertures receive signals can be written as:

$$s_1=A\exp\left(2\pi jT_{PRF}\overline{f}_1\right)=I_1+jQ_1$$
$$s_2=A\exp\left(2\pi jT_{PRF}\overline{f}_2\right)=I_2+jQ_2 \quad (8)$$

By combining the two previous equations we obtain:

$$s_1\times s_2=A^2\exp\left(2\pi jT_{PRF}\left(\overline{f}_1+\overline{f}_2\right)\right)$$
$$s_1\times s_2^*=A^2\exp\left(2\pi jT_{PRF}\left(\overline{f}_1-\overline{f}_2\right)\right) \quad (9)$$

The two phases of the signals described in equations (I.9) are given by:

$$phaseShift_B=2\pi T_{PRF}\left(f_1+f_2\right)$$
$$phaseShift_T=2\pi T_{PRF}\left(f_1-f_2\right) \quad (10)$$

where,

$$phaseShift_T=\arctan\left(\frac{\mathrm{Im}\left(R_1(1)\right)\mathrm{Re}\left(R_2(1)\right)+\mathrm{Im}\left(R_2(1)\right)\mathrm{Re}\left(R_1(1)\right)}{\mathrm{Re}\left(R_1(1)\right)\mathrm{Re}\left(R_2(1)\right)-\mathrm{Im}\left(R_1(1)\right)\mathrm{Im}\left(R_2(1)\right)}\right)$$

$$phaseShift_B=\arctan\left(\frac{\mathrm{Im}\left(R_1(1)\right)\mathrm{Re}\left(R_2(1)\right)-\mathrm{Im}\left(R_2(1)\right)\mathrm{Re}\left(R_1(1)\right)}{\mathrm{Re}\left(R_1(1)\right)\mathrm{Re}\left(R_2(1)\right)+\mathrm{Im}\left(R_1(1)\right)\mathrm{Im}\left(R_2(1)\right)}\right) \quad (11)$$

where $R_i(k)$ represents the autocorrelation function of lag k (integer) of s_i and is expressed as:

$$R_i(k)=\sum_{n=0}^{n=N-k}s_i(n)\times s_i(n+k)^* \quad (12)$$

where N is the total number of pulses sent to form a line and i={1,2}.

Therefore we deduct V_T and V_B:

$$V_B=\frac{phaseShift_B}{2\pi T_{prf}}\times\frac{c}{f_0\times\left(2\cos(\varphi)+2\right)}$$
$$V_T=\frac{phaseShift_T}{2\pi T_{prf}}\times\frac{c}{f_0\times\left(2\sin(\varphi)\right)} \quad (13)$$

This combination of the in phase and quadrature signals from the two receive apertures is called heterodyning [2] and is used to increase the dynamic of the difference and sum of the Doppler frequency means. A conventional (no heterodyning) vector Doppler estimation has also been implemented. In this paper conventional vector Doppler (VD) estimator refers to non heterodyning and heterodyning (H) vector Doppler estimation will refer to the combination of the in phase and quadrature signals to extract the sum and difference of the mean Doppler frequencies. From observation made in vitro and in vivo for tissue motion it can be seen that the

angle variation of the vector velocity is slower than the variation of the magnitude velocity. The novel estimator uses this assumption to apply a low pass FIR filter to reduce temporal fluctuations of the angle estimation before calculating the velocity magnitude. The arctan function also increases in a non-linearly manner the variability of the angle estimation. The FIR filtering is applied before the arctan function on the ratio following (14), used in the final calculation of the angle (2):

$$\frac{\left(\overline{f}_1 - \overline{f}_2\right)}{\left(\overline{f}_1 + \overline{f}_2\right)} \qquad (14)$$

The magnitude velocity is then calculated using the filtered angle using the following equation (15):

$$|\vec{V}| = V_B / c\cos(\theta) \qquad (15)$$

where θ has been filtered.

III. Validation

TDI mode is currently implemented on a commercial ultrasound system (Philips Ultrasound HDI 5000). This system has been modified to acquire data in reception from two separate apertures and to do the heterodyning or conventional vector Doppler processing. The accuracy and precision of the vector Doppler measurement are strongly dependent on the acquisition settings of the ultrasound system. The processing performance is studied through experimental tests using controlled-motion rotating phantoms.

The two main factors influencing the results are the processing of the data and the precision and accuracy of the TDI velocity estimate:

- Heterodyning and conventional vector Doppler estimations have been assessed separately with and without the filtering of the angle estimation.
- The accuracy and precision of the TDI mean frequency estimate will naturally influence the accuracy and precision of vector Doppler estimators. The accuracy is mainly determined by the velocity range used for acquisition. The precision is assessed by the number of pulses used to calculate the vector Doppler estimation (ensemble length).

Phantom Setup

An experimental setup for the validation of the two-dimensional motion measurements has been built. This setup includes a phantom, a PC driven controller and a DC-motor applied to a rotating stage. The phantom consists of a circular layer of tissue mimicking material rotating in a tank with water and and glycerol (speed of sound = 1540 m/s). The circular layer is rotated around its axis by a synchronous motor via a gearbox. The motor also rotates a disk with uniformly spaced holes near its ream. Using an optical sensor, the rotational speed accuracy and variation are assessed by looking at the frequency and frequency standard deviation coming out of the optical sensor. The tank, where the tissue-mimicking wheel is immerged, is lined with acoustically absorbent textured rubber mating. A transducer is held above the rotating disc so that the scan-plane intersects the disc parallel to the flat sides of the disc. The HDI 5000 system is used to acquire the echo and TDI two-dimensional color data. Figure 3 illustrates the data collected from the rotating phantom.

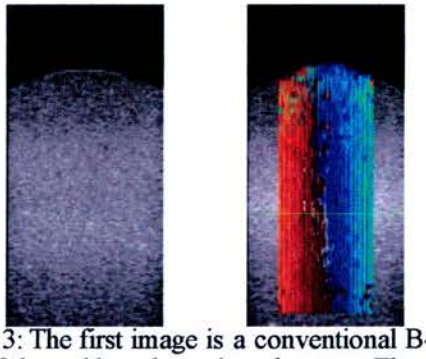

Figure 3: The first image is a conventional B-scan image of the gel-based rotating phantom. The second image illustrates TDI color-coded overlaid on B-mode.

Results of validation

The data collected experimentally are compared with theoretical velocity field generated by knowing the center of rotation and the speed of the rotation used in the experiments. Standard deviation and bias are computed for all the configurations implemented in the scanner and different filter length. This includes velocity ranges (PRFs), sensitivity characteristics defined by the ensemble length (varying from 2 to 9) and filter length (varying from 2 to 20). The results presented in the following figures

represent the mean bias and mean standard deviation error across all angles and velocity magnitudes.

Figure 4 and 5 present standard deviation and bias of the angle and the magnitude of the vector velocity as a function of ensemble length for both vector Doppler and the heterodyning estimators.

The angle bias and standard deviation are decreasing as a function of increasing ensemble length. The bias and standard deviation are smaller for the vector Doppler estimation than for the heterodyning technique.

The bias of the magnitude is also decreasing as a function of ensemble length for the vector Doppler and is below 5%. For the heterodyning the bias can be above 10%.

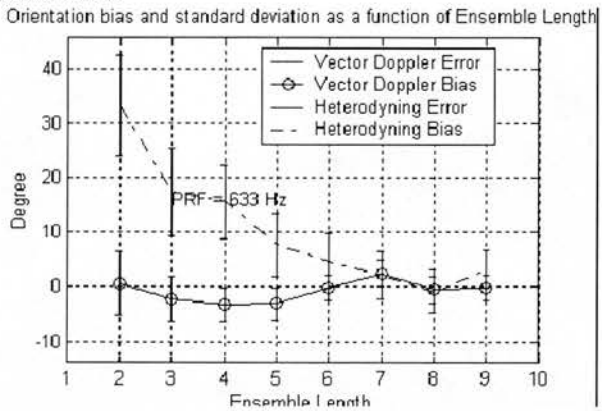

Figure 4: Standard Deviation and Bias in degree of the Angle for the VD and H estimators as a function of ensemble length (filter length = 20).

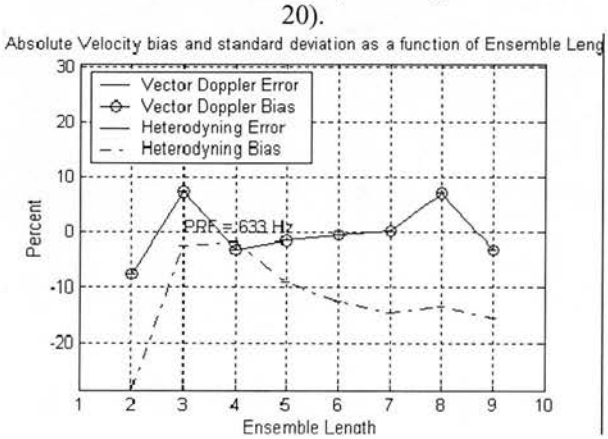

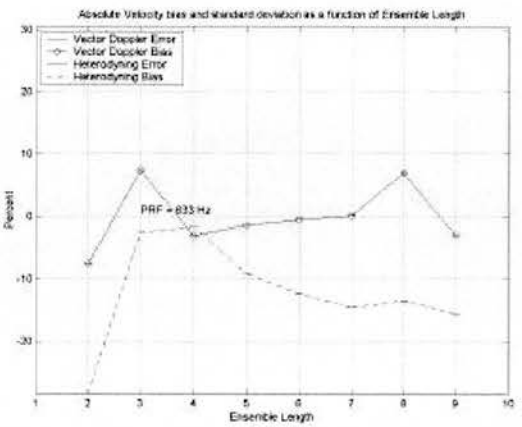

Figure 5: Standard Deviation and Bias in percent of the Magnitude for the VD and H estimators as a function of ensemble length (filter length = 20).

Figure 6 and 7 present standard deviation and bias of the angle and the magnitude of the vector velocity as a function of filter length for both vector Doppler and the heterodyning estimators.

The angle standard deviation is decreasing as a function of increasing ensemble length for both Vector Doppler and heterodyning. However the bias and error are higher for the heterodyning than for the vector Doppler. With no filtering of the angle estimation the angle standard deviation is above 20 degrees, with a filter length of 20 it reduces below 7 degrees and the bias around 5 degrees, which is suitable for quantitative analysis.

The bias of the magnitude is also decreasing as a function of ensemble length and is below 5% for the vector Doppler.

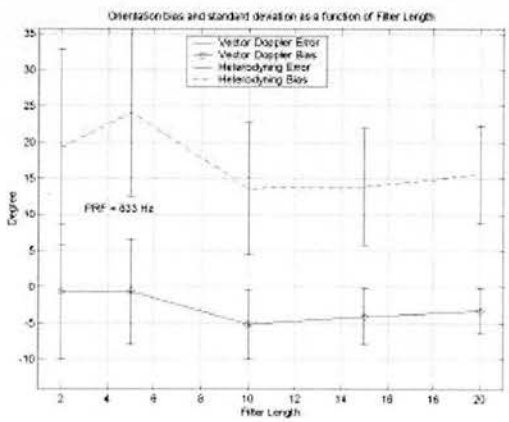

Figure 6: Standard Deviation and Bias in degree of the Angle for the VD and H estimators as a function of filter length (ensemble length = 4).

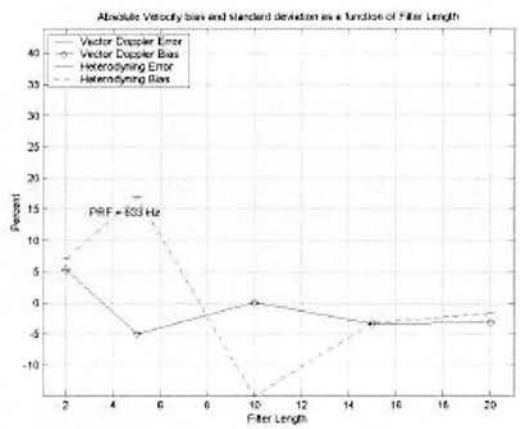

Figure 7: Standard Deviation and Bias in percent of the Magnitude for the VD and H estimators as a function of filter length (Ensemble Length = 4).

Figure 8 and 9 present standard deviation and bias of the angle and the magnitude of the vector velocity as a function of PRF for both vector Doppler and the heterodyning estimators.

The angle bias is stable as a function of PRF for both Vector Doppler (5 degree bias) and heterodyning (10 degree bias). However the bias and error are higher for the heterodyning than for the vector Doppler.

The bias of the velocity magnitude is also increasing as a function of PRF and is below 5% for low velocity scale.

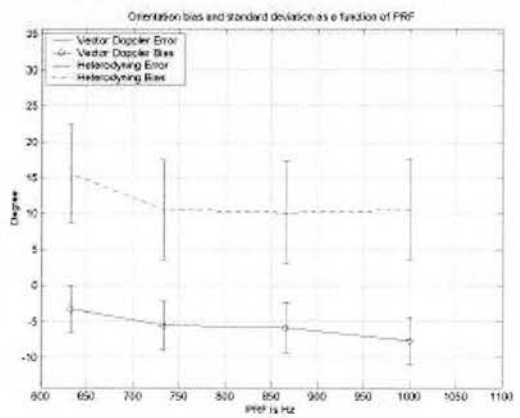

Figure 8: Standard Deviation and Bias in degree of the Angle for the VD and H estimators as a function of ensemble length (filter length = 20, ensemble length = 4).

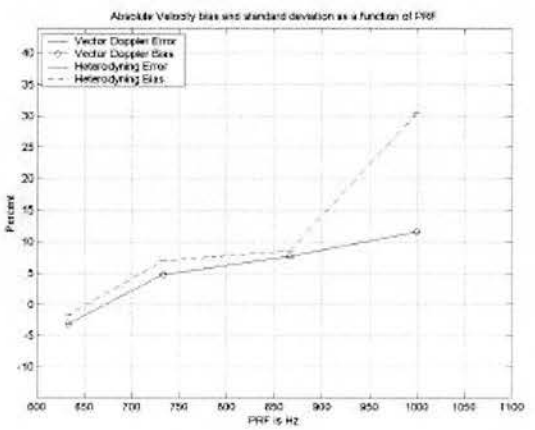

Figure 9: Standard Deviation and Bias in percent of the Magnitude of the VD and H estimators as a function of ensemble length (filter length = 20, ensemble length = 4).

These results allow defining the best acquisition and processing settings to estimate the tissue vector velocity magnitude and orientation. One of the first conclusions is that vector Doppler estimation has a lower bias and standard deviation than the heterodyning; therefore this estimator should be used to assess two-dimensional tissue vector velocities. The PRF should be set just above the aliasing point to reduce the bias and standard deviation on the velocity magnitude. The ensemble length should be set to 4 to decrease the standard deviation and bias of the angle estimation and the filter length should be to 20 to reduce the angle error. With these settings a bias less than 5 degree and a standard deviation around 7 degrees can be achieved for the angle estimation. The velocity magnitude estimator performance shows a bias less than 10% with a standard deviation less than 1%.

The standard deviation and bias values (5-10 %) demonstrate that a quantitative characterization of angle and velocity estimation can be performed.

IV. Conclusion

This technical validation step was essential for the evaluation of potential clinical parameters. Using experimental data allowed an understanding of the impact of acquisition settings and processing techniques.

From the results presented in this paper, it can be seen that two dimensional tissue motions can be assessed, as quantitative tool.

The next step consists in large-scale clinical validations of these measurements.

V. REFERENCES

[1] McDicken W., Sutherland G., Moran C., and Gordon L., "Color Doppler Velocity of the Myocardium," Ultrasound Med. Biol. 1992; 18, 651-654.

[2] Overbeck J. R., Beach K. W., Strandness D. E., "Vector Doppler: accurate measurements of blood velocity in two dimensions", Ultrasound Med Biol, 1992; 18; 19-3.